Volume II
Appendix D.7
Working Scenario

The Working Scenario was the result of a joint effort between the Columbia Accident Investigation Board (CAIB) and the NASA Accident Investigation Team (NAIT). The report was written beginning early in the investigation to track the current understanding of the events that led to the loss of *Columbia*. As such, the report evolved over time as facts became known, theories were developed or disproved, and NASA and the Board gained knowledge of the accident sequence.

The report was written to document the collection of known facts, events, timelines, and historical information of particular interest to the final flight of *Columbia*. The Columbia Accident Investigation Board released the final version of the Working Scenario to the public on July 8, 2003. The version contained here has been reformatted to match the overall style of the first volume and has had a few minor editorial corrections, but nothing that changes the substance of the report.

The Working Scenario includes information from numerous analyses, tests, and simulations related to the *Columbia* investigation that had been completed, or were ongoing at the time that this report was completed, i.e., up to and including July 8, 2003.

This effort compiles and documents the principal facts related to specific vehicle element events, timelines, and data. It also includes pertinent historical data surrounding some of the key vehicle element considerations in the investigation. The scenario addresses the chronology of vehicle events from prelaunch, launch countdown, launch/ascent, orbit, and re-entry, as well as specific information for the External Tank and the left wing, including aspects of the Reinforced Carbon-Carbon (RCC) and attachment hardware. Vehicle processing and significant preflight events and milestones are also discussed. The scenario addresses technical aspects only, and does not address management practices or philosophies, or other organizational considerations.

TABLES

FIGURES

Working Scenario

Prepared by the Columbia Accident Investigation Board (CAIB)
and the National Aeronautics and Space Administration (NASA) Accident Investigation Team (NAIT)

PREFACE

This Working Scenario report was written to document the collection of known facts, events, timelines, and historical information of particular interest to the final flight of *Columbia*. The report was written with the understanding that it could be published, either in part or in its entirety, as part of the official Columbia Accident Investigation Board (CAIB) report. The report includes information and results from numerous analyses, tests, and simulations related to the *Columbia* investigation that have been completed, or were ongoing at the time that this report was completed. It is anticipated that additional analytical and test results will emerge from ongoing work, as well as from future activities associated with the *Columbia* investigation and efforts related to the Return-To-Flight work. This Working Scenario includes information and results as they existed up to and including July 8, 2003.

1.0 INTRODUCTION

1.1 SCOPE

The Working Scenario is the result of a joint effort between the Columbia Accident Investigation Board (CAIB) and the NASA Accident Investigation Team (NAIT). This effort collates and documents the principal facts related to specific vehicle element events, timelines, and data. It also includes pertinent historical data surrounding some of the key vehicle element considerations in the investigation. The scenario addresses the chronology of vehicle events from prelaunch, Launch Countdown (LCD), launch/ascent, orbit, and entry as well as specific information for the External Tank (ET) and the Left Hand (LH) wing, including aspects of the Reinforced Carbon-Carbon (RCC) and attachment hardware. Vehicle processing and significant preflight events and milestones are also discussed. The scenario addresses technical aspects only, and does not address management practices or philosophies, or other organizational considerations.

The chronological portion of the scenario is contained in Sections 2 through 5 of this report. These sections discuss the prelaunch, launch, orbit, and deorbit/entry portions of the Space Transportation System 107 mission (STS-107). Sections 6 through 8 address the facts related to the Reusable Solid Rocket Motor (RSRM), Solid Rocket Booster (SRB), and Space Shuttle Main Engine (SSME) elements. Section 9 addresses relevant environmental factors such as weather and age of the ET. Section 10 addresses the details of *Columbia* vehicle processing, specifically as it pertains to the LH wing, from the most recent Orbiter Major Maintenance (OMM) at Palmdale, California, through the processing for STS-107. This section also includes a number of design and historical considerations for the LH wing and for the RCC in general. Section 11 addresses several aspects of the ET, including manufacturing, Kennedy Space Center (KSC) processing, Thermal Protection System (TPS) requirements, and numerous aspects of the foam insulation. These discussions provide the history of the bipod foam ramp design, fabrication, testing, and address the details of bipod foam ramp debris failure modes, testing, and analyses. Section 12 briefly summarizes the discussion of the working scenario.

The data sources and types include, but are not limited to, telemetry from all flight phases, Modular Auxiliary Data System (MADS) data from ascent and entry, video and imagery from launch/ascent and entry, and launch/ascent radar. It also includes reconstructed aerodynamic and vehicle loads, Radar Cross Section (RCS) and ballistics, aero/thermal, structural, debris forensics, post-flight test data (TPS impact, ET/SRB bolt catcher, wind tunnel, etc.), and prelaunch processing.

1.2 MISSION BACKGROUND

STS-107 was the 113th mission in the Space Shuttle program and *Columbia*'s 28th trip into space. These 28 missions spanned 22 years with the first being STS-1, launched on April 12, 1981. The STS-107 mission was a science research mission and the payload complement consisted of the

Spacehab Double Research Module and the Fast Reaction Enabling Science, Technology, and Research (FREESTAR). The mission altitude was approximately 150 nautical miles with an inclination of 39 degrees. Figure 1-1 depicts the STS-107 payload bay configuration.

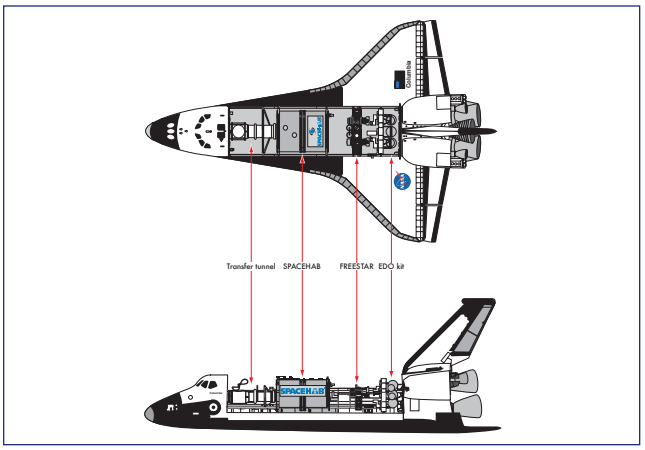

Figure 1-1. STS-107 payload bay configuration.

STS-107 was a Shuttle mission dedicated to investigating human physiology, fire suppression, and other areas of research, with 80-plus experiments representing the latest application of micro-gravity research. The seven-member crew devoted 16 days on-orbit to a mixed complement of research in the space, life, and physical sciences including biology, physics, and chemistry. Other investigations studied factors that control our terrestrial climate. Participants included several NASA centers, universities, and education and research organizations throughout the United States, along with the European Space Agency (ESA), the Canadian Space Agency (CSA), the Japanese National Space Development Agency (NASDA), the German Aerospace Research Establishment (DLR), and the Israeli Space Agency.

The primary payload carrier on STS-107 was the new SPACEHAB Research Double Module (RDM), doubling the volume available for, and significantly increasing the amount and complexity of, micro-gravity research. The RDM was a pressurized environment carried in *Columbia*'s payload bay and accessible to the crew via a tunnel from the Shuttle's middeck.

SPACEHAB Inc., via commercial contracts, enabled many universities, companies, and other government agencies to conduct important research in space on STS-107. As an example, the CSA conducted three bone-growth experiments and the DLR measured the development of the gravity-sensing organs of fish in the absence of gravity's effects. One university grew ultra-pure protein crystals for drug research while another university tested a navigation system for future satellites. The U.S. Air Force conducted communications experiments. Elementary school students in Australia, China, Israel, Japan, Liechtenstein, and the United States studied the effects of space flight on fish, spiders, ants, silkworms, bees, and even inorganic crystals.

Columbia's payload bay also housed six science payloads known as FREESTAR, which were mounted on a Multi-Purpose Experiment Support Structure bridge spanning the width of the Payload Bay (PLB). These experiments performed solar observations, earth science and atmospheric observations, fluid physics, and demonstrated new communications technology for future spacecraft. *Columbia* was also outfitted with an Extended Duration Orbiter (EDO) cryogenic pallet, which provided the required consumables for the long duration of the mission.

The Mediterranean Israeli Dust Experiment (MEIDEX), managed by the Israeli Space Agency and Tel-Aviv University, was one of the key FREESTAR experiments. The primary objective of MEIDEX was to observe dust storms in the Mediterranean and the Atlantic coast of Africa using a radiometric camera mounted in the payload bay, which was remotely controlled by the ground or astronauts in the crew cabin. Secondary objectives of MEIDEX included observations of slant visibility, sea-surface and desert-surface reflectivity, and Transient Luminous Events, such as sprites.

2.0 Launch Countdown

The STS-107 Launch Countdown (LCD) was approximately 24 hours longer than a typical International Space Station (ISS) countdown, but within the experience base of other SPACELAB or SPACEHAB-type missions. There were some differences in this countdown as compared to most LCDs, primarily because this was not an ISS mission. Some of the more significant differences were due to the Extended Duration Orbiter (EDO) pallet that provided additional electrical power generation capability for this 16-day science mission, and the fact that the SPACEHAB module had to receive final stowage late in the countdown to accommodate the live animals and other unique science payloads. Figure 2-1 details the STS-107 LCD overview flowchart.

There were no significant issues during the LCD including the Power Reactants Storage Device (PRSD) cryogenic load or EDO planned offload operations. The crew module activities were in the critical path from L-48 hours (post-PRSD) through the start of External Tank (ET) loading due to the amount of SPACEHAB and middeck stowage items. The SPACEHAB stowage activities were completed approximately 90 minutes late due to configuration issues and the significant amount of equipment to stow. However, the LCD team was back on the critical path timeline by the completion of the communication system activation (~ L-24 hours).

ET propellant loading was delayed by approximately 70 minutes (started at L-7 hours, 20 minutes) due to several factors. These factors included the fuel cell activation/calibration running longer than planned because the time allocated for this activity was not adequate for the additional cryogenic tanks on the EDO pallet. Also, the work to resolve Interim Problem Report 110 (IPR 107V-0110), which was written to document a Liquid Oxygen (LO2) replenish valve problem, required access to the Mobile Launch Platform (MLP) and delayed preparation for ET

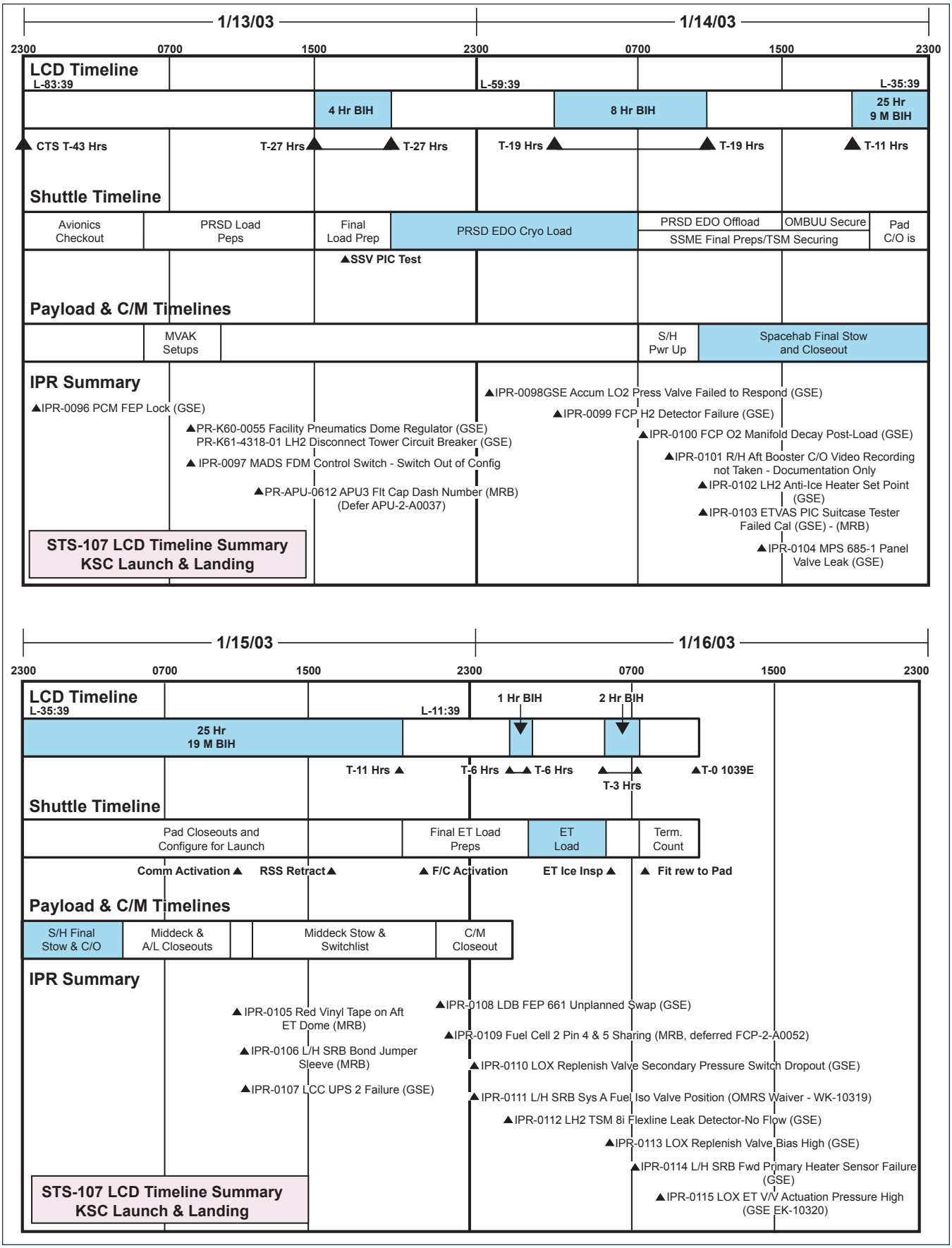

Figure 2-1. STS-107 launch countdown (LCD) overview flowchart.

LO2 filling operations. As a result of troubleshooting for another IPR (IPR 107V-0108, Front-End Processor (FEP) 661 Unplanned Swap), a Launch Processing System (LPS) reconfiguration of the active/standby launch data bus FEP power supplies was required to provide power redundancy for ET loading.

LO2 and LH2 tank loading were both normal, and all loading cycles were within previous experience. According to postflight analysis, at the end of propellant loading (end of replenish), the LH2 tank load was 231,035 pounds mass (lbm), and the LO2 tank load was 1,382,980 lbm. The postflight analysis includes corrections for the specific ET volume for both tanks and helium injection density corrections for the LO2 tank.

The post-ET load Ice Team inspection was performed with no significant issues noted relative to previous inspections. The inspection began at 6:15 EST and finished at 7:45 EST. The weather conditions at the start of inspection were as follows: temperature 48 degrees Fahrenheit, relative humidity 97 percent, winds from 290 degrees at 5 knots. One item of interest was noted with respect to the –Y (left) bipod ramp closeout area (see Figure 2-2 for vehicle coordinate system orientation). The Liquid Hydrogen (LH2) section of the Ice Team report noted that there were visual indications of frost along the bondline of the ET –Y bipod, and that the frost dissipated by 7:15 EST, after sunrise. The ET bipod assembly is located at the forward ET/orbiter attach point, and indications of frost are not unusual in this area.

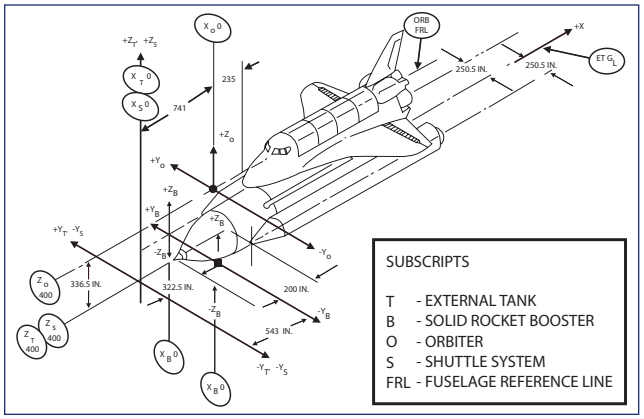

Figure 2-2. Shuttle vehicle coordinate system.

The postlaunch debris walk down was performed at the launch pad per Operations and Maintenance Instruction (OMI) S6444, and no unusual debris or damage was noted. All IPRs and Problem Reports (PRs) recorded during the LCD were evaluated and three were noted as worthy of discussion since they involve possible ascent debris or the ET. The first, IPR 107V-0102, LH2 Anti-Ice Heater Failed Set Point, was written to document a Ground Support Equipment (GSE) heater that did not control to the required set point within the specified time. The Alternating Current (AC) phasing was found incorrectly wired due to a previous modification. The associated power leads were swapped and retested on the second day of the LCD without incident. This system performed nominally for the remainder of the LCD.

The second item, IPR 107V-0105, Red Vinyl Tape on Aft ET Dome, was written to document a small piece of red vinyl tape (1 in. by 1.5 in.), similar to that used in Solid Rocket Booster (SRB) closeout activity, which was found adhered to the +Y side of the ET LH2 aft dome (Y-Y axis approximately 1 ft aft of station XT2058) during the L-1 day walk down. There was no visible Thermal Protection System (TPS) damage noted in the vicinity of the tape. The tape was accepted to use as-is via the Material Review Board (MRB) process. The rationale was that the tape was limited in size and mass, presented no adverse effect to the TPS performance, and was outside of the critical debris zone since it was located on the very bottom part of the ET.

The third item was IPR 107V-0106, Booster Bond Jumper Sleeve Not Removed. This IPR was written for a part marking identification sleeve found on the systems tunnel ground strap 5 feet below the aft web of the right booster ET attach ring near the booster factory joint Xb-1577. The small plastic sleeve was accepted via Material Review (MR) board to use "as-is," because the sleeve and strap would not be affected by aero heating, and if the sleeve melted or tore away during ascent, its trajectory would be outside the orbiter debris zone.

3.0 Launch

3.1 Introduction

This section discusses the launch and ascent phases of STS-107 in four separate sections. The first section outlines some general launch conditions and an introduction to the ET bipod foam impact, including photographic and debris transport analyses, as well as RCC impact testing and analyses. The next section discusses several key MADS measurement signatures from the ET foam impact timeframe. This is followed by a summary of launch and ascent radar, and corresponding analyses. The final section is a detailed discussion of several orbiter Guidance, Navigation, and Control (GNC) system events of interest from the ascent timeframe. These include wind shear, ascent loads, ET propellant slosh, and SSME and SRB nozzle positions. The discussion centers around possible correlation of these events with other families of flights, including the family of flights where it is known that ET bipod foam loss occurred.

3.2 Launch Debris Impact Observation

3.2.1 Launch/Ascent Conditions

Launch occurred at the Kennedy Space Center (KSC), launch pad 39A, on January 16, 2003, at 10:39 EST (see Figure 3-1). The weather at pad 39A, 60-foot level was: temperature 65 degrees Fahrenheit, relative humidity 68 percent, dew point 59 degrees Fahrenheit, with calm winds. Figure 3-2 shows the STS-107 reconstructed altitude data and Figure 3-3 shows the mach number and dynamic pressure during first stage, prior to Solid Rocket Booster (SRB) separation, as a function of Mission Elapsed Time (MET).

Figure 3-1. Launch of STS-107 from pad 39A at Kennedy Space Center.

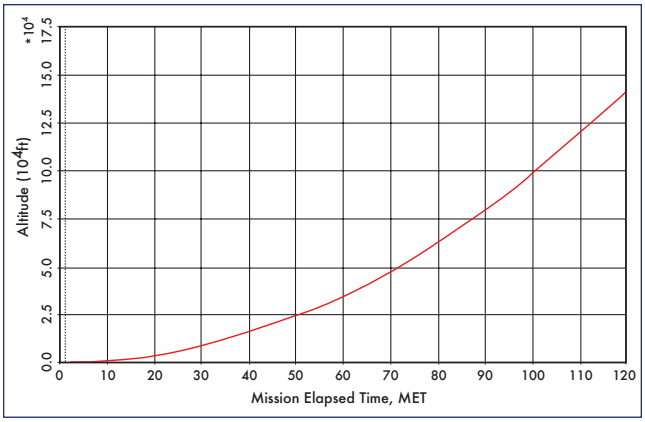

Figure 3-2. STS-107 reconstructed altitude during first stage (prior to SRB separation).

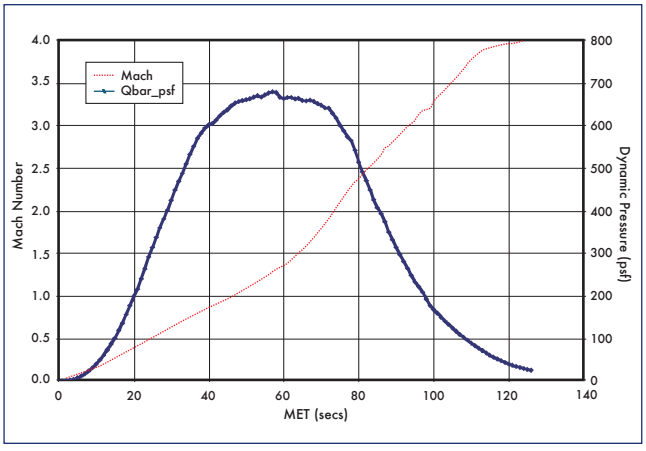

Figure 3-3. STS-107 flight reconstruction data for mach number and dynamic pressure (Q-bar) prior to SRB separation. Note that Q-bar is highest during first stage (prior to SRB separation), and reduces to a very small number after SRB separation.

3.2.2 Launch Debris Impact Area

Postlaunch photographic analysis determined that one major piece of foam and at least two minor pieces departed the External Tank (ET) left bipod ramp area approximately 82 seconds after launch. The primary foam piece impacted *Columbia* in the vicinity of the lower left wing Reinforced Carbon-Carbon (RCC) panels 5 through 9 at 81.86 seconds after launch. There were no indications that any of the minor pieces impacted the left wing based on their post-separation trajectories. The orbiter was at an altitude of ~65,860 feet, traveling at Mach 2.46 at time of impact.

Several approaches were taken to assess the area of left wing damage. The efforts included launch video and photograph analysis, review of launch MADS data, debris transport analysis, forensic analysis of debris found in Texas, wire bundle burn through analysis, and aero/thermal modeling of the entry. The data indicate that the area of the highest probability of damage to the left wing was between RCC panels 5 and 9, with the most likely damage occurring on the lower side of RCC panel 8 or an adjacent Tee seal. The damage was most likely equivalent in size to a 6 to 10 inch diameter hole or area broken from the RCC panel or an adjacent Tee seal. Figure 3-4 shows the area of highest probability of wing damage and Table 3-1 shows the methods used to determine the damage.

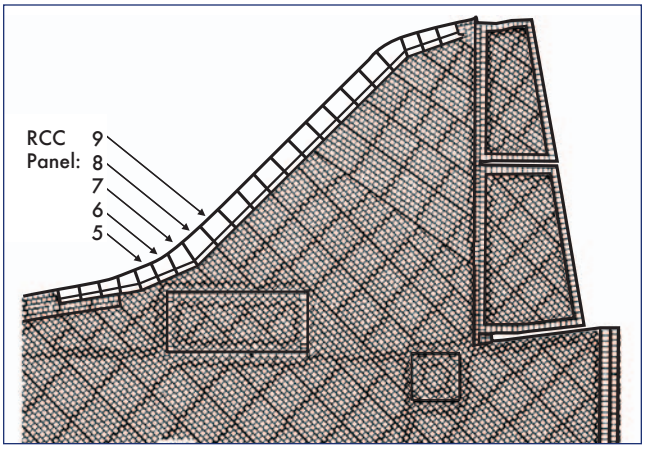

Figure 3-4. Area of most likely wing damage.

3.2.3 Launch Photo and Transport Analysis

Photographic analysis of the debris impact event included participation from the Johnson Space Center, the Marshall Space Flight Center, the Kennedy Space Center, Lockheed Martin Management and Data Systems, Boeing NASA Systems, the Eastman Kodak Company, and the National Imaging and Mapping Agency.

Video and Computer-Aided Design (CAD) analysis determined that the most likely impact location was leading edge RCC panels 6 through 8 (Figure 3-5). Due to the foam size, RCC panels 5 and 9 must also be included in this impact zone. The best estimate of the foam size, based on imagery measurements, is 21 to 27 inches long and 12 to 18 inches

Wing Damage Analysis Method	*Predicted Damage Area*	*Comments*	*Discussion Found In Section*
Launch Video and Photo Analysis	RCC 5 through 9	Most likely area of impact was RCC panels 6 through 8.	3.2
Ascent MADS Data	RCC 6 through 8	Unusual temperature sensor data observed on spar behind RCC panel 9, and temperature rise matches a thermal math model of a 10 inch diameter hole in RCC panel 8.	3.3
Debris Transport Analysis	RCC 5 through 8	Most likely area of impact was RCC panels 6 through 8.	3.2
Hardware Forensics Data	RCC 8 or 9	Fragments of RCC panels 8 and 9 showed extreme temperature indications, knife edge heat erosion patterns, and heavy amounts of slag deposited on the insides of those panels.	5.3
Entry MADS Data	RCC 8 or 9	First unusual indication observed during entry was a strain gauge behind RCC panel 9 (could be due to a strain behind adjacent panel 8).	5.4
Wire Bundle Burn Through	RCC 7 through 9	Burn through from locations forward of panel 7 or aft of panel 9 are very unlikely based on sensor data loss timing.	5.4
Entry Aero/thermal Modeling	RCC 8 or 9	Based on wind tunnel test results and CFD analysis.	5.5

Table 3-1. Wing damage analysis methods and results.

wide. The precise foam shape and thickness cannot be determined from the available imagery; however, a reasonable estimate is that it was a plate-like shape and several inches thick. The foam tumbled at a minimum rate of 18 times per second based on the imagery, although the actual rate may never be known more accurately. Figure 3-6 illustrates a portion of the photographic analysis techniques used to determine the size of the foam.

The most useful video analysis was performed using two cameras that are part of the Eastern Launch Range imaging system. Camera E212 (film), located on the Cape Canaveral Air Force Station, was approximately 17 miles from the orbiter at the time of foam impact and Camera ET208 (video),

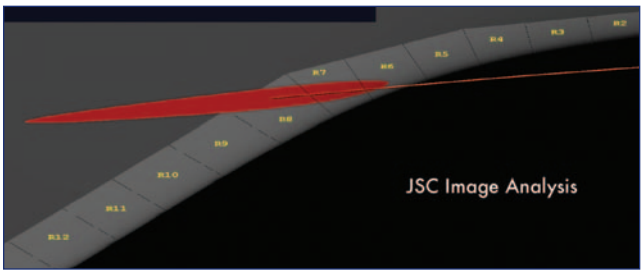

Figure 3-5. Multiple analyses determine foam impacted lower RCC panels 6 through 8 area.

located in Cocoa Beach, Florida, was 26 miles from the orbiter. The overall camera geometry relative to the launch pad and ascent flight path is shown in Figure 3-7. Camera E212 had a better view of the topside of the launch vehicle, while Camera ET208 had a better bottom side view. Figure 3-8 depicts the view from each of the camera systems. A third camera, E208 (film), also recorded the launch but was blurred and contained no useful data for the investigation. There are no Launch Commit Criteria (LCC) regarding cameras, or camera views for ascent, for either onboard or ground.

Figure 3-6. Photographic analysis techniques determined foam size: debris appears almost circular in frame 4914 and elongated in frame 4919.

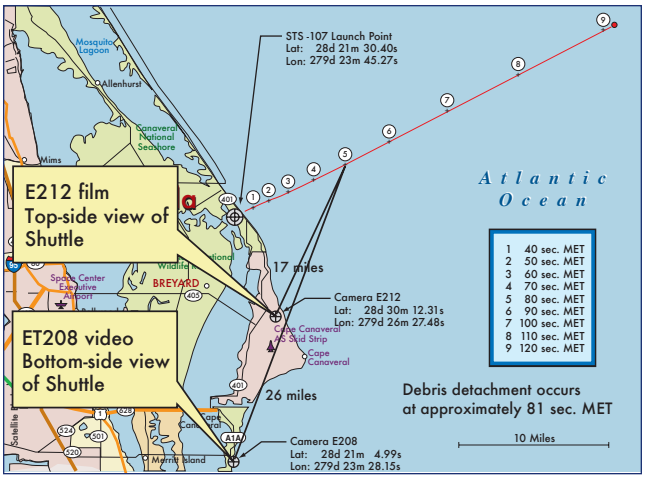

Figure 3-7. Camera geometry for ascent video analysis; note that video camera ET208 is at same location as film camera E208.

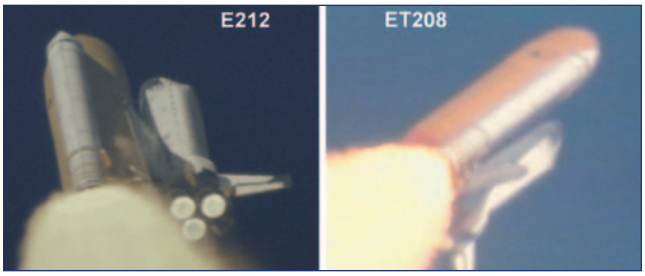

Figure 3-8. Orbiter view from cameras E212 and ET208.

There is significant visual and debris trajectory information to implicate the left bipod ramp area as the source of debris. In Figure 3-9, the red line depicts the estimated foam trajectory as it moved from the bipod ramp area toward the left wing. In addition to locating the impact in the RCC panels 6 through 8 region, the video analysis has also shown that the impact was below the apex of the RCC panels since no foam or post impact debris was observed to traverse over the top of the wing. This is indicative of an impact below the wing leading edge aerodynamic stagnation line (Figure 3-10). The stagnation line, or dividing streamline, is the line along the leading edge of the wing where the airflow comes to rest; above this line, airflow moves over the upper wing surface and below this line, the airflow moves over the lower wing surface.

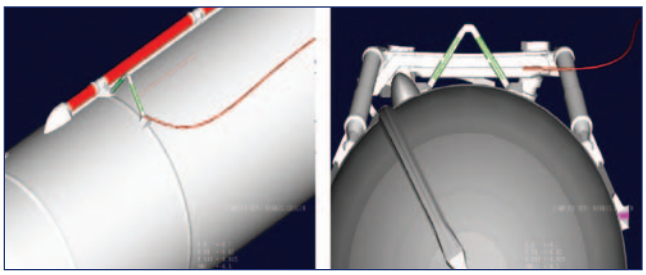

Figure 3-9. Multiple analyses indicate foam is from ET left bipod area. Red line depicts the estimated foam trajectory as it moved from the bipod ramp area toward the left wing.

Enhancements of the ascent video indicated there was no discernable damage to the orbiter wing leading edge or lower tile surface. Figure 3-11 is a sample of these video enhancements. The figure compares 30 pre-impact integrated video fields with 21 post-impact integrated video fields. Based on these enhancements, photo experts have been unable to determine or quantify any damage to any portion of the orbiter vehicle as a result of the impact.

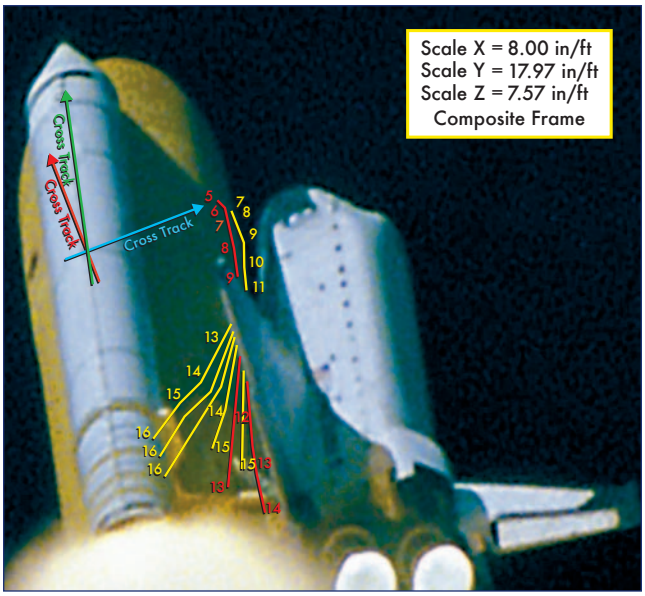

Figure 3-10. Video analysis shows impact is below wing leading edge stagnation line. Trajectories of particles are depicted after the impact.

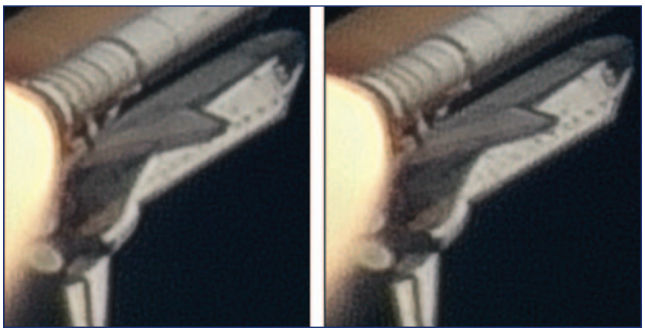

Figure 3-11. Pre-impact vs. post-impact shows no observable damage within the resolution limits.

3.2.4 Debris Velocity and Size Assessment

In addition to size and location of the foam impact, there are several other parameters necessary to complete the post-flight analysis of possible impact damage. These include an estimate of the foam's mass, relative velocity at impact, rotational energy, and the angle of impact with respect to the Shuttle wing at the point of impact. These parameters combine to determine the amount of impulse imparted at impact and are therefore critical to determine whether there was possible damage to the RCC panel, associated attach fitting hardware, or other leading edge structure.

	Transport Analysis Lower Bound	Transport Analysis Upper Bound	ET Working Group Estimate	RCC Impact Testing Target
Ballistic Number (BN)	1.2	1.45	1.0	1.45
Velocity (ft/sec)	820	775	850	775
Volume (in^3) @ 2.4 lb/ft^3	1,025	1,240	855	1,200
Weight (lbs) @ 2.4 lb/ft^3	1.42	1.72	1.19	1.67

Table 3-2. Transport analysis and ET Working Group estimates of ET bipod debris size, weight, and volume.

Photographic analysis was used to establish a range of relative impact velocities, from 625 to 840 feet per second (416 to 573 miles per hour). This large uncertainty is due to the small number of video and film frames between release of the foam and impact with the wing, since the estimated time between the foam release and foam impact is only 0.2 seconds. The predominant direction of motion is toward the aft of the orbiter along the X-axis, although the foam is moving slightly outboard at the time of impact with little to no motion in the Z-axis (see Figure 2-2 for vehicle coordinate system orientation). The direction of motion is from the ET bipod area toward the left wing at an angle of 2 to 10 degrees with respect to the orbiter X-axis in the orbiter X-Y plane. The motion is slightly toward the wing surface at a 0 to 3 degree angle measured in the orbiter X-Z plane.

Three-dimensional trajectories from the launch films and videos were refined using a physics-based trajectory fit that included a realistic flow field model generated using computational fluid dynamics (CFD) techniques. These results indicated that the relative velocity at impact was in the range of 775 to 820 feet per second. The CFD analysis used numerical methods to model the flow field around the orbiter/ET/Solid Rocket Booster (SRB) stack including the SRB and Space Shuttle Main Engine (SSME) plumes. An example of this analysis is shown in Figure 3-12.

The transport analysis was also used to estimate a range of sizes and corresponding weights for the foam, which are summarized in Table 3-2. For an impact velocity of 820 feet per second, the estimated foam volume is approximately 1025 cubic inches with a weight of 1.42 pounds assuming the density of the foam was 2.4 pounds per cubic foot. Similarly, for a velocity of 775 feet per second, the estimated volume is 1240 cubic inches, and the resulting weight is 1.72 pounds. Additional results produced with a more complex CFD model included lift forces and the unsteady rotation of the debris. Table 3-2 also lists the ET Working Group estimate of the bipod foam size and weight. This estimate was for one particular ET bipod ramp configuration and did not account for manufacturing variability. Thus, it was not used as the volume for the RCC impact testing, and more details are included in Section 11.

Numerous factors could affect mass of the foam debris, and the exact volume and mass may never be known. For example, the BX-250 foam could have had a higher than predicted density of 2.4 pounds per cubic foot, since the density can range from 1.8 to 2.6 lb/ft^3. Alternatively, a lower drag coefficient on the debris could also account for a higher ballistic number (BN).

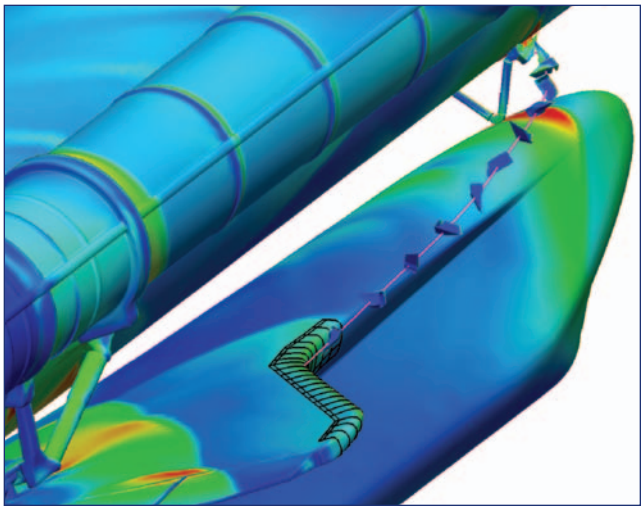

Figure 3-12. Sample CFD flow field with debris modeling.

3.2.5 Impact Damage Testing and Analysis

Analysis and experimental results were used to assess the potential for debris impact to damage *Columbia*'s wing leading edge. The overall concept was to replicate, to the greatest extent feasible, the debris impact event that occurred on *Columbia*'s left wing during ascent, by impacting flight-ready composite panel assemblies with a representative foam projectile fired from a compressed gas gun. The target panel assemblies had a flight history similar to that of *Columbia*, and were mounted on a support structurally equivalent to *Columbia*'s left wing. The attaching hardware and fittings were either flight certified, or built to *Columbia*'s drawings. BX-250 foam, without entrained ablator material, was used for the impacting projectile material because it represented the ascent event and provided a lower bound damage assessment. After significant study and consideration of all inputs by the NAIT and CAIB members, the parameters for representative impacts were established as: foam volume 1200 cubic inches, velocity 775 feet per second, and foam mass 1.67 pounds.

Impact testing has been completed on full size fiberglass panels, an RCC panel 6, and an RCC panel 8 to obtain insight and experimental data important to the understanding and modeling of the response of the wing leading edge components. The RCC panel 6 assembly was from *Discovery* and had flown 30 missions, and the RCC panel 8 was from *Atlantis* and had flown 27 previous missions.

The test of the RCC composite panel assembly 6 demonstrated that a foam impact representative of the debris strike at 82 seconds was capable of damaging RCC material. A 5.5-inch crack was created, extending from a visible 3/4 inch diameter damage area on the outside of the panel to the rib inside the wing. The panel 6/7 Tee seal was also damaged with a 2.5-inch crack, and the Tee seal as well as panel 6 were shifted in position. In addition, a carrier panel on the upper side of the wing was chipped.

Subsequent engineering testing has demonstrated that the localized impact loads imposed on the panel 6 assembly would have been substantially higher with changes in foam impact orientation and location. These changes were included in the RCC panel 8 assembly test and included a 30 degree clocking angle (orientation of the foam projectile relative to the target), a 22 degree angle relative to the impact surface, and an impact location lower and farther outboard relative to the panel 6 test. Impact target location was six inches farther down the trajectory track from the earlier tests. The test generated a 16 inch by 16 inch hole in the lower surface of panel 8, which is the most substantial damage to date in any RCC impact test.

The exact flight damage is unknown but is believed to be bracketed by these two tests. The testing is important in that it confirms that the ET bipod foam can catastrophically damage the RCC.

3.3 Launch MADS Data

There are two other indications that the foam impact occurred in the panels 6 through 8 area. Two Modular Auxiliary Data System (MADS) lower surface pressure measurements behaved anomalously immediately after the time of the impact. Figure 3-13 shows the location of these measurements along with possible areas for post-impact debris re-contact in the vicinity of the sensors. The unusual behavior of one of the sensors is shown in Figure 3-14.

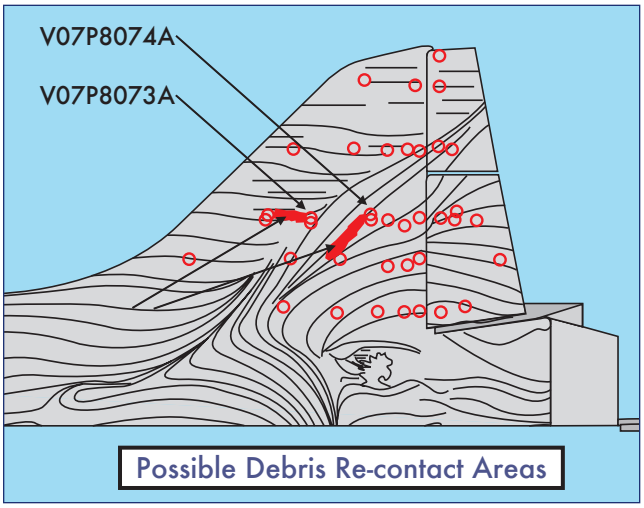

Figure 3-13. CFD surface flow with lower left wing pressure sensors.

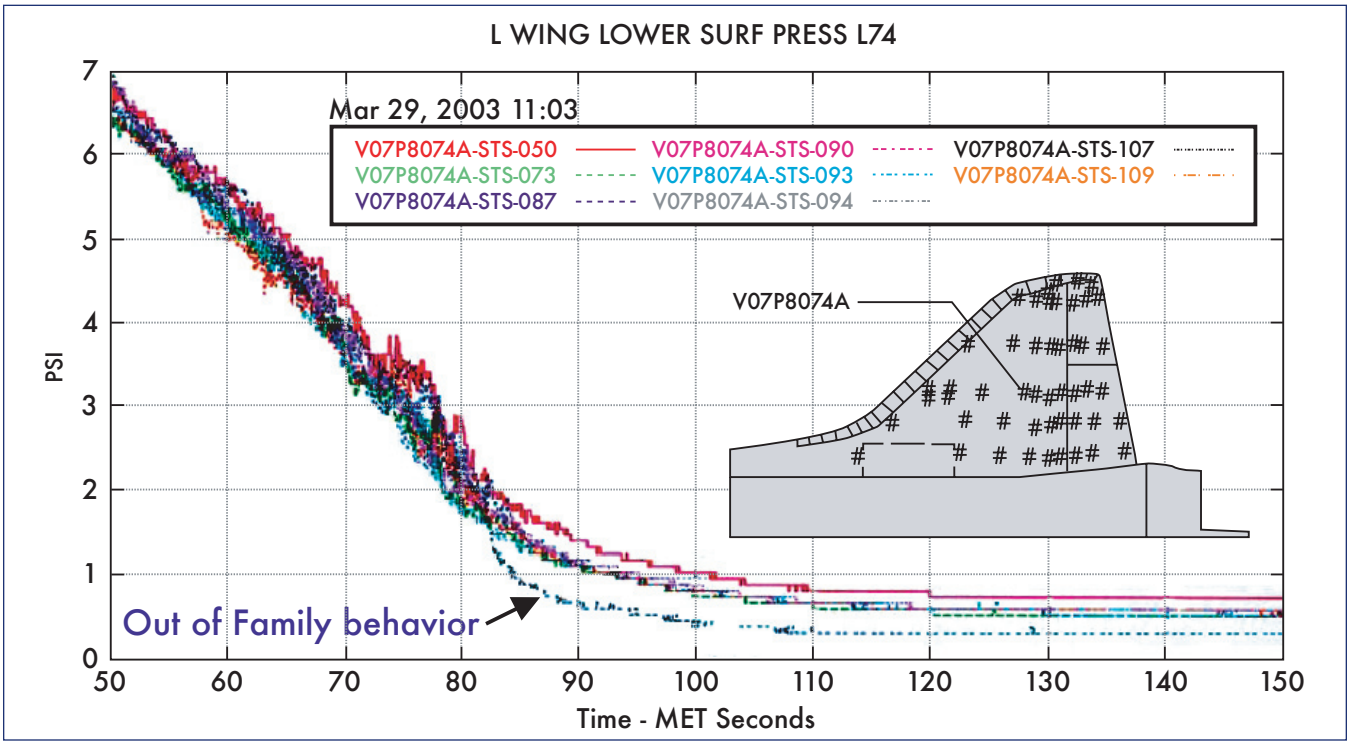

Figure 3-14. Unusual behavior of pressure sensor V07P8074A.

Additionally, there is another MADS measurement that had an off-nominal signature during the ascent timeframe. The temperature sensor on the leading edge spar behind RCC panel 9 showed a slightly higher temperature rise than seen on any previous *Columbia* flight. Figure 3-15 shows the location of the temperature sensor behind the wing leading edge spar inside the wing. The slight temperature rise can be seen in Figure 3-16. Note that most flights show a small rise in this temperature during ascent due to aerodynamic heating.

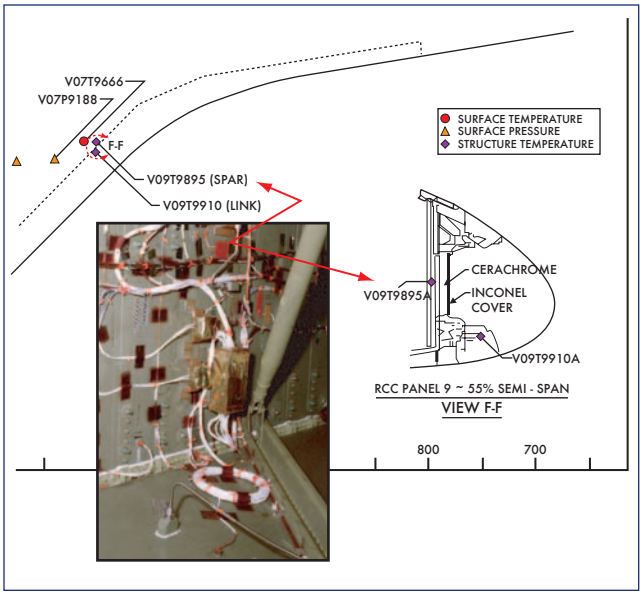

Figure 3-15. Close-out photo shows RCC panel 9 wing leading edge temperature measurement.

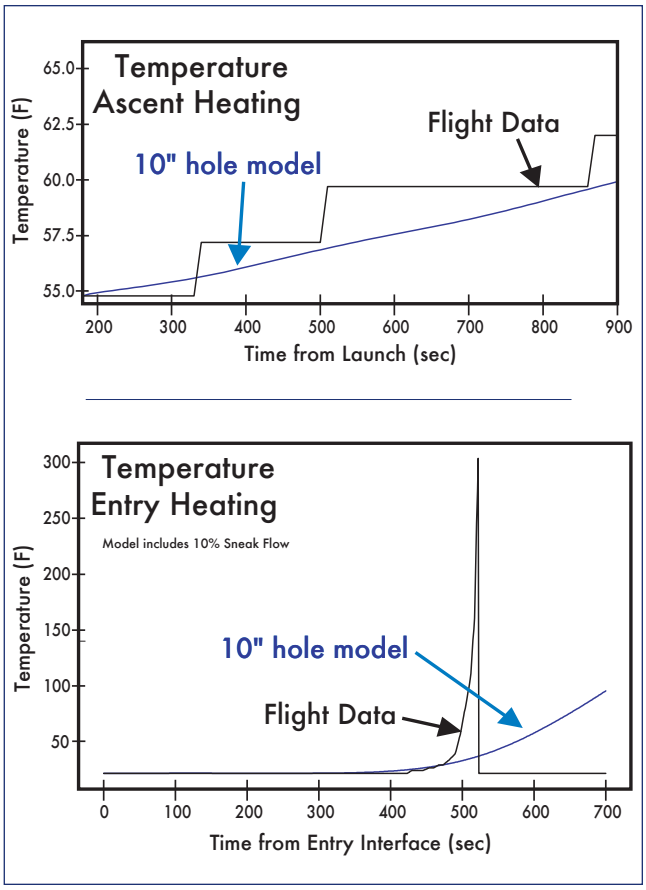

Figure 3-17. Correlation between simplified thermal math model and STS-107 ascent and entry flight data.

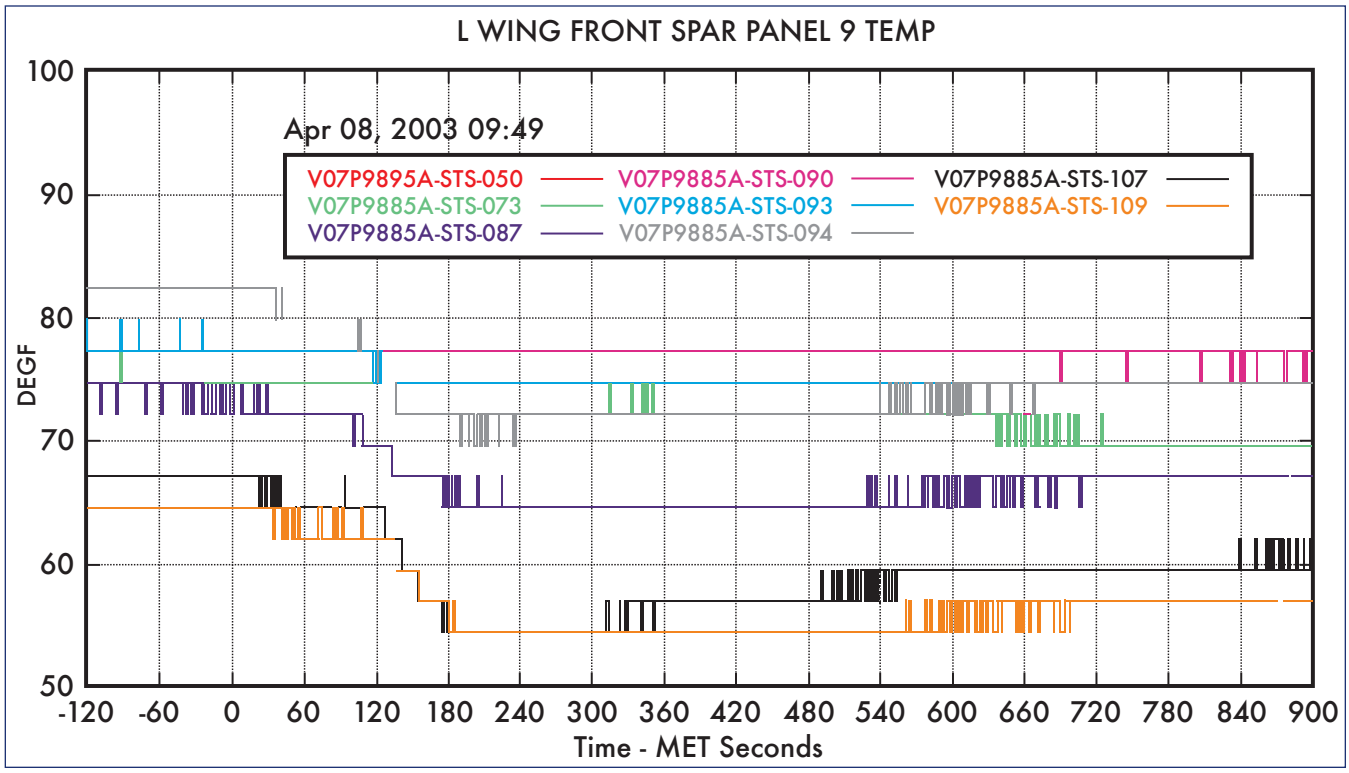

Figure 3-16. Three-bit rise (7.5 degrees F) on MADS wing leading edge spar temperature measurement (V09T9895A) during ascent.

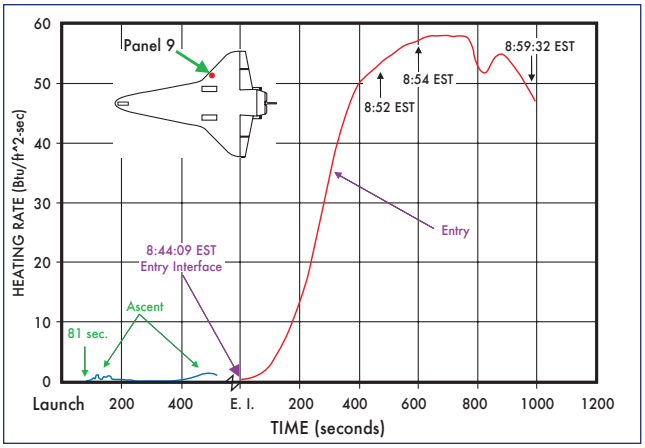

Figure 3-18. STS-107 ascent and entry heating environments on RCC panel 9.

STS-107 had a 7.5 degree Fahrenheit rise that started very early during ascent (five to six minutes after launch). Although the data do not prove that the RCC was breached during ascent, the data are consistent with a possible flow path into the RCC cavity via damage in the RCC panels 6 through 8 area. A simplified thermal math model was constructed and verified with flight data from STS-5. The model was then correlated to the flight data from STS-107. Assuming the equivalent heating from a 10 inch diameter hole in RCC panel 8, this model nearly predicts both the ascent and entry temperature profiles for the wing leading edge spar temperature sensor. Figure 3-17 compares the model with the flight data for both ascent and entry. For comparison, Figure 3-18 shows the overall heating rate of the STS-107 ascent and entry environments on RCC panel 9. As shown, the heating on the wing leading edge is much greater during the entry profile than during the ascent profile.

3.4 Launch Area Radar Analysis

STS-107 was tracked during ascent by the Eastern Range (ER) land-based C-Band radars, and identified debris was analyzed for time of separation, radar cross section (RCS), and range separation rate. In summary, the radars were unable to detect debris prior to SRB separation. Following SRB separation, from Launch + 150 to L + 230 seconds (2:30 to 3:50 Mission Elapsed Time, MET), 46 items were catalogued, of which 27 items are considered to be debris; however, the radar return signal was not of sufficient strength to determine the approximate shape, size, or rigidity of the debris. The radar analysis results are consistent with the debris analyses from previous STS missions. Table 3-3 lists the STS-107 catalogued radar detected events.

The launch radar is optimized for range safety and vehicle trajectory determination, and not for small debris assessment. A better radar for small debris, the Multiple-Object Tracking Radar (MOTR) was not available for use on STS-107. The ER radars used on STS-107 were not designed for signature analysis and were not able to lock onto and track multiple targets simultaneously. Additionally, debris could remain undetected if the debris was emitted at a time and angle where it was shielded from the radar by the vehicle body.

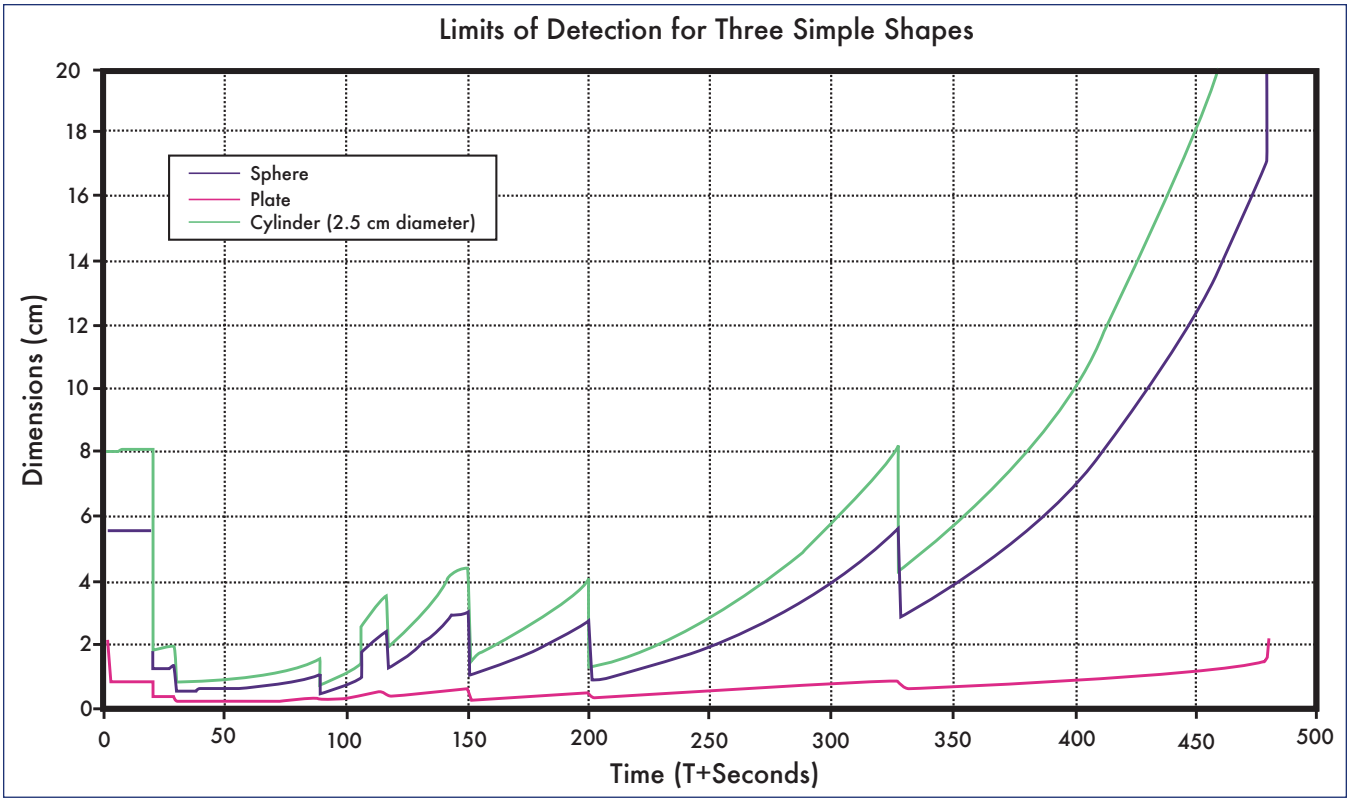

Figure 3-19. Limits of dimensional detectability for three simple shapes.

Catalog number	Radar source (site no.)[a]	First / last appearance (T + sec)	MAX RCS[b] (dBsm)[c]	Separation rate (m/sec)	Lower RSR[d] (m/sec)	Upper RSR[d] (m/sec)
1 [e]	0.14	80.4/87	8	14	44	541
29 [e]	19.14	81.6/86.1	-1	30	36	688
34	19.14	117/121	-15	771	10	1268
30 [f]	0.14	117.5/118	-8	1240	0	1162
31 [f]	28.14	117/118.5	-11	1500	3	616
32	28.14	118/119	-8	350	0	622
35	19.14	121/122	-16	771	4	1286
36	19.14	121/125	-16	372	6	1289
37	19.14	121/123	-15	426	4	1286
38	19.14	123/126	-14	424	1	1294
39	19.14	124/126	-14	480	3	1297
40	19.14	126/127	-12	490	2	1303
41	19.14	126.5/128	-13	490	2	1306
42	19.14	127/128	-14	476	2	1307
43	19.14	128/129	-13	570	0	1310
33	28.14	128/130	1	520	1	710
44	19.14	129.5/131.5	-14	670	2	1320
45	19.14	130/132.5	-15	371	4	1324
46	19.14	130.5/131.5	-13	370	2	1320
23	28.14	152/158.5	-12	187	13	947
2	0.14	152.5/156	-10	210	9	1405
3	0.14	152.5/162.5	-8	326	26	1405
4	0.14	153/160	-9	229	104	1505
24	28.14	154.5/162	-14	400	15	975
5	0.14	156/170	-16	217	38	1465
6	0.14	158.5/171	-17	309	34	1477
7	0.14	164/170	-17	312	17	1493
8	0.14	166.5/173	-21	357	19	1513
25	28.14	167/176.5	-18	221	22	1106
9	0.14	167/184.5	-15	260	53	1557
10	0.14	170/184.5	-15	265	44	1568
11	0.14	174.5/180	-14	290	17	1568
12	0.14	173/180	-16	206	21	1562
13	0.14	174/175.1	-16	244	2	1546
14	0.14	175.5/180	-15	180	14	1572
15	0.14	178/180	-14	296	8	1583
26	28.14	179/187.5	-10	884	22	1221
16	0.14	184/190	-14	236	19	1643
17	0.14	187/192.7	-11	649	19	1665
27 [g]	28.14	201/207	Low signal	Low signal	18	1438
28 [g]	28.14	205/208.5	Low signal	Low signal	11	1468
18 [g]	0.14	204.5/210	Low signal	Low signal	20	1812
19	0.14	204.5/214	-18	326	36	1829
20	0.14	204.5/212	-17	166	28	1820
21	0.14	206/212	-18	225	22	1827
22	0.14	211.5/228	-17	219	66	1926

a - Radar source: 0.14 = Patrick Air Force Base (PAFB), 19.14 = Kennedy Space Center (KSC), 28.14 = Jonathan Dickinson Missile Tracking Annex (JDMTA)

b - Radar cross section (RCS)

c - Decibels relative to one square meter (dBsm)

d - range separation rate (RSR)

e - Objects 1 and 29 are explained as plume artifacts evident by low separation rates from vehicle

f - Objects 30 and 31 are probably SRB slag ejection evident by high separation rates from vehicle

g - Objects 27, 28, and 18 had indeterminable RCS and RSR due to low level of signal returns

Table 3-3. STS-107 ascent radar events.

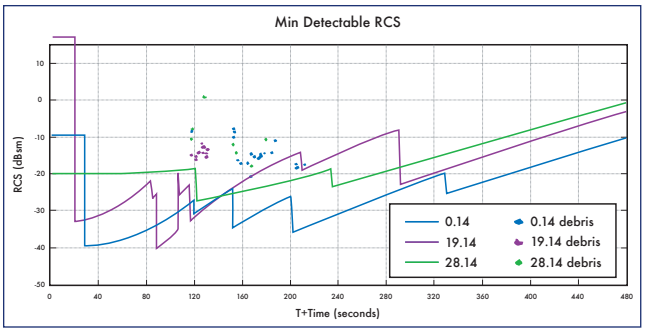

Figure 3-20. Limits of radar cross section (RCS) detectability and measured STS-107 debris for three radar source sites.

Detailed postlaunch radar debris analysis was performed on a regular basis until STS-57. There are reports available from previous flights, and typical observations include low strength radar returns from SRB separation to T + 300 seconds.

In general, the strength of the radar (C-band, AN/FPQ-14 unit) return depends on distance to the object, size of the object, and reflectivity of the object. For the STS-107 analyses, the distance to the objects is known but the object size and reflectivity are unknowns for all objects detected. As such, it was necessary to perform an exclusionary exercise to try to identify the objects. Some basic rules could be applied, such as knowledge that objects with very high separation speed are known to be part of the exhaust plume or products (such as SRB slag). In Table 3-3, items 30 and 31 were determined to be SRB slag. Moderate separation speed indicates solid objects being left behind. Separation rates can also be used to infer the density. There are limits to the debris size and shape that can be detected by the radar (see Figures 3-19 and 3-20).

From Table 3-3, debris item numbers 1 and 29 appear from 80.4 - 87 seconds and 81.6 - 86.1 seconds, respectively. This time coincides with the ET left bipod foam debris generation at 81.7 seconds. However, the low separation rate and relatively large RCS of the two radar objects indicate that they are most likely traveling with the vehicle and are flame (plume) artifacts. There are also several radar objects around the SRB separation time frame, ~126 seconds; however, the data are inadequate to determine the size, shape, or composition of the objects beyond that their moderate separation speed indicates solid objects being left behind. Some known debris objects at the time of SRB separation are the aft Booster Separation Motor (BSM) throat covers. It should be noted that the number and strength of the radar returns are typical as compared to previous Shuttle missions where no significant debris damage occurred.

In an effort to identify the STS-107 launch debris, data was reviewed from a post-STS-27 radar calibration that was performed on several materials. These objects included many applicable Space Shuttle system materials, including various orbiter thermal protection system tiles, various ET insulation foam types, as well as numerous SRB/RSRM materials and potential debris sources. Table 3-4 lists the material samples tested for Orbiter, ET, and SRB/RSRM elements. Additionally, data was used from the 2003 Wright Patterson Air Force Base testing, including Orbiter Felt Reusable Surface Insulation (FRSI), High-Temperature Reusable Surface Insulation (HRSI), and HRSI with Room-Temperature Vulcanized (RTV) sealant and Strain Isolation Pad (SIP).

As a result of the testing, the minimum detectable size for each radar return for selected materials was determined and catalogued. These data were carefully screened and scrutinized, using some reasonableness tests and assumptions, in an attempt to identify STS-107 radar objects as Orbiter, ET, or SRB/RSRM debris.

The radar data are inconclusive with respect to determining identity, size, or shape of any of the debris objects detected. The signal returns were weak and too close to radar noise to allow estimation of object shape. The number and strength of the returns on STS-107 are typical of previous Space Shuttle launches, including those where no debris damage occurred.

3.5 Launch Guidance Navigation and Control

Postflight analysis of the STS-107 ascent data revealed several events that were within the design capability of the

Orbiter	*SRB/RSRM*
Black tile	MSA-1/TPS with Hypalon
White tile	MSA-2/TPS with Hypalon
	Cork with Hypalon
ET	Aft booster separation motor (BSM) cover
PDL (closeout foam)	SRM slag
Ice plate	Cork
CPR 488 (acreage foam)	K5NA
Super Light Ablator (SLA) 561M	Instafoam
MA25	Inhibitor
BX250	EA934 adhesive
Instafoam	Viton thermal curtain
	Quartz cloth blanket

Table 3-4. Material samples from post-STS-27 radar calibration tests.

Shuttle, but considered to be new flight experience. These events were reviewed in detail, primarily because they occurred prior to SRB separation, when the foam loss and wing impact were observed. The items considered new flight experience were environmental (wind relative) side-slip angle during the period of maximum dynamic pressure (Hi-Q), SSME yaw nozzle positions during Hi-Q, and SRB thrust mismatch during SRB tail-off. Other events observed during the flight that were not new flight experience, but were considered worthy of note included the presence of a negative orbiter body yaw rate at ET separation and a period of ET slosh during powered ascent. Each event was separated into the following categories for detailed study and evaluation: wind shear, predicted versus actual vehicle loads, ET slosh, nozzle positions, and ET separation yaw rate.

Those parameters along with several other STS-107 ascent Guidance, Navigation, and Control (GNC) related points of interest were studied to determine if they were significant relative to the scenario. The study included integrated vehicle loads analysis, comparison of the STS-107 data with historical flight experience envelopes, and comparison of STS-107 data with specific families of flights. This section of the report summarizes the integrated GNC flight data review.

3.5.1 Wind Shear, Day of Launch Wind Effects

STS-107 experienced a wind shear during the period of maximum dynamic pressure starting at 57 seconds MET (Mach 1.27). The wind shear was due to a rapid change in the out-of-plane wind velocity of -37.7 feet per second over a 1200 foot altitude range starting at approximately 32,000 ft (as shown in Figure 3-21). Immediately after the vehicle flew through this altitude range, its side-slip angle began to increase in the negative direction, reaching a value of approximately –1.75 degrees at 60 seconds. This value of side-slip angle is a new flight experience value for MET 60 seconds (as shown in Figure 3-22). Post-flight data indicates that the new flight experience side slip event was not the result of the wind shear itself. Instead, it was the direct result of a difference in the L - 4:35 minutes balloon measurement, upon which orbiter guidance commands were updated on launch day, and the actual winds flown through by the orbiter during launch and ascent. Figure 3-21 highlights the difference in these two winds in this altitude region (a 25 foot per second increase in out-of-plane magnitude pre-launch compared to a 12 foot per second reduction in magnitude as experienced by the vehicle).

The L - 4:35 minutes weather balloon is launched to measure atmospheric conditions at the launch site, which are then used as part of a standard process to update the orbiter guidance software to keep it within design limits and minimize loads during ascent. After the Day of Launch I-Load Update (DOLILU) software update but prior to launch, additional balloons are used to verify that the L - 4:35 minutes balloon atmospheric conditions are still valid and meet required tolerance checks required to commit for launch. All STS-107 balloon measurements taken on launch day after L - 4:35 minutes satisfied the required launch commit criteria, and were subsequently verified by balloon data taken 15 minutes after launch.

Several theories consider this wind shear event and the difference between the balloon data to be significant. A negative side-slip angle places the wind vector on the left side

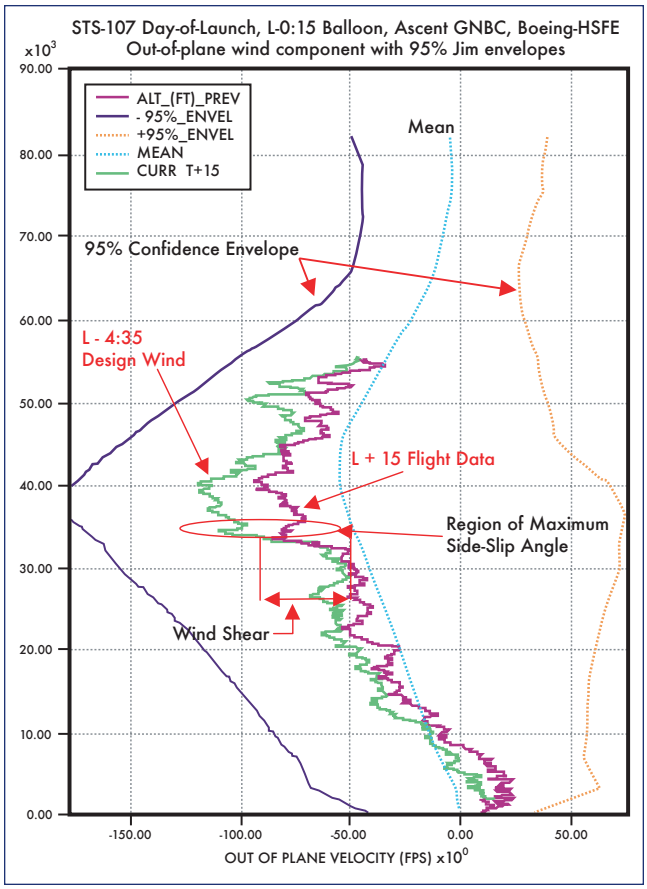

Figure 3-21. Out-of-plane wind velocity.

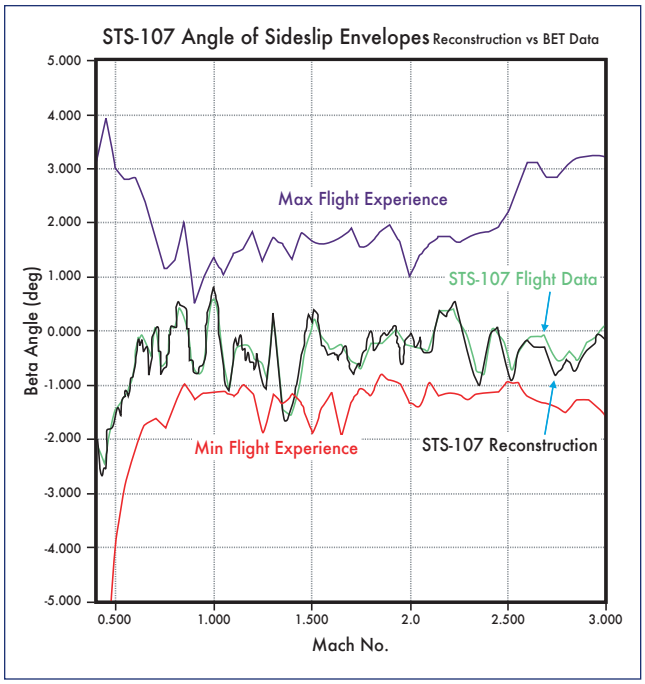

Figure 3-22. Side-slip angle.

of the orbiter, pushing the orbiter to the right, changing the complex aerodynamic flow pattern characteristics in the left ET bipod area. To better understand the conditions on the ET left bipod, several studies were conducted. The studies (1) compared flight data for missions that had ET bipod foam liberation; (2) compared flight data for missions that flew a Light Weight Tank (LWT) in combination with ascent Performance Enhancements (PEs), a package of vehicle software and hardware changes designed to increase overall weight to orbit capability for the ISS; (3) analyzed external aerodynamic loads on the ET forward attach bipod ramp; and (4) studied integrated orbiter/ET vehicle loads.

The flight data correlation studies indicate that a negative side-slip angle during the period of maximum dynamic pressure alone could not explain the liberation of the bipod foam. For both families of flights in the study (LWT and PE flights, and bipod foam liberation flights), a negative side-slip angle was seen on almost every flight. Of the bipod foam loss flights, STS-90 was of particular interest. STS-90 had a larger negative side-slip angle in Hi-Q of -2.0 degrees, when compared to STS-107, yet STS-90 did not lose bipod foam. When flights that shed bipod foam were studied as one family of flights, STS-112 is another outlier that does not support the negative side-slip angle theory. During the STS-112 ascent, video coverage shows the bipod foam liberation occurring prior to Hi-Q, yet the negative side-slip angle on STS-112 did not occur on that flight until after Hi-Q. The details of the flight data correlation studies are summarized in Sections 3.5.6 and 3.5.7 of this report.

To understand the aerodynamic loads on the ET forward attach bipod ramp, a CFD loads assessment was performed. The resulting CFD loads, discussed in more detail in Section 3.5.2, demonstrated that the external aerodynamic loads were below the design requirement.

To measure the orbiter/ET interface loads, an integrated orbiter/ET loads assessment was performed. The assessment, summarized in Section 3.5.2 of this report, also showed all integrated vehicle loads were below design limits.

The day-of-launch wind effects (including the noted wind shear event and associated negative side-slip angle) alone did not cause the ET left bipod foam loss.

3.5.2 Predicted/Actual Loads

Postflight reconstruction analysis of the STS-107 ascent loads characterized the effects of (1) RSRM thrust mismatch, (2) ET slosh dynamics, and (3) wind shear in Hi-Q. The integrated effects of these events were calculated through a flexible body loads assessment. This loads assessment used the STS-107 reconstructed ascent trajectory, and included ET slosh dynamic forces. The assessment produced (1) a wing loads summary, (2) an ET/orbiter interface loads summary, and (3) a summary of external aerodynamic loads on the ET forward attach bipod ramp.

The wing loads analysis used a flexible body structural loads assessment that was validated by the MADS data. The wing loads analysis used reconstructed trajectory parameters to generate the loads on the orbiter wings during ascent. The assessment demonstrated that all orbiter wing loads were 50 to 60% of their design limit, or less, throughout the ascent. This includes the wind shear event at 57 seconds MET, and subsequent side-slip angle at 60 seconds MET (as shown in Figure 3-23).

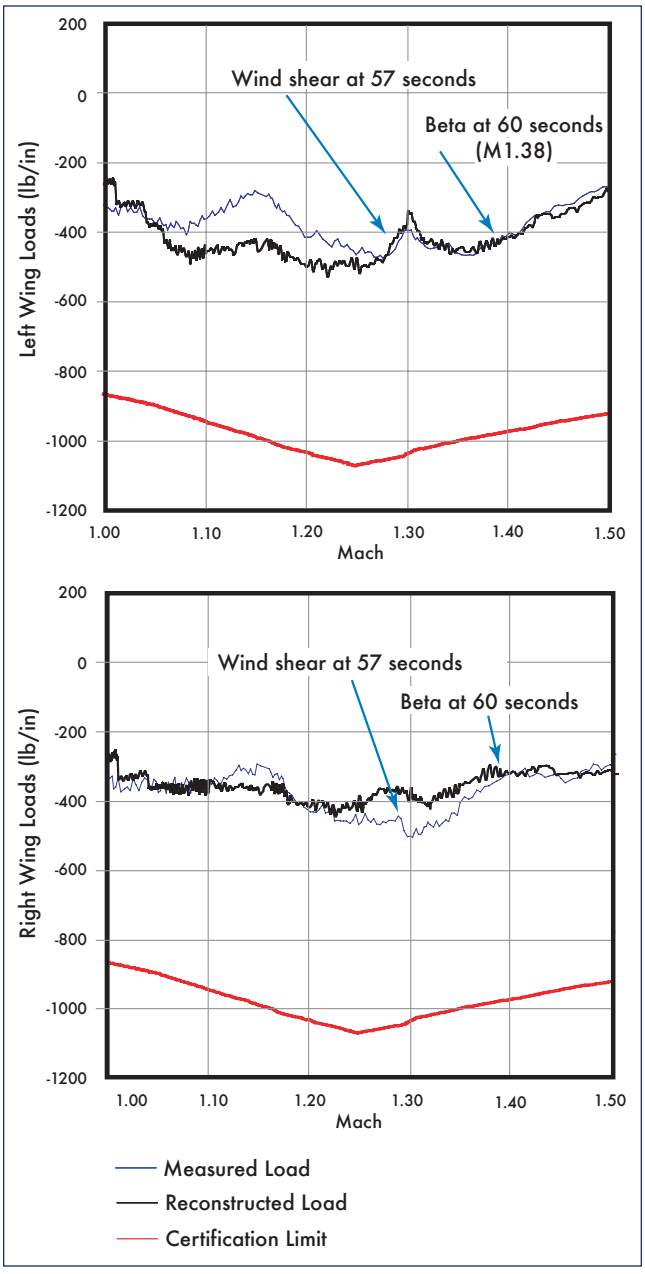

Figure 3-23. Wing loads during wind shear and side-slip angle.

The ET/orbiter interface loads were generated using reconstructed trajectory parameters that included the effects of wind shear/crosswind, side-slip angle, and ET liquid oxygen (LOX) slosh. The loads analysis demonstrated that the ET forward attach loads were within certification requirements at all times. The wind shear event had only a small effect on the overall ET loads relative to the required limits (as shown in Figure 3-24), as did the ET liquid propellant slosh

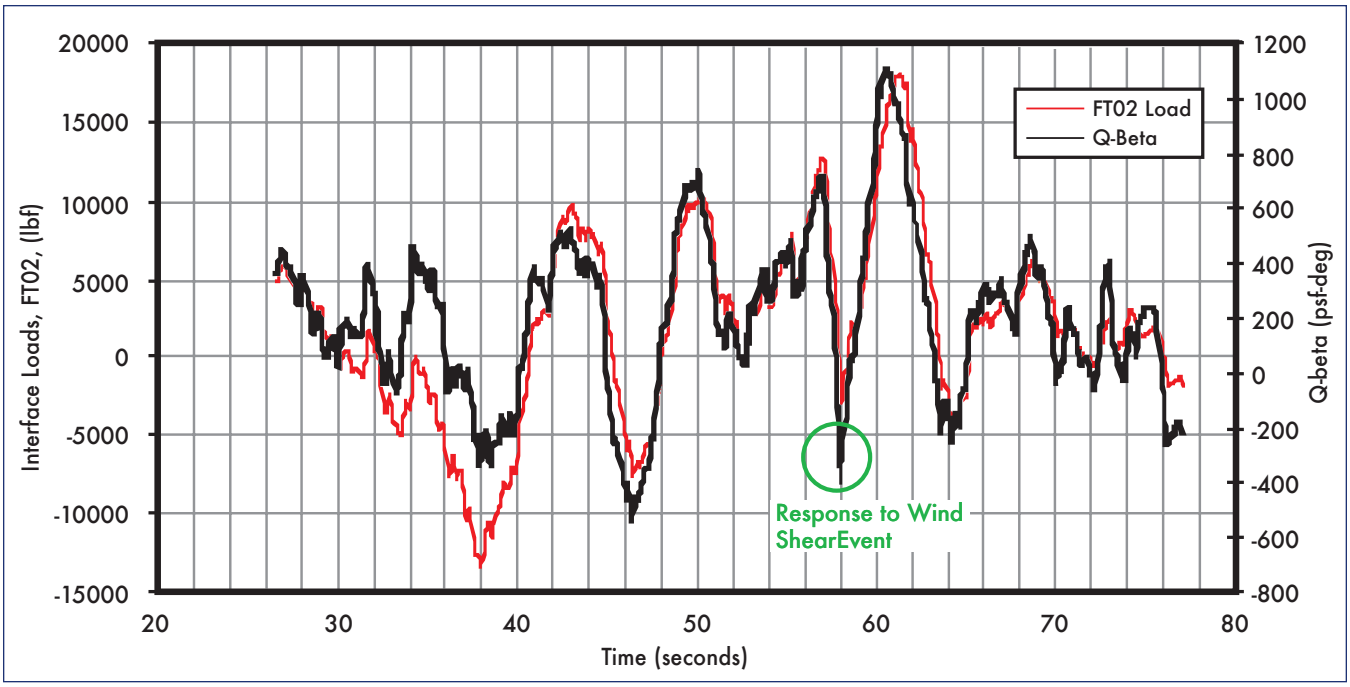

Figure 3-24. ET interface loads at forward attachment during wind shear and side-slip angle. Q-beta is side-slip angle multiplied by the dynamic pressure and represents the side-slip angle contribution of the interface load.

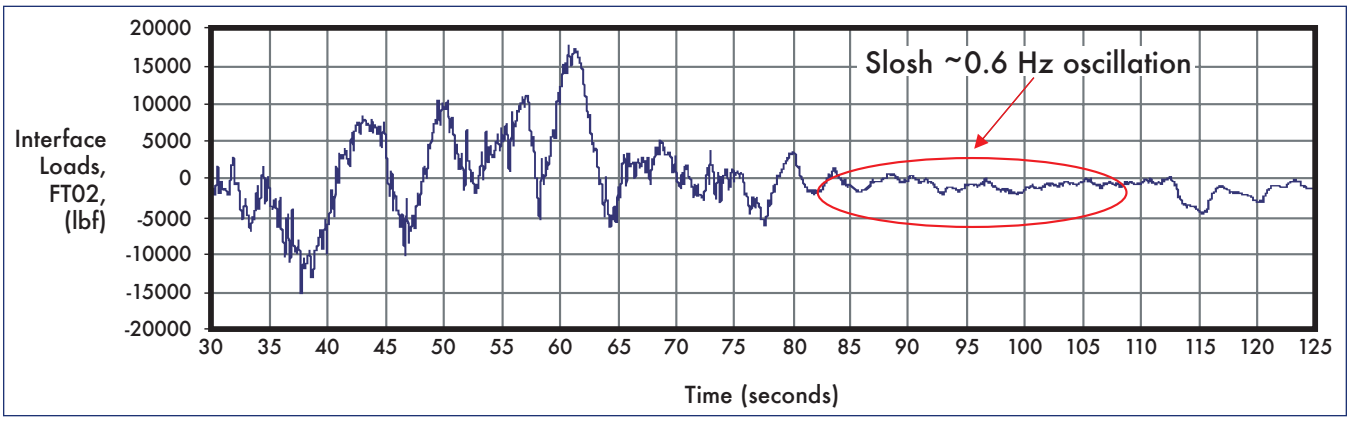

Figure 3-25. Slosh effect on ET interface loads.

(as shown in Figure 3-25). The resulting load from the wind shear event was of the same order magnitude as the roll maneuver and other first stage events prior to SRB separation.

The external aerodynamic loads on the ET forward attach bipod were analyzed using a CFD simulation. The simulation produced axial, side-force, and radial loads as shown in Figure 3-26, Figure 3-27, and Figure 3-28, respectively. The CFD assessment of the bipod area indicated that the external air loads were below the design limit during the Hi-Q region and at the time of the bipod foam liberation.

Flexible body simulation results indicate that all vehicle elements and associated loads were within required limits. The reconstruction loads analyses indicate that the ascent environment-induced loads alone did not cause the ET bipod foam loss.

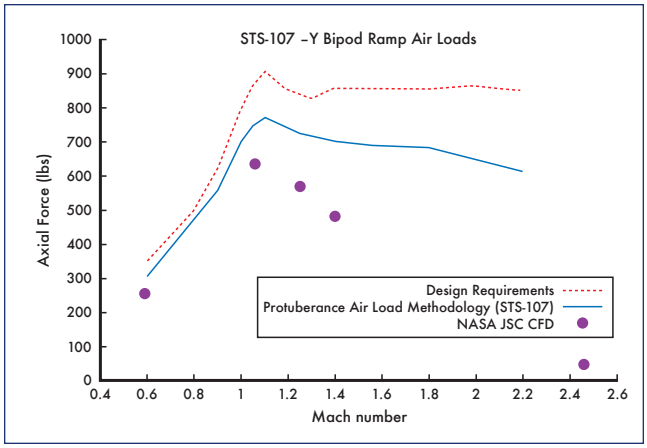

Figure 3-26. ET bipod axial aerodynamic loads.

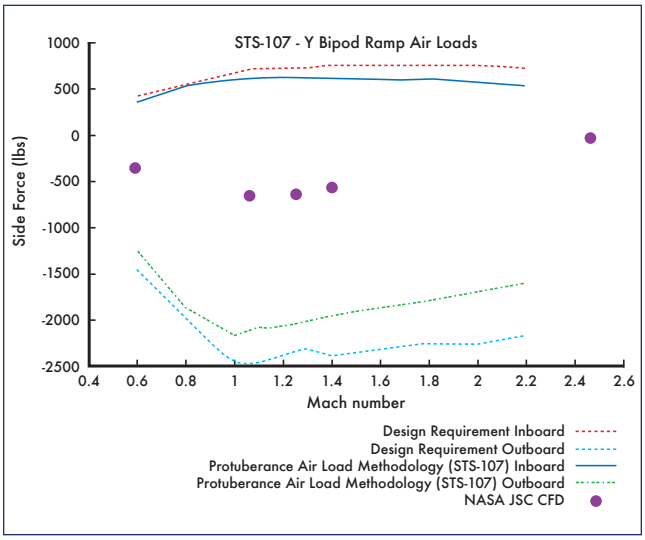

Figure 3-27. ET bipod side-force aerodynamic loads.

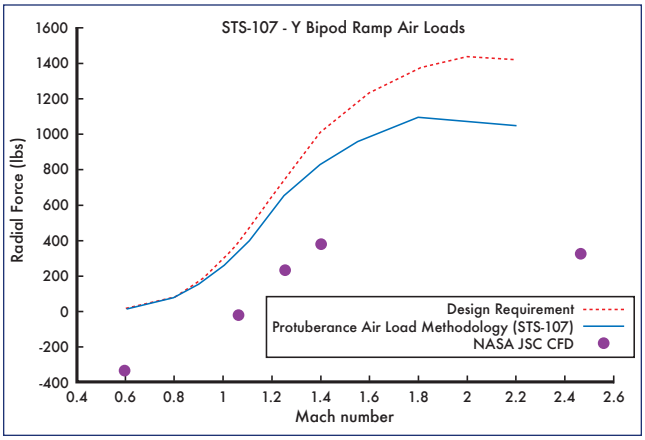

Figure 3-28. ET bipod radial aerodynamic loads.

3.5.3 ET Liquid Oxygen Slosh

The STS-107 ascent data indicate a 0.6 Hz actuator oscillation frequency that peaks in amplitude at 55 seconds, and again at 77 seconds MET and continues through SRB separation. The peaks directly correlate to peaks in 0.6 Hz wind content. A 0.6 Hz oscillation in the Flight Control System output is of interest since it can couple with the ET Liquid Oxygen (LOX) slosh mode. Slosh refers to the repeated side-to-side movement of the center of gravity of the liquid oxidizer propellant in the external tank. The slosh mode frequency and amplitude cannot be measured directly through vehicle data. In order to determine if ET LOX slosh is present, a post-flight process of reviewing the vehicle SRB and SSME actuator frequency content must be conducted, as well as that of the launch wind. When this post-flight process was conducted for STS-107, it revealed that this flight experienced more than typical 0.6 Hz frequency content in the SRB tilt actuators with moderate content in the rock actuators. Figure 3-29 illustrates this point with the results of the SRB left tilt actuator frequency response as compared to previous *Columbia* flight history.

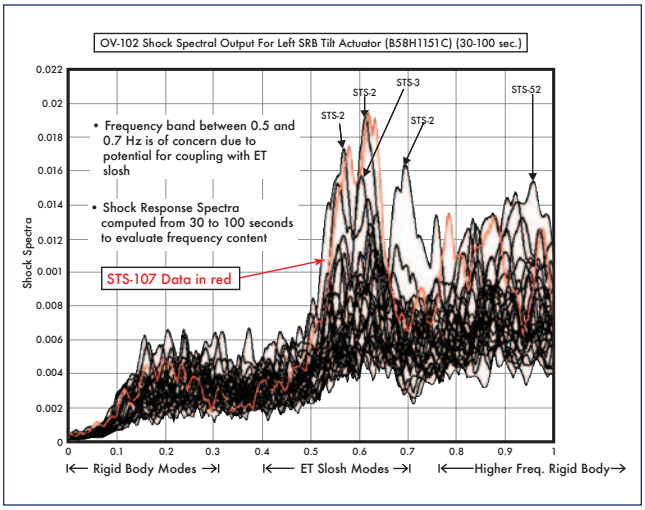

Figure 3-29. STS-107 SRB tilt actuators experienced more than typical 0.6 Hz content.

Figure 3-30 shows the relative time variation of amplitudes of the 0.6 Hz frequency content in wind and actuator data. The close correlation between the peaks in the 0.6 Hz content of the right and left actuator responses and the wind dynamics indicates that the actuators were responding primarily to wind rather than ET LOX slosh at this frequency through most of first stage (prior to SRB separation). As the 0.6 Hz content of the wind dynamics reduces in magnitude late in first stage, the remaining 0.6 Hz content in the actuator response may be attributed to a combination of the remaining wind dynamics and low-amplitude ET LOX slosh. STS-90 shows a similar wind frequency content.

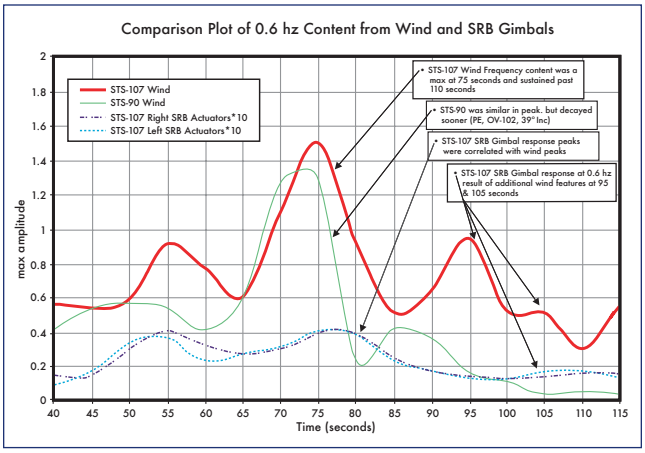

Figure 3-30. STS-107 SRB gimbal responses at 0.6 Hz frequency correlated to wind.

In general, ET LOX slosh is due to (1) commanded vehicle attitude transients, (2) additional wind dynamics after the start of ET LOX slosh, and (3) the 0.2 Hz rigid body vehicle mode. Note that a 0.6 Hz mode is the 3rd harmonic of the 0.2 Hz frequency, and is therefore subject to cross-coupling, and that some wind conditions can naturally contain a 0.6 Hz content.

The data from the ET LOX slosh study indicate that the flight control system operated as designed, and that more than adequate slosh phase stability margin existed. When the ET LOX slosh data is combined with the integrated vehicle loads analysis results (reference Figure 3-25), data indicate that the ET LOX slosh did not result in excessive vehicle loads at the orbiter/ET interface.

3.5.4 Nozzle Positions

A review of the STS-107 ascent data identified two discrete points in time when the SRB and SSME nozzle positions exceeded the flight experience envelope for those respective times in the ascent profile. The first event occurred when the center and right SSME yaw deflections exceeded the previous flight experience envelope during the period of maximum dynamic pressure, as a result of the differences between predicted and actual flight wind conditions (as shown in Figure 3-31 and Figure 3-32).

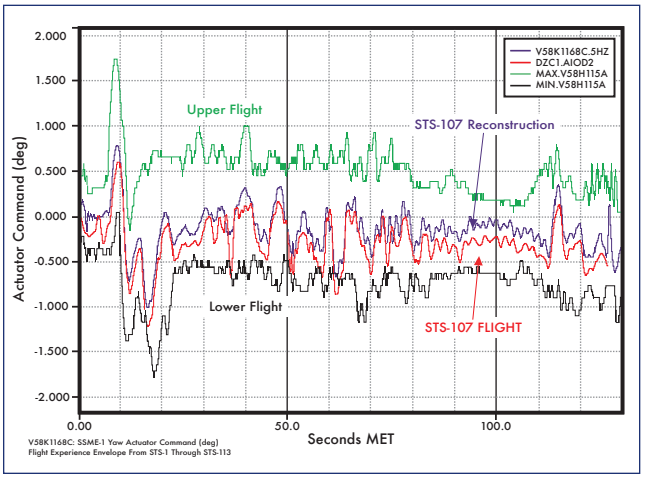

Figure 3-31. Center SSME yaw position.

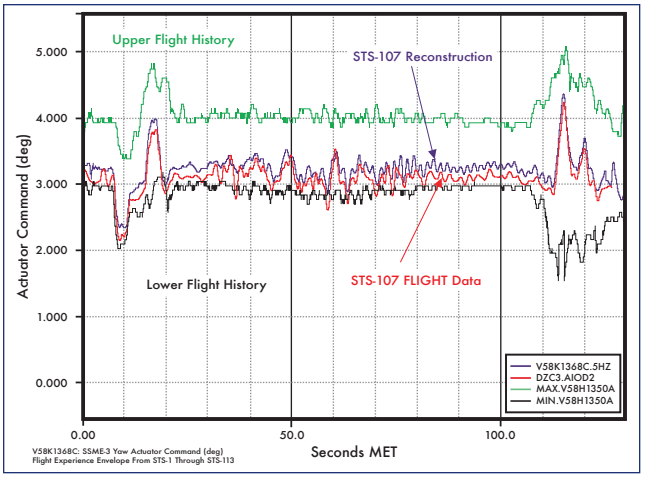

Figure 3-32. Right SSME yaw position.

This nozzle yaw event was coincident with a wind-induced positive lateral acceleration, as sensed via the body mounted accelerometer assemblies and a positive orbiter body yaw rate, as sensed by the orbiter rate gyro assemblies. The yaw event follows the period of greatest change in out-of-plane wind velocity (e.g., the wind shear previously shown in Figure 3-21).

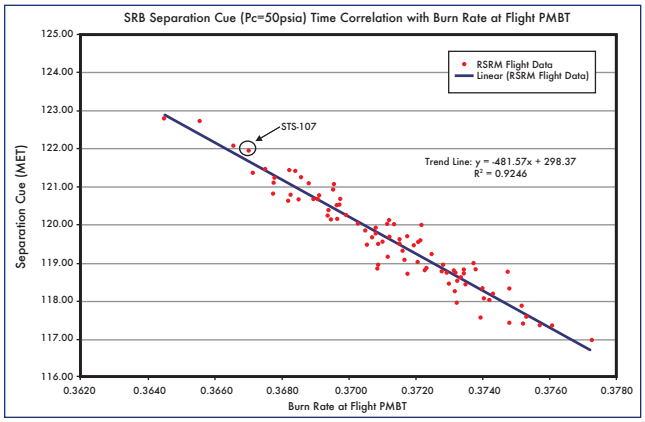

Figure 3-33. RSRM burn rate at propellant mean bulk temperature (PMBT).

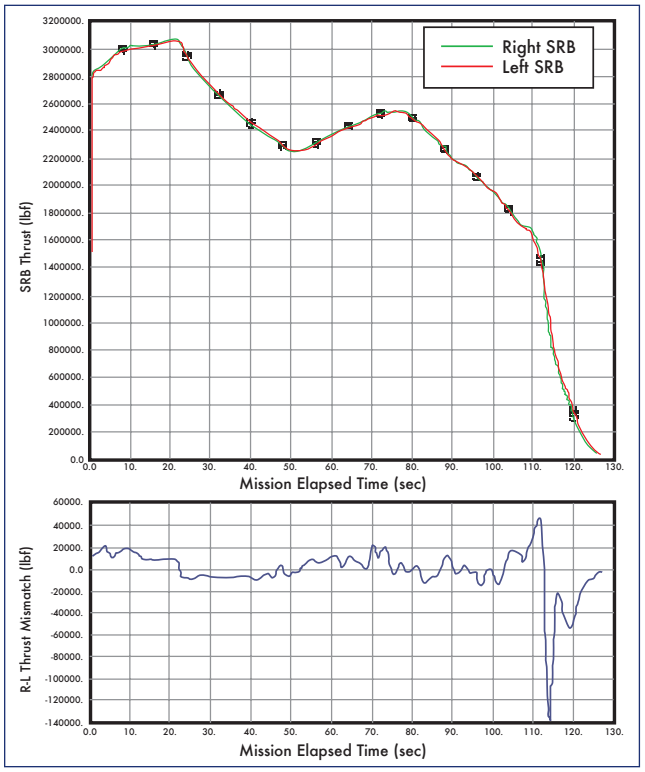

Figure 3-34. SRB thrust mismatch.

The large offset in the Center and Right SSME yaw positions at 62 seconds MET was the reaction of the flight control system to the wind shear event and day-of-launch wind differences as compared to the DOLILU design. The nozzle motion was within the capability of the Shuttle flight control system, and the system operated as designed. As discussed in Section 3.5.1, the reconstruction loads analyses indicate that the ascent environment-induced loads alone did not cause the ET bipod foam loss.

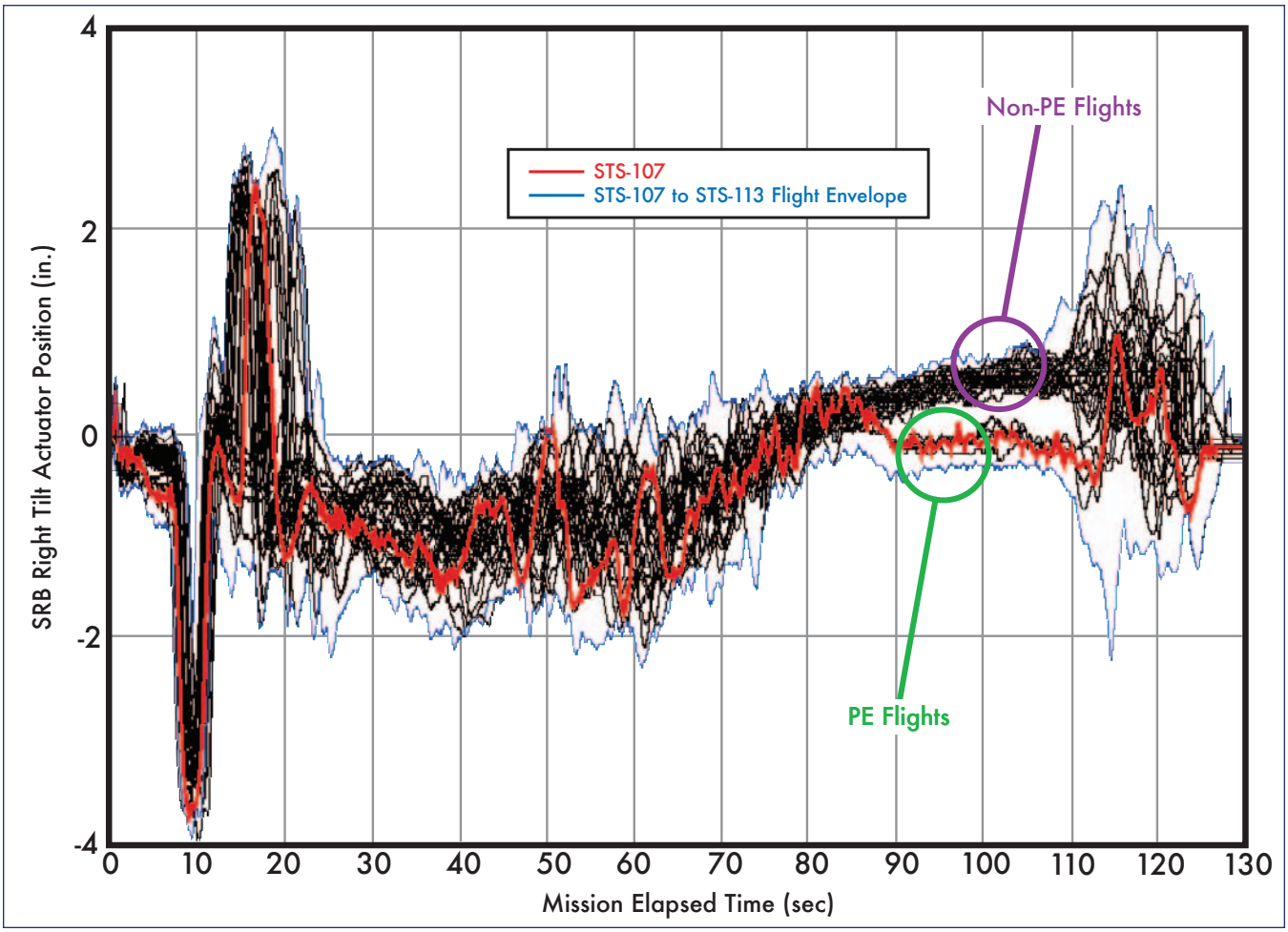

Figure 3-35. SRB nozzle position for PE flights versus non-PE flights.

The second nozzle motion event occurred when the SRB and SSME Thrust Vector Control (TVC) pitch and yaw deflections exceeded the previous flight experience envelope during SRB tail-off (as the SRB thrust diminished). The new flight experience envelope for the SSME and SRB nozzle positions was primarily due to (1) low Reusable Solid Rocket Motor (RSRM) performance that caused a time shift of the SRB tailoff events relative to previous flight experience, as indicated by a low burn rate shown in Figure 3-33, (2) a thrust mismatch between the left and right SRB caused by lower than normal thrust on the right SRB during tail-off, the final seconds of SRB burn (as shown in Figure 3-34), (3) a small bias in the left SRB pitch actuator that shifted the actuator positions farther toward the edge of the flight experience envelope, and (4) flight control trim characteristics unique to PE flights (as shown in Figure 3-35).

The RSRM burn rate is a temperature dependent function, and is determined based on pre-flight tests of small samples of the actual motor propellant at a reference temperature. These values are then adjusted based on a Predicted Mean Bulk Temperature (PMBT) based on the actual weather conditions prior to launch day. For STS-107, the pre-flight predicted motor performance was very close to that determined by post flight reconstruction. A low RSRM burn rate does not affect the total impulse produced by the RSRM during first stage; it only affects the amount of time the RSRMs must burn to achieve the same level of impulse.

The SRB thrust mismatch observed during tail-off was well within the design margin of the flight control system, and similar occurrences have happened numerous times during previous flights.

Due to flight control gain settings unique to PE flights, PE flights have a nozzle position closer to zero inches deflection from 85 to 110 seconds MET. The flight data that coincides with the STS-107 data are all from PE flights, seen clearly in the 85 to 110 seconds MET timeframe in Figure 3-35. The other grouping of flights in this same timeframe (85 to 110 seconds MET) are all non-PE flights and have larger pitch nozzle deflections.

To examine if SRB thrust mismatch during tail-off contributed to the loss of the ET bipod foam, several studies were conducted. The studies included data correlation of (1) flights that used LWT and PEs, and (2) flights that shed ET left bipod foam. The data correlation showed that for both families of flights, SRB thrust mismatches were observed on the majority of flights. The only flights to not have

significant SRB thrust mismatches near SRB tail-off were STS-87 and STS-90. The study of the two families of flights are summarized in Sections 3.5.6 and 3.5.7 of this report.

The data indicate that the SRB thrust mismatch on STS-107 was a direct result of SRB burn rate differences between the left and right SRB. The thrust mismatch observed on STS-107 and the new flight experience nozzle positioning occurred after the foam shedding event. The SRB thrust mismatch occurred on the majority of flights in both families of flights, including those that did not shed foam.

3.5.5 ET Separation Yaw Rate

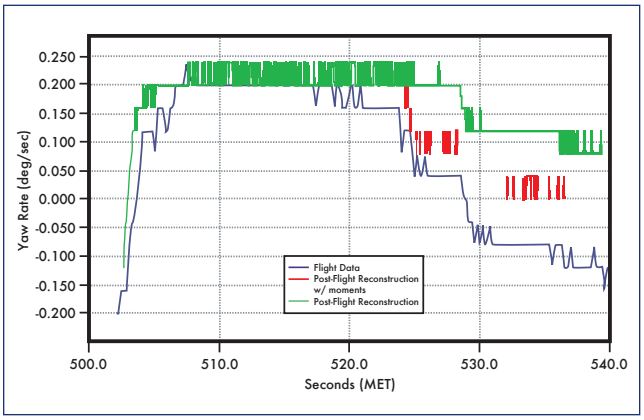

Figure 3-36. ET separation yaw rate.

A higher than typical negative yaw rate was observed at ET separation during STS-107. The yaw rate, shown in Figure 3-36, was approximately -0.12 deg/sec and near the edge of the flight experience envelope. The negative yaw rate is noteworthy because it does not correspond to the flight control system's thruster activity, known vent forces, or any other explained mission activity. Furthermore, the rate appears at the time of physical separation between the orbiter and external tank, which indicates that it is related to the structural release between the two objects. Although the negative yaw rate was unusual, it was well within the design and certification envelope for ET separation. This rate was also well within the flight limits (± 0.7 deg/sec) for ET separation to occur.

A fault tree analysis narrowed down the cause of the negative yaw rate to a release of strain energy at ET separation due to either (1) a misalignment of the orbiter and external tank at structural mating, or (2) a build up of strain energy in the ET structure and associated orbiter attachment strut areas due to thermal differences. STS-107 was one of six flights to have a negative yaw rate at ET separation. The other flights with negative yaw rates at ET separation were STS-2, STS-70, STS-80, STS-92, and STS-98. None of these flights are known to have had bipod foam loss. The ET separation yaw rate on STS-2 was identical to that on STS-107, within the 0.02 deg/sec accuracy limits of the sensors and related data and signal noise.

Data indicate that the yaw rate at ET separation did not result in re-contact between the orbiter and the ET after separation. This observation is based on high rate telemetry (25 Hertz) orbiter body rate data, and MADS accelerometer data analyzed post-flight. The yaw rate was within the expected range of vehicle body rates when taking into account all known error sources, including rate sensor noise. The data indicates that no correlation exists between observed yaw rate at ET separation and bipod ramp foam loss.

3.5.6 Data Correlation of Flights that Used a LWT and PEs

To determine if any of the items considered new flight experience were unique to the use of Light Weight Tank (LWT) and Performance Enhancements (PEs), an evaluation was performed to compare the STS-107 flight data to other flights using LWT and PEs. The STS-107 data was compared to flights STS-87, STS-89, STS-90, and STS-99 (as shown in Table 3-5).

LWT and PEs were also used on STS-85 and STS-86. Neither flight was included in the LWT and PE flight data correlation study because the flights were the first to use the new PE flight software, and as such had very few of the PEs active. One of the most significant PEs not active for STS-85 and STS-86 was the first stage pitch parallel change. Not having the first stage pitch parallel PE in place resulted in STS-85 and STS-86 being outliers when compared to the other five flights, due to significantly different SRB and SSME nozzle positioning during first stage (as previously shown in Figure 3-35).

The LWT and PE flight data correlation study compared the STS-87, STS-89, STS-90, STS-99, and STS-107 flight data for parameters that were considered new flight experience for STS-107. The LWT and PE flight data correlation included a comparison of environmental side-slip angle

Flight	*Tank type*	*ET #*	*Orbiter*	*Flight software*	*Inclination*	*Launch date*
STS-87	LWT	89	*Columbia*	OI-26A	28.45 deg	11/19/97
STS-89	LWT	90	*Endeavour*	OI-26A	51.6 deg	1/22/98
STS-90	LWT	91	*Columbia*	OI-26B	39.0 deg	4/17/98
STS-99	LWT	92	*Endeavor*	OI-27	57.0 deg	2/11/00
STS-107	LWT	93	*Columbia*	OI-29	39.0 deg	1/16/03

Table 3-5. LWT and PE flights.

during Hi-Q, SSME yaw position during Hi-Q, SRB thrust mismatch during Hi-Q, ET separation yaw rate during Hi-Q, and ET slosh.

The LWT and PE flight correlation study indicated that negative side-slip angles of -0.75 degrees or more occurred on all flights, including STS-90, which had the second largest side-slip angle of any flight in Hi-Q of -2.0 degrees. Evaluation of SSME yaw positions during Hi-Q indicated that only STS-90 had a similar signature. The STS-90 SSME yaw was primarily due to a large wind shear on that flight. Evaluation of SRB thrust mismatch shows a similar thrust mismatch and corresponding SRB and SSME TVC gimbal activity on STS-89 and STS-99 only. Within this family of flights, the negative yaw rate at ET separation and ET slosh characteristics were only observed on STS-107.

Of all of the flights studied, STS-90 and STS-107 were the most similar. Both flights were flown on *Columbia*, on a 39.0-degree inclination trajectory, used LWT and PEs, were daytime launches, and had a SPACEHAB module as the primary payload. Furthermore, STS-90 and STS-107 flew through a large wind shear during the Hi-Q region.

The data is inconclusive as to whether ascent GNC parameters/events correlated for flights using a combination of LWT and PEs.

3.5.7 Data Correlation of Flights with ET Bipod Foam Liberation

To examine if any of the items considered new flight experience for STS-107 contributed to the ET bipod foam liberation, a flight data correlation study was performed for all flights known to have lost ET bipod foam during ascent. The flights compared to STS-107 below included STS-7, STS-32, STS-50, STS-52, STS-62, and STS-112 (as summarized in Table 3-6). These are the only flights to have definitive photographic information to show ET bipod foam loss between liftoff and ET separation. An estimate of the ET bipod foam volume obtained from this photographic evaluation can also be found in Table 3-6. It should be noted that STS-32 is under review as a flight that lost ET bipod foam. It is known that STS-32 lost ET foam, but it is not clear at this time if it was acreage foam or bipod foam.

The ET bipod foam liberation flights were compared for parameters that were considered new flight experience for STS-107. The data correlation study included a comparison of environmental side-slip angle during Hi-Q, SSME yaw position during Hi-Q, SRB thrust mismatch during thrust tail-off, ET separation yaw rate, and ET slosh.

The negative side-slip angle of -1.5 degrees or more occurred on all flights in this family, and STS-62 had the

FLIGHT	*STS-7*	*STS-32*	*STS-50*	*STS-52*	*STS-62*	*STS-112*	*STS-107*
BIPOD FOAM LIBERATED ON ASCENT	YES	Under Review	YES	YES	YES	YES	YES
APPROX. DEBRIS VOLUME (cu. in.)	404	295	707	15	1	202	1200
ET NUMBER	06	32	50	55	62	115	93
ET TYPE	SWT	LWT	LWT	LWT	LWT	SLWT	LWT
ORBITER	*Challenger*	*Columbia*	*Columbia*	*Columbia*	*Columbia*	*Atlantis*	*Columbia*
INCLINATION (degrees)	28.45	28.45	28.45	28.45	39.0	51.6	39.0
LAUNCH DATE	06/18/83	01/09/90	06/25/92	10/22/92	03/04/94	10/07/02	01/16/03
LAUNCH TIME (local)	07:33:00 AM EDT	07:35:00 AM EST	12:12:23 PM EDT	1:09:39 PM EDT	08:53:00 AM EST	3:46:00 PM EDT	10:39:00 AM EDT
SIDE-SLIP ANGLE DURING FIRST STAGE	YES	YES	YES	YES	YES	YES	YES
NOZZLE YAW DURING FIRST STAGE	No	No	YES	YES	YES	No	YES
SRB THRUST MISMATCH	YES	YES	YES	YES	YES	YES	YES
ET SLOSH	No	YES	YES	YES	YES	No	YES
NEGATIVE YAW RATE AT ET SEPARATION	No	No	No	No	No	No	YES

Table 3-6. STS flights with ET left bipod foam liberation.

largest side-slip angle of any flight in first stage (prior to SRB separation) at -2.5 degrees. Evaluation of SSME yaw positions in first stage show similar signatures occurred on STS-50, STS-52, and STS-62 (all primarily due to large wind shears). Evaluation shows that similar thrust mismatch and corresponding SRB and SSME TVC gimbal activity occurred on all flights in this family. STS-107 is the only flight in this family to have a negative yaw rate at ET separation. The ET slosh characteristic was present on STS-32, STS-50, STS-52, STS-62, and STS-107.

In summary, the negative side-slip angle and SRB thrust mismatch were evident for all flights on which ET bipod foam loss was observed. For other parameters within this family of flights, no correlations are evident. It is noteworthy that five of the seven flights in the foam loss family were *Columbia* missions, all with the ET slosh characteristic. Finally, the data are inconclusive as to whether any of the new flight experience parameters (individually, or in some combination) by themselves caused bipod foam loss.

4.0 Orbit

4.1 Introduction

While *Columbia* was on-orbit, there was no indication of damage from either the ascent foam impact or a micrometeoroid/orbital debris (MMOD) hypervelocity debris impact based on orbiter telemetry, crew downlinked video and still photography, or crew reports. Multiple comprehensive postflight reviews of the same data indicated that there was nothing unusual with any of *Columbia*'s systems or structure. This included a detailed review of orbiter Inertial Measurement Unit (IMU) accelerometer, body rates, and jet firing data to determine if there were indications of an orbital debris hypervelocity impact. The results of this analysis show that there were no indications of an orbital debris impact, although there are several unexplained events. Data from an additional accelerometer package, known as Space Acceleration Measurement System (SAMS), was used to determine if this more sensitive system was able to detect any unusual activity during these timeframes. Details of the orbital debris analysis can be found in Section 4.2 and the flight day 2 debris event will be discussed in Section 4.3.

4.2 Orbital Debris

4.2.1 Orbital Debris Risk Assessment

There were multiple payload constraints on this mission, which resulted in 239 attitude maneuvers, or orientation changes. For each Shuttle mission the complement of attitude maneuvers is analyzed for orbital debris risk of a critical penetration due to an on orbit hypervelocity impact. This same analysis, performed post-flight, determined that the probability of no critical penetration was 0.9972, which is well below the guideline for critical penetrations. The analysis also included specifics for critical penetrations of the left wing. The results show that the overall probability for no critical penetration is 0.9996 for the entire left wing and 0.9999 for the left wing leading edge RCC.

4.2.2 Micrometeoroid or Orbital Debris Detection

Postflight, a NASA JSC team consisting of members from Mission Operations, Engineering, and Space and Life Sciences with the support of Draper Labs, participated in an effort to use downlisted data to identify any external forces or torques that could be correlated with an MMOD impact. This task was divided into four different areas:

1. Build an inclusive, detailed activity timeline that includes all known Shuttle and payload events (venting, waste control system activities, LiOH canister change out, payload bay door operations, and SPACEHAB systems operations) that would cause attitude and rate errors or momentum changes detectable by the orbiter systems.
2. Review the orbiter IMU rate data for net changes in angular momentum, which would be indicative of an MMOD strike.
3. Screen the 20,000 plus orbiter Vernier Reaction Control System (VRCS) jet firings with an algorithm to determine whether or not each firing was due to the control system response to normal attitude changes or disturbances, or in response to an MMOD strike.
4. Examine SAMS payload experiment data for potential signs of an MMOD strike.

4.2.2.1 IMU Rate Data Review

This study reviewed all orbiter data from various sensors and systems. The only data useful for this study were the orbiter body axis rate data, which are derived from IMU attitude data by the Guidance Navigation and Control (GNC) flight software. This analysis assumed rigid body dynamics; flexural response was covered in the SAMS data analysis (see below).

The entire orbit portion of the mission, from the orbit transition (1 hour MET) to four hours prior to the deorbit, was examined. A total of 238 events of interest were identified which required further examination. All but 13 of these events were correlated to either a known forcing function, or the signature did not match the expected dynamic response of an externally applied impulse (MMOD strike). The remaining 13 unexplained events were analyzed in significantly greater detail.

Additional analysis included the evaluation of the rate transients and a time integration of the change in angular momentum across the event of interest. The guiding principle of this analysis is that unless there is an external force or torque applied to the vehicle, conservation of angular momentum will always apply. This study resulted in the elimination of 10 of the 13 events that did not fit the expected response for an externally applied impulse. One event was inconclusive due to the low resolution of the data, and the remaining two events have the potential to be caused by an MMOD strike; however, other causes are also possible (unknown venting, etc.). The orbiter rate data cannot be used to explicitly determine mass, velocity, or point of impact of an MMOD object. Table 4-1 provides an overview of the original 13 events of interest.

Event	EST* (Day/hour:min:sec)	MET* (Day/hour:min:sec)	External torque, unknown venting, or potential MMOD** strike	Angular momentum conserved (crew motion, other, or unknown)	H_2O dump	Inconclusive
1	18/11:45:00	2/01:06:00		X		
2	19/12:45:50	3/02:06:50		X		
3	19/20:02:20	3/09:23:20	X			
4	19/21:31:30	3/10:52:30		X		
5	24/16:45:10	8/06:06:10			X	
6	25/04:19:20	8/17:40:20	X (possible)			
7	25/05:08:00	8/18:29:00		X		
8	26/03:53:20	9/17:14:20		X		
9	29/00:02:00	12/13:23:00		X		
10	29/15:48:30	13/05:09:30		X		
11	29/17:40:10	13/07:01:10		X		
12	31/11:07:00	15/00:28:00				X
13	32/02:02:30	15/15:23:30		X		

** Times are approximate*
*** Micrometeorite or orbital debris*

Table 4-1. Summary of analysis of 13 rate events.

4.2.2.2 Lower Bound of IMU MMOD Detection Threshold

Two separate techniques were evaluated to attempt to bound the lowest MMOD mass and velocity that could be detected using the orbiter IMU data. The first used measured angular rate data, while the second used the accelerometers to measure a change in velocity.

There were two assumptions for this angular rate analysis. First, the lowest value of angular rate change that can be detected by the Shuttle IMU's is 0.002 deg/sec, based on an evaluation of body rates and engineering judgment. Second, to bound the minimum mass of an MMOD object, the efficiency of transfer of linear momentum of the striking object was assumed to be 100% with optimal geometry. The resulting transfer of the linear momentum is a change of orbiter angular momentum.

The bounding of the lower limit of the linear momentum and/or mass of a potential strike object is not a one-dimensional exercise. Several assumptions must be made to perform this analysis. Strike location on the orbiter is significant. For a fixed orbiter rate change from a strike, the radius from the orbiter center of gravity (CG) to the strike location is inversely proportional to the linear momentum of the striking object. Also, once the linear momentum of the striking object is defined, the mass of the object is inversely proportional to the velocity. The examples shown in Table 4-2 are three of many possible solutions; however, they have

Body Axis	Body Rate (degrees per second)	Angular Momentum (slug*ft²/sec)	Assumed Strike Location of MMOD	Assumed Velocity of MMOD (nmi/sec)	Lower Bound of the Mass of MMOD (Assumes optimal geometry & 100% momentum transfer) (gram)
Roll	0.002	36	Outside edge of the main landing gear door, or about 14 ft Y c.g. offset.	5	1
Pitch	0.002	273	The forward most portion of the wing structure, or about 23 ft in front of the X c.g.	5	6
Yaw	0.002	285	The forward most portion of the wing structure, or about 23 ft in front of the X c.g.	5	6

Table 4-2. Summary of analysis of the lower bound of MMOD (based on body rate data).

been selected to be representative of a strike location roughly associated with the main landing gear door and forward through the leading edge of the wing.

The lowest value of velocity change that can be detected is 0.0344 feet per second based on the minimum integrated acceleration (velocity) pulse size from the IMU's. In order to determine the minimum possible detectable MMOD mass for this orbiter velocity detection capability, the following assumptions were used: conservation of linear momentum, a 100% momentum transfer from the striking object, object impact at the orbiter center of mass, and a relative debris velocity of 5 nmi/sec. Based on these assumptions, the lowest detectable MMOD mass is 127 grams. From this momentum analysis, it is apparent that the orbiter being struck by an approximately one-quarter pound object (at 5 mi/sec) assuming 100% momentum transfer would most likely be noticeable by the crew. Therefore, IMU accelerometers are not considered of significant value in the search for an MMOD strike on-orbit.

4.2.2.3 Vernier Thruster Firing Algorithm

The review of orbiter data accounted for momentum changes due to VRCS jet firings. However, the possibility existed that a debris strike with enough energy or striking the orbiter at the right time could have caused the On-Orbit Digital Auto-Pilot (DAP) to command a jet firing due to a rate deadband exceedance.

The On-Orbit DAP will command jets to fire to maintain attitude errors within attitude deadbands and rate errors within rate deadbands. During periods of attitude hold, the majority of jet firings are due to the attitude deadband. Rate deadband firings typically occur at the beginning and end of attitude maneuvers, and during maneuvers due to changes in the desired rate. Figure 4-1 depicts changes in the vehicle rates due to jet firings and normal gravity gradient forces.

Analysis was undertaken to examine every jet firing and determine the cause of the firing. An algorithm was built to screen all nominal attitude deadband related firings. The remaining firings were examined to determine cause.

The algorithm assumed a VRCS jet was firing any time the downlist (telemetry) indicated a command to fire any one or more of the six VRCS jets. Also, instances of VRCS firings when the DAP attitude error (downlisted at 1 Hz) was less than 95% of the estimated attitude deadband were flagged for further investigation.

A total of 747 jet firings out of 28,779 were identified by the screening process for further investigation. Of these, 19 were due to faulty driver indications (data hits). These were verified via no change in slope of attitude rates, DAP attitude errors, and the six vernier jet fuel and oxidizer injector temperatures.

The remainder were examined and determined to be caused by (1) rate limit firings at the start and stop of attitude maneuvers, (2) rate limit firings that occurred during maneuvers due to changes in the desired rate, and (3) attitude deadband

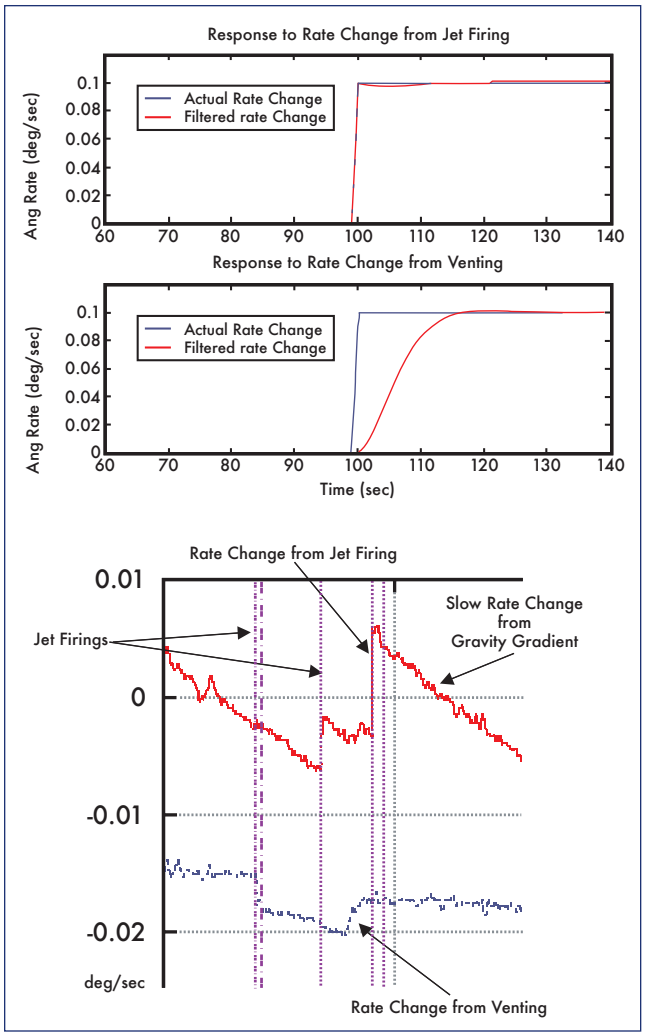

Figure 4-1. Jet firing example for vehicle rates

firings not screened. The final result was that there were no unexplainable jet firings in the STS-107 on-orbit data.

4.2.2.4 SAMS Data Analysis

After a review of the available payload sensors, it was determined that the SAMS data package would be the only suitable sensor that could provide additional data to aid in the detection of an MMOD strike. SAMS provides tri-axial accelerometers to measure the vibratory and transient portion of the microgravity environment. Those vibratory and transient accelerations are composed of disturbances that originate in STS equipment, scientific experiment, and crew operations. The vibratory/transient accelerations are on the order of milli-g's and are sampled at 100 Hz. While the Shuttle IMU's are designed to measure the rigid body accelerations and attitude, SAMS measures the vibratory/transient portion of the micro-gravity environment. The vibratory portion is the dominant part of the SAMS data. Three SAMS sensor sets were aboard STS-107; however, only one had data that was downlinked during the flight. This sensor was located in the SPACEHAB Module near the Combustion Module 2 experiment.

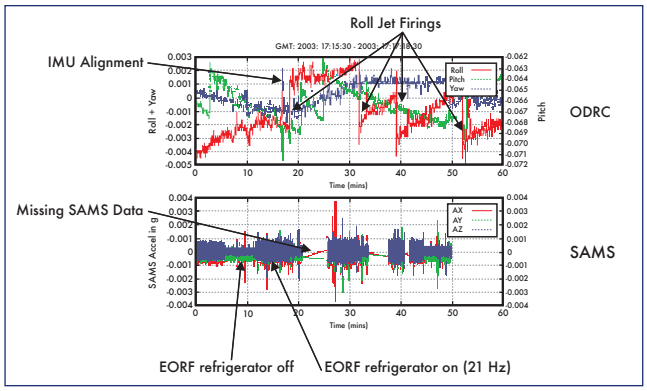

Figure 4-2. Sample data from SAMS and ODRC.

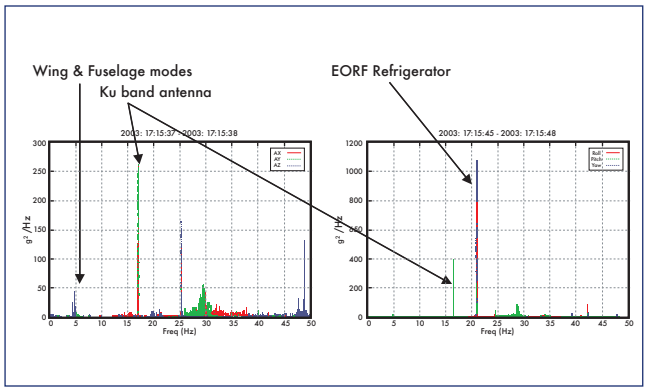

Figure 4-3. SAMS data frequency content.

SAMS data was used to support the aforementioned IMU rate data review. Anomalies in rates from manual review of orbiter body rates were compared to SAMS measurements to help identify sources. Figure 4-2 provides a sample plot of SAMS data and the response signature to an IMU alignment and the Enhanced Orbiter Refrigerator/Freezer (EORF) operation, as well as downlisted telemetry in the Operational Data Retrieval Complex (ODRC) system. SAMS data was also scanned for large transients to identify potential strikes (the assumption is that a hypervelocity impact would "ring" the structure). Various frequencies from nonstructural items were identified, so that they could be filtered out of the data. Figure 4-3 shows the frequency response of several items such as the EORF refrigerator and the Ku-band antenna. A detailed structural model that identifies frequencies of primary structure was developed. This model was used to screen for vibrational transients associated with orbiter wing strikes.

The review of SAMS data has not uncovered any events that could be correlated to a hypervelocity debris strike from micrometeoroids or orbital debris.

4.3 Flight Day 2 Event

4.3.1 Radar Tracking of Flight Day 2 Object

Air Force Space Command post-flight evaluation of radar tracking data indicated an object in the vicinity of the orbiter on flight day 2. The object remained on-orbit for approximately two and a half days, and reentered the atmosphere. Multiple government agencies participated in complex post-mission analysis of this object. These agencies include the Department of Defense *Columbia* Investigation Support Team, United States Strategic Command, Air Force Research Labs (AFRL) at Wright-Patterson Air Force Base, Air Force Space Command (AFSPC), Lincoln Laboratory at the Massachusetts Institute of Technology, and NASA's Johnson and Kennedy Space Centers.

The AFSPC Space Analysis Center estimated the departure time for the object was January 17, between 10:00 and 11:15 EST. Because there was no direct radar observation at the exact time of departure from the orbiter, analysis indicated that the most likely window of departure was between 10:30 EST and 11:00 EST. The analysis was complicated by the high drag profile, making it difficult to determine the precise time when the object left the vicinity of the orbiter.

The calculated departure velocity was relatively low and was estimated to be 0.7 to 3.4 miles per hour with the lower velocity being more likely. An exact departure direction relative to the orbiter could not be determined. Multiple ground sensors including Eglin Air Force Base (AFB), Beale AFB, Cape Cod Air Force Station (AFS), and the Navy Space Surveillance fence radar tracked the object. The object reentered the atmosphere on January 19 between 20:45 EST and 23:45 EST. Figure 4-4 depicts the tracking of the object including various sensor passes.

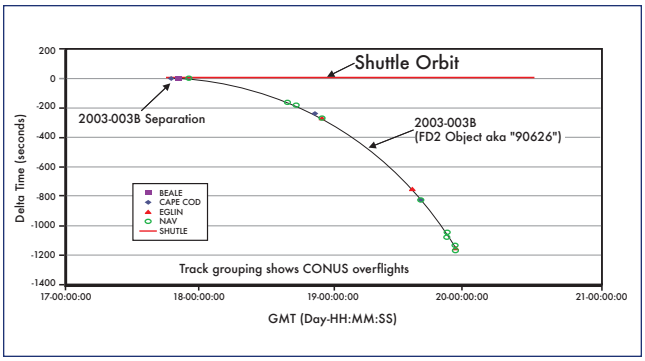

Figure 4-4. Tracking of flight day 2 object through various sensor passes.

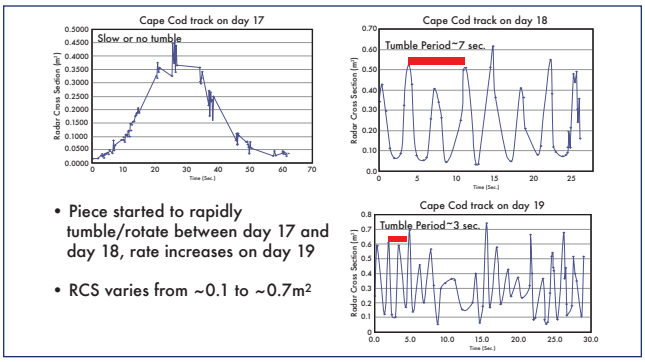

Figure 4-5. On-orbit RCS shows increased tumble/rotation rate over time.

Date/Time (EST hh:mm)	EVENT
January 17 9:42 to 9:46	Attitude maneuver to a biased tail forward bay to earth attitude (biased -ZLV, -XVV)
January 17 10:17 to 10:21	Maneuver back to the bay to earth tail forward attitude (ZLV, -XVV)
January 17 10:30 to 11:00	Best estimate of object departure window
January 17 11:25	Manual fuel cell purge
January 19 16:39	First water dump
January 19 20:45 to 23:45	Object re-enters atmosphere

Table 4-3. Chronology of events related to flight day 2 object.

Based on the observed radar cross sections, the object appeared initially to have a minimal to no tumble/rotation rate, but it gradually developed a rate over the next two days. During a Cape Cod AFS sensor pass on January 18 at 15:29 EST, the tumble/rotation rate had a period of seven seconds. Later, on January 19 at 10:39 EST during another Cape Cod AFS pass, the apparent tumble/rotation rate had increased and the period was approximately three seconds. Figure 4-5 depicts the tumble/rotation rates during the timeframe that the object remained in orbit. The exact physical size and mass of the object are unknown, although it appeared to be a lightweight piece based on the observed ballistic coefficient.

4.3.2 Analysis of Mechanisms for Object Release

The timeframe of estimated departure has been reviewed in detail. There were no unusual crew events, telemetry data, or accelerations in orbiter or payload accelerometer data that can account for the ejection of an object matching this description. SAMS, IMU, and jet firing data indicate that there was no orbital debris impact during the timeframe. Additional reviews indicate that no external mechanical systems such as the radiators or FREESTAR experiment canister doors were active during the time of interest. The port radiator was deployed on January 16 at 13:47 EST and was stowed on January 19 at 17:39 EST.

Crew commentary in the air-to-ground voice transmission during this window was routine and there was no mention of an object being observed. There was no video downlink at the time of interest, but subsequent surveys of downlinked video and still imagery did not reveal any items missing from the payload bay or visible exterior of the vehicle.

The orbiter did not perform any translational maneuvers during this timeframe. Two attitude maneuvers or orientation

MET (hh:mm:ss)	EST (hh:mm:ss)	EVENT
0:00:00	10:39:00	*Columbia* launch
0:01:21.7	10:40:21.7	Foam departs ET left bipod ramp
0:01:21.9	10:40:21.9	Foam impacts Orbiter left wing RCC panels 6 through 8
0:02:06.6	10:41:06.6	SRB separation
0:07:23.6	10:46:23.6	3-G throttling of Space Shuttle Main Engines
0:08:22.5	10:47:22.5	Main Engine cutoff command
0:08:33	10:47:33	Zero thrust
0:08:43.7	10:47:43.7	ET separation translation
0:08:57	10:47:57	Crew +X translation for ET photography
0:10:24 – 0:12:24	10:49:24 – 10:51:24	Main Propulsion System dump
0:13:44 – 0:14:33	10:52:44 – 10:53:33	Manual pitch maneuver for ET photography
0:29:52 – 0:34:24	11:08:52 – 11:13:24	Attitude maneuver to Orbital Maneuvering System (OMS)-2 burn attitude
0:41:24 – 0:43:24	11:20:24 – 11:22:24	OMS-2 burn using left and right OMS engines
~01:15:00	11:54:00	Attitude maneuver to payload bay door opening
~0:02:00	12:39	Configure for vernier attitude control (six small, 24 lb thrusters)

Table 4-4. Summary of nominal launch day events.

changes were accomplished using the small, 24 lb vernier attitude control thrusters. The first maneuver was a 48-degree yaw maneuver to a biased tail forward bay-to-earth attitude that occurred from 09:42 to 09:46 EST. Near the window of estimated departure, there was a maneuver back to the bay-to-earth tail forward attitude from 10:17 to 10:21 EST.

A manual fuel cell purge was performed later at 11:25 EST, outside the window of probable object departure. The first orbiter water dump occurred approximately two days after this event. Table 4-3 lists the chronology of relevant events.

Data indicate that in the timeframe of the object departure there were no unusual forces or mechanisms for liberating the debris that were not also present prior to this timeframe. The orbiter had encountered a more severe loading environment during the ascent and post-insertion timeframe than on-orbit as depicted in Table 4-4. The orbiter was using the large 870 lb primary reaction control system thrusters for attitude maneuvers until the small 24 lb vernier thrusters were activated about two hours after launch. One theory is that 16 orbits of thermal cycling (day/night transitions) caused stored energy from an object in the payload bay or on the orbiter structure to be released. Another theory is that attitude maneuvers in this timeframe could have assisted the object in obtaining the opening rate from the orbiter. The data is inconclusive in determining the cause of the object departing on flight day 2.

4.3.3 Radar Cross Section and Ballistics Testing

In addition to the careful inspection of downlinked orbiter payload bay video and still photography, radar testing and ballistics analysis of various thermal protection system items and thermal blankets have been conducted in an attempt to identify the flight day 2 object. The AFRL Advanced Compact Range Facility at Wright-Patterson AFB in Ohio tested a total of 32 items for radar cross section (RCS) at the Ultra-High Frequency (UHF) frequency of 433 MHz. These items comprise nearly the entire external surface of the orbiter as well as the exposed surfaces in the cargo bay, RCC panels, and carrier panels. The items tested also included four pieces of recovered RCC debris from *Columbia* to better understand the radar characteristics of partial Tee seals and RCC panels.

The results of this radar testing and ballistics analysis have excluded all external Shuttle materials with the exception of 1) a whole Tee seal, 2) a Tee seal fragment that includes an attachment flange and/or apex segment, or 3) RCC panel acreage no less than 90 square inches and roughly square in shape (+/- 20%), although curvature is possible, with a thickness on the order of 0.33 inches. An RCC panel segment matches the RCS and ballistic performance characteristics observed during the STS-107 mission.

A Tee seal fragment with an apex segment matched the RCS characteristics extremely well in any spin orientation; however, the ballistic match required a very specific spin orientation that was shown to be feasible in one analytical simulation. Therefore, it is possible that the flight day 2 object was either a partial Tee seal or RCC panel acreage piece. The Incoflex spanner beam "ear muff" insulation was also a good match for both ballistics and RCS. Because the "ear muff" is situated behind the RCC panel, it is excluded from being considered a very likely candidate because of the lack of a mechanism for exposing it to the space environment. If the damage to the wing were actually a 10-inch diameter, uniformly round hole, then an "ear muff" would be a more plausible candidate. However, it is considered unlikely that the wing damage was a 10-inch diameter round hole. The damage is considered to be the equivalent of that which would provide the same thermal response during entry as a 10-inch diameter hole did in the analyses and simulation. It is not likely that the actual wing damage was geometrically uniform. The damage was more likely a combination of cracks and holes, or a slot, such as a Tee seal or partial Tee seal missing or displaced. Therefore, the ear muff is not considered to be a good candidate for the flight day 2 object. Figure 4-6 shows the three leading edge

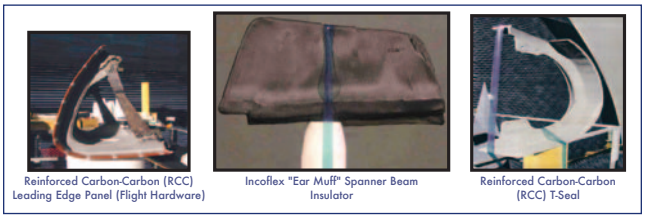

Figure 4-6. Leading edge structural subsystem components matching RCS and ballistics.

Processing Flow	*Tool Description*	*Location*	*PR #*
OMM J3	Allen Socket, 2"x 1/2"	Mid-body	(LAF-2-J3-0550)
OMM J3	Plastic Extraction Tool, 22 gauge	Flight Deck	(LAF-2-J3-0567)
OMM J3	Pliers, 7 3/4"	Hypergolic Maintenance Facility (HMF)	(LAF-RPO5-15-0004)
OMM J3	Screwdriver, 11"	HMF	(LAF-RPO5-15-0005)
OMM J3	Screwdriver, 7"	HMF	(LAF-RPO5-15-0006)
OMM J3	Screwdriver, 8"	HMF	(LAF-RPO5-15-0007)
STS-109	Mini Flashlight, 6"	Forward Reaction Control System (FRCS) 2	(LAF-FRC2-27-0005)
STS-107	Socket, 7/16"x 5/16"	Aft Compartment	(LAF-2-28-0632)

Table 4-5. Lost tools in Columbia *processing for STS-107, STS-109, and OMM J3.*

components that match both RCS and ballistics analysis. It should be noted that a full Tee seal and RCC panel are shown in these photos while there are specific partial Tee seal and RCC panel configurations that match the test results.

4.3.4 KSC Lost and Found Items

A review was conducted of the lost-and-found items from the *Columbia* processing flows of STS-107, STS-109, and the last *Columbia* OMM-J3. The largest tools that were lost and not found are listed in Table 4-5; other smaller items (e.g., washers and nutplates) are not listed. The item, size, location, and Problem Report (PR) number are noted. The largest item documented on a Lost and Found (LAF) PR is a piece of a blanket 6" x 3" lost in the payload bay (LAF-2-27-0611) during STS-109 processing. These items were screened using the ballistic coefficient and RCS criteria. All of the items failed the RCS screening and their RCS is too low to be a candidate for the flight day 2 object.

4.4 Orbit Summary

Extensive data review provided no conclusive indication of damage from either the ascent foam impact or an MMOD hypervelocity impact based on orbiter telemetry, crew downlinked video and still photography, or crew reports.

Orbiter IMU and jet firing data have been reviewed, and this review confirmed that the IMU's were not designed for MMOD detection and data available to detect an MMOD strike is coarse. This data review found 13 events that required additional analysis. After this additional analysis, only two events remained that could not be ruled out as MMOD strikes. An examination of all VRCS jet firings was conducted and showed no unexplainable jet firings during STS-107.

SAMS data were also used in the analysis of the 13 events detected using IMU rate data. SAMS sensor data were also screened for large transients indicative of an MMOD strike; however, none were found. A model was developed that identifies the modal frequencies of the Shuttle structure (including wing modes) to further screen the SAMS data for MMOD strikes.

A review of the flight day 2 event has been performed including RCS testing and ballistics analysis of 41 items, including TPS. The analysis performed to date indicates that a full Tee seal, a partial Tee seal, and RCC panel are the only tested items that have not been excluded.

It is possible that another untested object could match the RCS and ballistics and have departed the orbiter on flight day 2. Objects have departed the payload bay on previous Shuttle missions. The data are inconclusive as to whether the ET ascent foam debris event and the flight day 2 event are related.

5.0 Deorbit/Entry

5.1 Introduction

The deorbit and entry section is divided into four distinct areas. The first section discusses the upper atmosphere weather including high altitude winds, and the Kennedy Space Center (KSC) Shuttle Landing Facility (SLF) weather for the STS-107 landing. The next section includes a detailed discussion of forensics data obtained from testing and analysis of the key items in the recovered debris. The third section is a narrative of the entry events from February 1, 2003, and the fourth section is a brief discussion of key elements of the aerodynamic reconstruction.

5.2 Weather

5.2.1 Upper Atmosphere Weather

As the Shuttle entered the atmosphere, it descended from about 400,000 feet when located over the central Pacific Ocean to roughly 200,000 feet over Texas. The Goddard Space Flight Center Data Assimilation Office (DAO) provided the GEOS-4 model analysis for the investigation in order to provide a best estimate of the density, temperature, and wind along the entry trajectory. The GEOS-4 model assimilates a wide variety of data sources to produce an integrated 3-dimensional analysis of the atmosphere from the Earth's surface to about 250,000 feet. The Global Reference Atmosphere Model (GRAM) was used to provide information about the atmosphere from Entry Interface to the top of the GEOS-4 analysis. In general, the entry environment was characterized by a lower than average density and higher than average winds prior to the vehicle breakup. Comparison of the GEOS-4 analysis to GRAM indicates that the estimated density and winds were within the expected climatology for the upper atmosphere. Figure 5-1 shows the wind profile that was developed by the DAO as part of the STS-107 investigation.

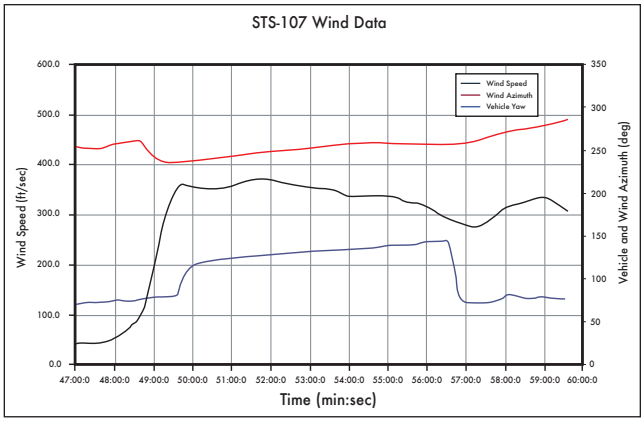

Figure 5-1. Wind profile developed by DAO as part of the STS-107 investigation (time referenced to 8:min:sec EST).

5.2.2 Landing Weather

On the morning of February 1, 2003, there was a concern for ground fog formation at KSC for the first STS-107 landing opportunity. This concern is not uncommon for a morning landing at KSC during the winter months. The landing time for the first KSC opportunity was 9:16 EST. The forecast called for the fog to burn off as the sun rose, producing mixing in the lower levels of the atmosphere. The Shuttle

Training Aircraft (STA), which is used for weather reconnaissance, flew approaches to both the KSC-15 and KSC-33 runways to determine the best runway for landing. The STA is used to evaluate touchdown conditions, visibility, turbulence, crosswind, and overall pilot workload. At the time of deorbit decision, runway visibility was reported as 4 miles in light fog with winds 5 knots from the west. Visibility on final approach was slightly better for Runway 33. The final landing runway decision was not made at that time.

Leading up to the deorbit decision time, the fog had been the main point of discussion until some clouds developed to the northwest of the landing area. Satellite imagery indicated an area of broken clouds (5/8 to 7/8 sky coverage) with bases at approximately 4,000 feet above ground level between 20 and 25 nautical miles northwest of the runway. The forecast was for those clouds to erode as they approached the SLF producing scattered clouds (3/8 or 4/8 sky coverage) at landing time. The Spaceflight Meteorology Group (SMG) stated that if erosion did not occur, the clouds reaching the SLF would be covering the runway for the first landing opportunity. No low clouds were being reported at the SLF at deorbit burn decision time and no surrounding observing sites were reporting low ceilings. The final forecast update was for a few clouds at one thousand feet and scattered clouds at three thousand feet, and the forecast remained "Go" per the flight rules.

At the actual deorbit decision time and at the actual deorbit time, the landing weather satisfied all criteria per the documented Flight Rules, resulting in a "Go" observation and a "Go" forecast. At 9:10 EST, approximately five minutes prior to the expected landing time, the weather observation at the SLF reported a broken ceiling at 3,500 feet with 6/8 sky coverage and visibility 7 miles. The ceiling remained 3,500 broken until 9:25 EST at which time the SLF observer reported scattered clouds with 3/8 sky coverage.

The cloud deck at landing time was below the Flight Rule ceiling minimum requirement of 8,000 feet. Therefore, the commander would have relied in part on computer instrumentation and visible geographic references of the airfield, flying a Microwave Scanning Beam Landing System (MSBLS) approach until breaking out of the clouds at 3,500 feet, a procedure regularly practiced in several landing simulators. The incorporation of MSBLS data provides very accurate onboard navigation, allowing for more accurate instrument information and facilitating instrument approach capability. The opinion among several experienced astronaut commanders, including the Chief of the Astronaut Office, is that the landing would likely not have been affected by this ceiling, when considering all other conditions of the day.

5.3 Hardware Forensics

As discussed earlier in Section 3, *Columbia* entered the upper atmosphere with unknown damage to a Reinforced Carbon-Carbon (RCC) panel or Tee seal in the left wing RCC panels 6 through 9 area. The panel 8/9 area is the most likely area of damage as determined by hardware forensics testing and analysis of MADS entry temperature and strain measurements on the left wing leading edge structure. This damage area is also consistent with the location of the ascent foam impact, and includes the Tee seals adjacent to panel 8, Tee seals 7 and 8.

The forensic data indicate that the panel 8/9 area was subjected to extreme entry heating over a long period of time leading to RCC rib erosion, severely slumped carrier panel tiles, and a substantial slag deposition on the upper portion of RCC panels 8 and 9. Figure 5-2 shows the slag deposition (both metallic and oxide) in the RCC panel 8/9 area relative to the other parts of the wing leading edge, and Figure 5-3 shows samples of the severe slag deposition on the panel 8 rib. A review of all recovered debris indicates that this is the most probable area of a breach into the wing since there are no other debris pieces that exhibit the unique characteristics observed in this area.

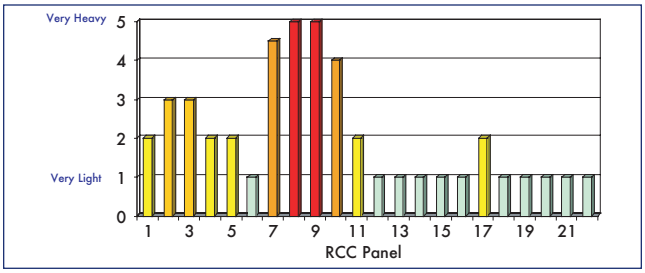

Figure 5-2. Slag deposition in the RCC panel 8/9 area relative to the other parts of the left wing leading edge.

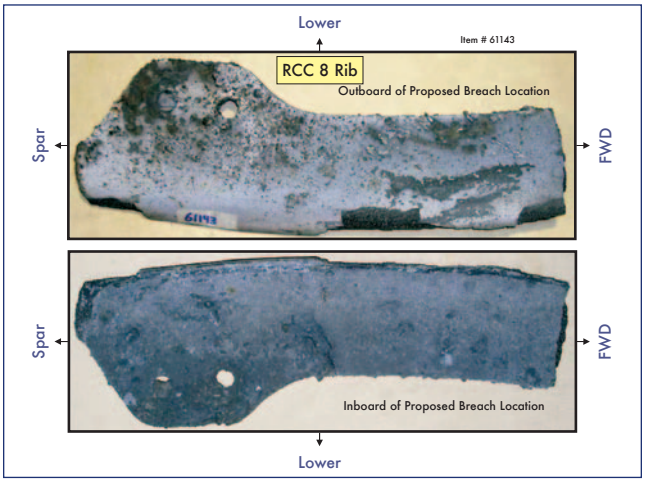

Figure 5-3. Samples of severe slag deposition on the panel 8 rib.

Based on the slag deposition on the upper RCC panel 8 and the rib erosion at the panel 8/9 interface, the most likely area of damage was the bottom portion of RCC panel 8. The outboard apex on the panel 8 upper inboard rib shows knife edge erosion, and the rib tapers from a design thickness of 0.365 inches to 0.05 inches. The surface of the panel 8 outboard rib and matching heel piece show a similar sign of erosion, as does the panel 9 upper inboard rib. The erosion on both the panel 8 and 9 rib is on the inboard side, indicating that flow is coming from the panel 8 location. Additionally, several lower carrier panel tiles in the RCC panel 9 area also show significant slumping and erosion that is consistent with a hole or breach in the lower part of RCC panel 8. Fig-

ure 5-4 and Figure 5-5 show an example of the rib erosion and the flow on the lower carrier panel 9.

Figure 5-6 is a CAD drawing of the recovered debris showing overall slag deposition and erosion patterns. The drawing is a view from behind the RCC panels since this provides the best view of the erosion and slag deposition. Three full Tee seals can be seen in this drawing; the leftmost, Tee seal 9, divides panel 9 and 10; Tee seal 8 in the center divides panel 8 and 9; the rightmost, Tee seal 7, is the division between panel 7 and 8. The drawing shows the heavy slag deposition of the upper portion of panel 8 indicating that the probable breach area was the bottom of panel 8. The severely eroded RCC ribs are also visible near the RCC panel 8/9 Tee seal. The heavy slag on these inner surfaces indicate flow from the panel 8 direction toward panel 9. This is also consistent with the knife-edge erosion shown in Figure 5-4. The proposed flow direction leading to the erosion and slag deposition on the lower carrier panel 9 tiles can be seen in this view as well. The detailed flow, erosion, and deposition are best viewed in Figure 5-5. The last significant feature in Figure 5-6 is the heavy slumping that is observed on the upper carrier panel 8 tile (50336T) in the upper right portion of the drawing.

The data shown in Figure 5-6 is important when combined with the analysis of the slag deposition. The slag deposition on the upper RCC panel 8 was analyzed using sophisticated cross sectional optical and scanning electron microscopy, microprobe analysis, and x-ray diffraction to determine the content and layering of the slag deposition. This analysis indicated that the materials in this area were exposed to extremely high temperatures, since Cerachrome insulation was deposited first and its melting temperature is greater than 3200 degrees Fahrenheit. The analysis also showed no presence of Aluminum 286 in the slag indicating that the RCC attach fittings were not in the direct line of the breach and that the Inconel 718 spanner beam was one of the first internal items to be subjected to heating. Inconel slag was prevalent in much of the analyzed slag indicating melting of the spanner beam, foil, and associated insulation. Aluminum was found in the last deposited layer indicating the wing honeycomb spar was the last area to be subjected to hot gas flow.

Analysis of the slag deposition on the lower carrier panel 9 tiles was also performed. Materials on these tiles are consistent with wing leading edge materials (Aluminum, Inconel, Nickel alloy, and Carbon) indicating an outflow from the panel 8 area across the tiles. Tile slumping in this area is indicative of temperatures in excess of 3000 °F. The upper carrier panel 8 tile was also analyzed and the results were similar to lower carrier panel 9 except that this tile appeared to have more Cerachrome and Nextel fiber deposits. These materials are consistent with the insulator that protects the wing leading edge spar and with flow moving toward the upper wing surface through the vent between the upper carrier panel and RCC.

This forensics analysis further corroborates the breach location to be the lower portion of RCC panel 8 below the apex, approximately midway between the apex and where the RCC panel meets the carrier panel. Based on the flow

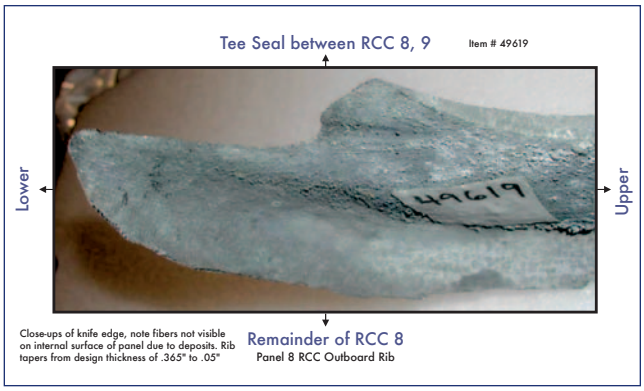

Figure 5-4. Example of rib erosion.

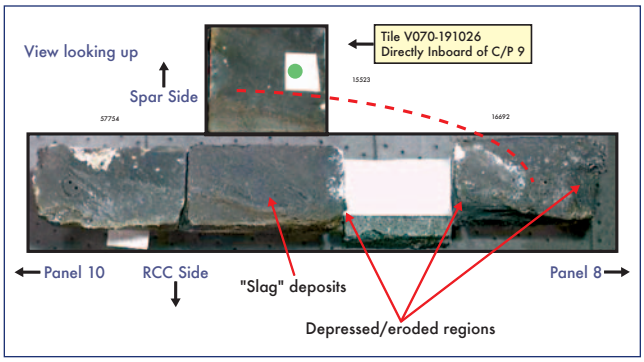

Figure 5-5. Flow on the lower carrier panel 9 tiles.

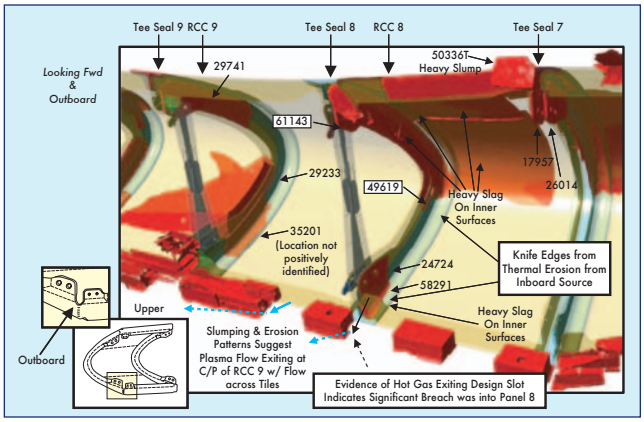

Figure 5-6. CAD drawing of the recovered debris showing overall slag deposition and erosion patterns.

patterns, the breach was in an area that caused the flow to impact the spanner beam associated with Tee seal 8 and create the knife edge erosion shown in this area in Figure 5-6.

The flow appears to have entered through this breach and into the lower aft corner, exiting through a slot toward carrier panel 9. The flow burned through the horse collar and eroded and slumped the carrier panel tiles. The flow continually grew the hole in panel 8 as time progressed and it eroded the remaining aft flange part of RCC panel 8 and the forward flange on RCC panel 9. Although the lower carrier panel 9 tiles are slumped and eroded, there must have been

an RCC rib protecting the adjacent carrier panel 8 tiles since there is no erosion or slumping of these tiles. Compared to the severely eroded carrier panel 9 tiles, the three recovered carrier panel 8 tiles are in relatively pristine condition, and likely separated due to backside heating with no indications of mechanical damage occurring prior to vehicle break-up.

As time progressed, the Cerachrome and Inconel wing spar insulators were eroded, and eventually hot gas flow impinged on the wing leading edge, burning through the honeycomb spar. Figure 5-7 depicts the possible flow direction and deposition of various metals as determined by this analysis.

In addition to the slag deposition and flow analysis, there are two other significant pieces of data that point to a breach in the RCC 8/9 area as the initial damage. The first item is the location of the leading edge RCC in the debris footprint. Figure 5-8 shows the recovered RCC for both the left and right wing and its location in the debris footprint. The eroded RCC pieces from panels 8 and 9 are found in the westernmost part of this debris footprint near Waxahachie, Texas, along with other pieces of RCC panel 8. Left wing RCC panel 9 and other aft panels appear to have been lost relatively early in the break-up sequence since their footprint spans the western to center part of the footprint. This is indicative of a left wing breach in the panel 8/9 area. The forward portion of the RCC panels on both the left and right wings (panels 1 through 7) are found from the center to eastern part of the debris footprint possibly indicating that these were lost in a secondary aerodynamic break-up.

The second additional piece of data is an upper left wing tile recovered near Littlefield, Texas. Littlefield is a small town near the Texas/New Mexico border along *Columbia*'s

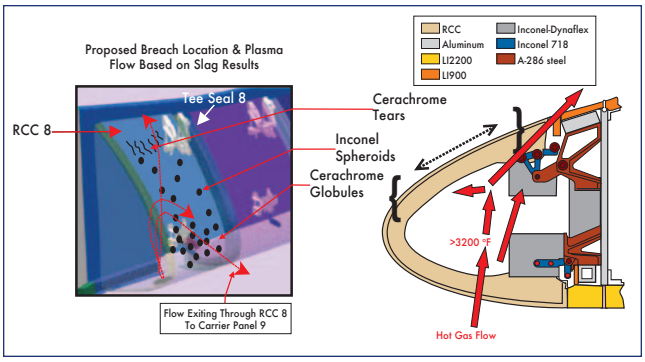

Figure 5-7. Analysis results show possible flow direction and deposition of metals.

ground track. This tile is the westernmost piece of debris that has been found to date in the debris recovery efforts. Due to the unique features of the tile (thickness, shape, paint, etc.), the tile must be from the upper wing area in the RCC panel 9 area. Figure 5-9 shows the only three possible locations for this tile.

The tile departed the orbiter more than one minute prior to final break-up due to prolonged internal heating of the upper wing skin in the area shown in Figure 5-9. The tile shows indications of backside heating and an RTV debond. It was not a failure in the densification layer, which would have been caused by mechanical loading. This piece of recovered debris is not very significant on its own merit; however, it is consistent with the previously discussed forensics data (rib erosion, carrier panel 9 tile slumping, etc.) and other events that will be discussed later in Section 5.4.

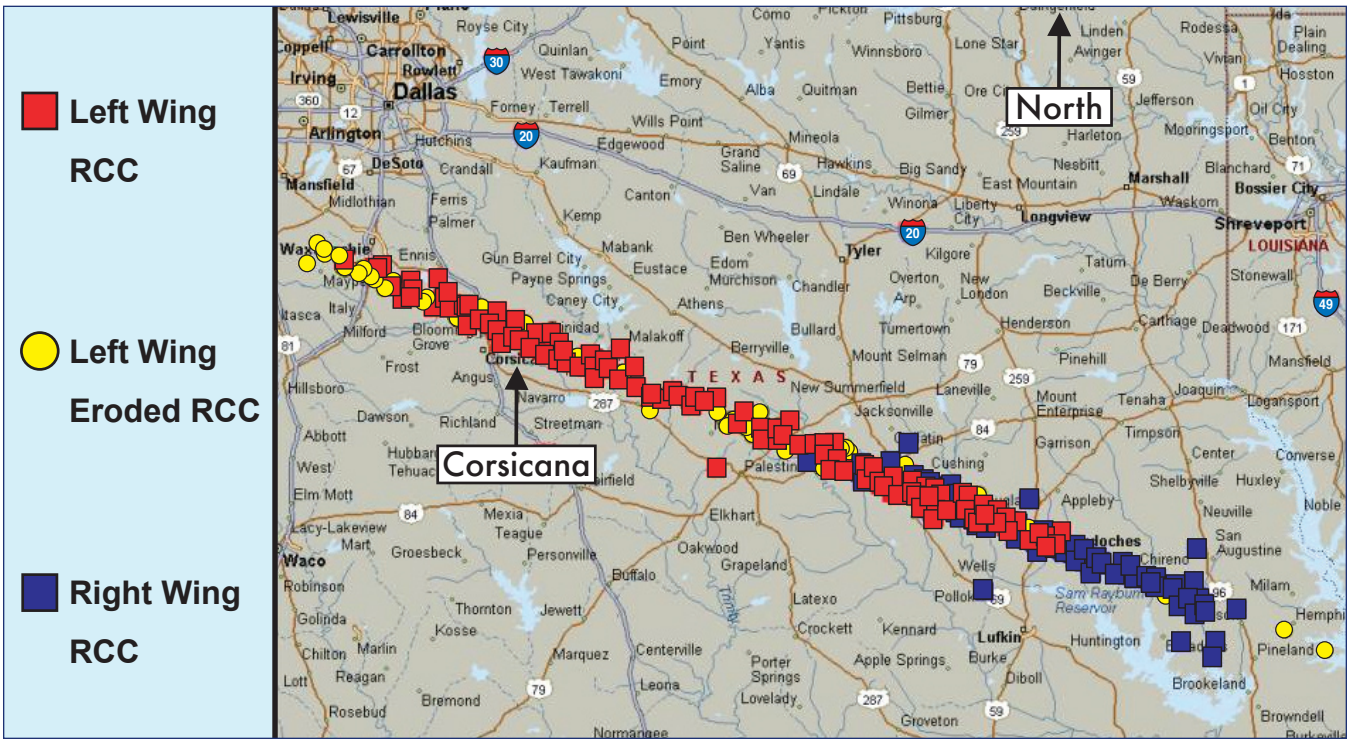

Figure 5-8. RCC panel debris location.

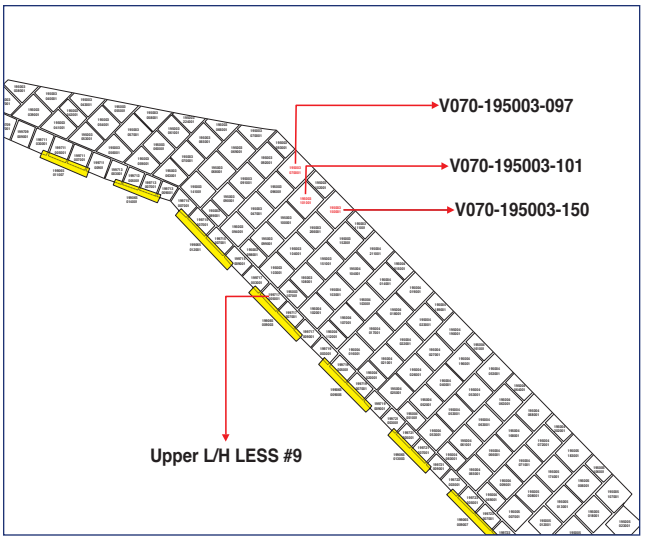

Figure 5-9. Three possible orbiter locations of the Littlefield tile on left wing.

5.4 Entry Events Timeline

5.4.1 Early Entry Heating Events

Columbia successfully completed the deorbit burn at 8:18:08 EST over the Indian Ocean. The deorbit burn and entry targeting were accomplished using well-established Mission Control Center procedures, and there were no problems identified with this process. Both the left and right Orbital Maneuvering System (OMS) engines performed nominally and the post burn residuals were less than 0.2 feet per second indicating a precise burn. The maneuver to the Entry Interface (EI) attitude, the Forward Reaction Control System Dump, and remaining Auxiliary Power Unit (APU) start (APU 1 and APU 3) were accomplished nominally.

At 8:44:09 EST, *Columbia* reached EI, the transition between orbital and atmospheric flight. The altitude was 400,000 feet and the orbiter was traveling Mach 24.6 in wings level (zero degree bank) attitude with a nominal 40-degree angle of attack. The orbiter guidance had been moded to OPS 304 nominally at five minutes prior to entry interface. OPS 304 is the name given to the entry flight software that contains the aerojet digital auto-pilot control mode. It is used from five minutes prior to EI through Mach 2.5. Figure 5-10 is a plot of dynamic pressure and stagnation heating from EI to vehicle break-up. The plot shows that both heating and dynamic pressure were very low during the two to three minutes (120-180 seconds) after EI. The heating rate shown is stagnation heat flux that is the allowable heat flux that could be achieved by the gas if all its thermal and kinetic energy were available. For this plot and others that follow in Section 5, EI occurred at 8:44:09 EST, which corresponds to zero seconds on the plots. This is a convenient reference point for many of the entry events that will be discussed.

At approximately 8:48:39 EST (EI + 270 sec.), a left wing leading edge spar strain gauge began a small off-nominal increase. Figure 5-11 shows the STS-107 response of this

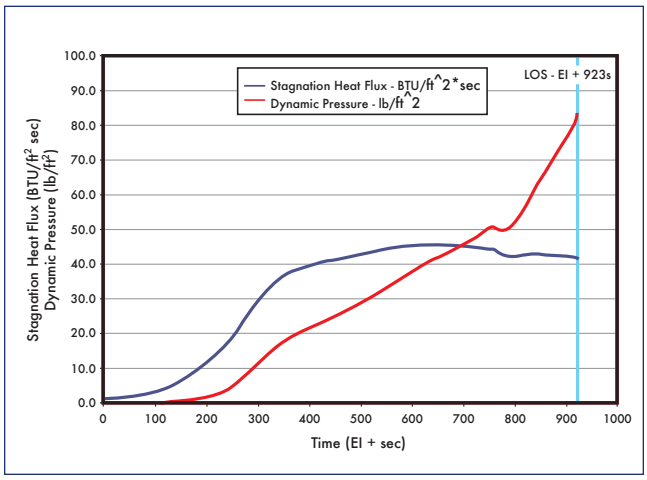

Figure 5-10. STS-107 stagnation heat flux and dynamic pressure. Note that EI was at 8:44:09 EST.

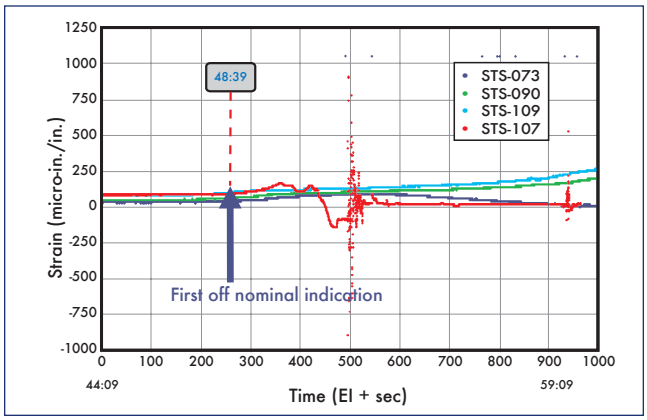

Figure 5-11. Left wing RCC panel 9 strain gauge is first measurement to indicate an off-nominal event. Note that EI was at 8:44:09 EST.

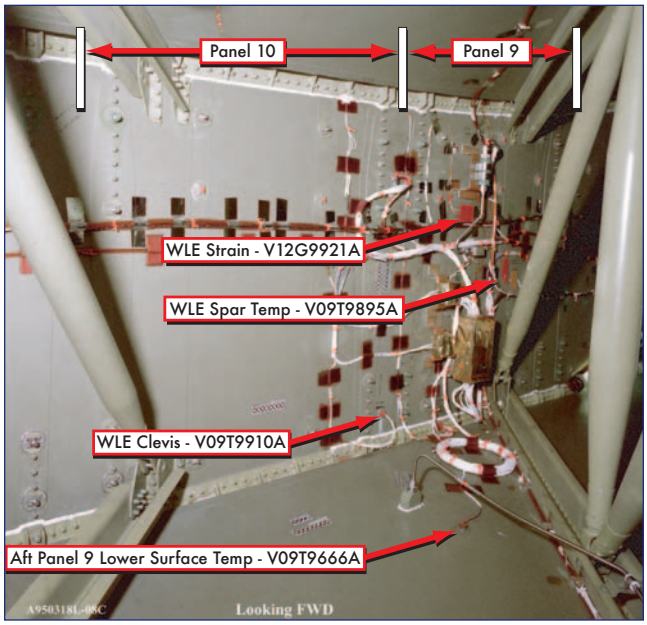

Figure 5-12. MADS sensors inside left wing.

strain measurement along with three other previous *Columbia* missions. Figure 5-12 shows the location of this sensor (WLE Strain V12G9921A) and others on the wing leading edge. The damage in lower RCC panel 8 is believed to be the cause of this strain increase. The breach allowed hot gas intrusion onto the panels 8 through 9 wing leading edge spar area leading to extreme heating and thermally induced strain. The strain increase grew over time and reached a maximum at approximately 8:50:09 EST (EI + 360 sec.). Thermal and structural analyses indicate that a breach would need to be within approximately 15 inches of the strain gauge to create the observed strain increase.

Twenty seconds later at 8:48:59 EST (EI + 290 sec.), the left wing lower attach clevis temperature sensor (between RCC panel 9 and 10) began an early off nominal temperature trend. Figure 5-13 shows the abnormal temperature response when compared to other *Columbia* missions. This temperature rise is consistent with an early entry of hot gas into the RCC cavity. This Modular Auxiliary Data System (MADS) measurement (V09T9910A) is the only temperature measurement located in the RCC cavity along the left wing leading edge. It is positioned on the lower attach fitting between panel 9 and 10 and is well protected thermally by Inconel foil insulation. The sensor is also thermally isolated since it sits on the attach fitting away from other structure as shown in Figure 3-12. In order to get an early temperature rise for this sensor, unlike that observed on any other flight, there must be a path in the RCC cavity to allow hot gas to reach the sensor.

A thermal analysis was performed with heating rates from various hole sizes in the bottom of RCC panel 8 in an attempt to match this temperature rise. The analysis used a thermal math model of the wing leading edge (Inconel Cerachrome insulation, Inconel 718 and A-286 steel attach fittings, and aluminum honeycomb spar). The results indicated that the heating equivalent of a 6 to 10 inch diameter hole with a 10 percent "sneak flow" around the insulation would be required to match the thermal response of the clevis temperature. In the same timeframe several MADS lower surface temperatures on the left wing showed a slight off nominal early temperature rise when compared to previous flights of *Columbia* of the same inclination.

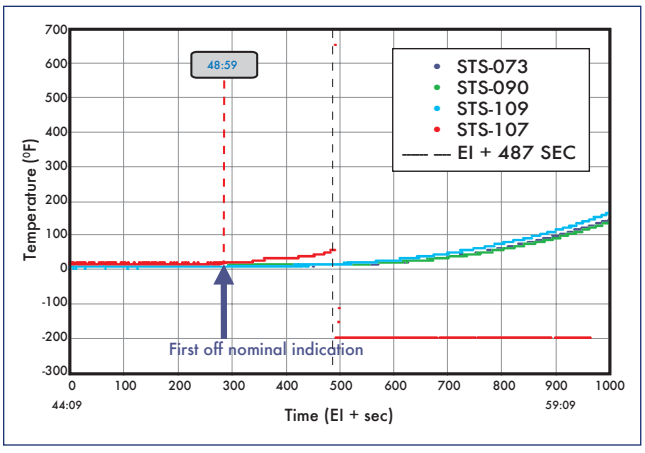

Figure 5-13. Left wing RCC panel 9/10 clevis temp sensor is second measurement to indicate an off-nominal event.

5.4.2 First Roll Maneuver Through Wing Spar Breach

Columbia executed a nominal roll to the right at 8:49:32 EST (EI + 323 sec.) as the entry guidance software began to actively control energy (i.e., closed loop guidance) to land at KSC. This initial roll command is also timed to ensure atmospheric capture by reducing the lift on the vehicle. Within 17 seconds of this maneuver, at 8:49:49 EST (EI + 340 sec.), four left OMS pod surface temperature measurements showed an off-nominal trend with lower temperature rises when compared to similar *Columbia* missions. A sample of these measurements compared to other *Columbia* missions is shown in Figure 5-14, and the location of these measurements on the left OMS pod forward face can be found in Figure 5-15.

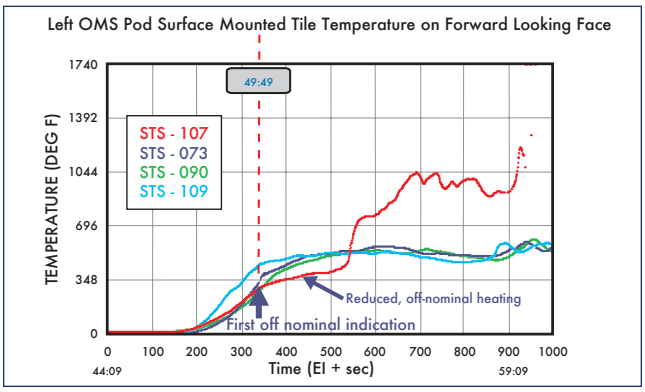

Figure 5-14. Typical off-nominal OMS pod thermocouple (V07T9220A).

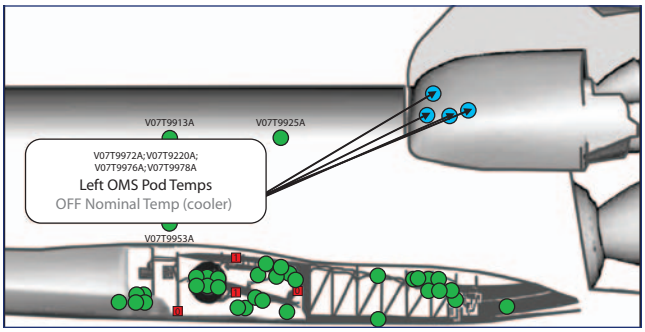

Figure 5-15. Location of OMS pod thermocouples off-nominal low.

The reduced heating is not completely understood since the weak aerodynamic flow field on the upper surface of the orbiter is difficult to model and is extremely sensitive to disturbances. The best explanation for this reduced heating is that flow into the RCC cavity was venting through to the upper surface of the wing through an existing 0.1-inch vent between the RCC and upper surface carrier panels. This vent exists all along the leading edge from RCC panel 1 through panel 22 and has an approximate area of 66 square inches. This upper surface RCC venting and the flow disturbance created by the panel 8 and upper carrier panel 8 damage caused the vortices from the canopy or area where the wing

meets the orbiter fuselage to move from their normal positions, thus reducing the heating on the OMS pod. Figure 5-16 depicts the change in the upper wing surface vortices and the weak upper surface flow.

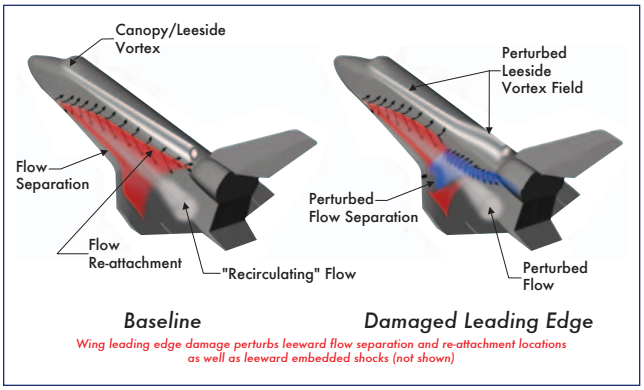

Figure 5-16. Postulated orbiter leeside flow field associated with wing leading edge damage.

In order to verify this theory of a weak upper surface flow being disturbed from venting on the upper surface, several wind tunnel tests were performed in the NASA Langley Research Center Mach 6 Tetraflouromethane (CF4) Wind Tunnel. The use of CF4 as the gas for the flow analysis is required to best replicate the Mach number environment during this timeframe. These wind tunnel tests used a ceramic model and a 0.01-inch leading edge vent to mimic the postulated venting. Nitrogen gas was allowed to flow through this upper surface vent via a gas supply line. A picture of this model is shown in Figure 5-17. Results of this testing show that it is feasible to obtain reduced heating on both the left OMS pod and the left fuselage as a result of flow through the RCC upper surface vent. Figure 5-18 shows the change in heating as the vent velocity is altered.

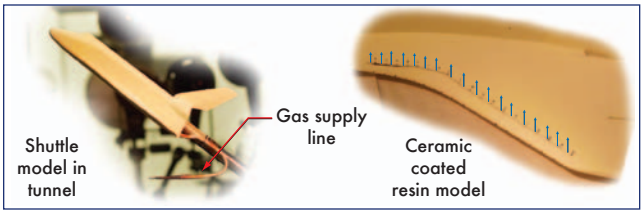

Figure 5-17. Orbiter wind tunnel model with vent gap along wing leading edge.

Over the next 43 seconds, there were five communications dropouts beginning at 8:50:00 EST and ending at 8:50:43 EST (EI + 351 through 394 sec.). It is possible that hot gas in the RCC cavity had begun to erode the Inconel and Cerachrome insulation along the wing leading edge spar. Molten materials could have been ejected into the environment around the orbiter creating multi-path signal scattering with the link between the orbiter and the western Tracking and Data Relay Satellite (TDRS). The best parallel for this explanation is chaff used by some military aircraft to confuse opposing radar systems.

Forensic analysis of the recovered left OMS pod debris indicates that molten Inconel 718 and A-286 cress were sprayed onto the left OMS pod during entry. This OMS pod debris and the left side of a recovered vertical tail debris piece were significantly pitted by this metallic spray supporting the concept that there was vaporized metal in the environment around *Columbia*. These materials must have originated from the RCC panel 8 wing spar damage area since Inconel 718 is used as the wing leading edge insulator and A-286 is used for the RCC attach fittings.

In the same timeframe, at 8:50:09 EST (EI + 360 sec.), a left payload bay fuselage MADS surface temperature measurement (Figure 5-19) showed an off-nominal temperature trend. This trend is a reduced rise rate when compared to other previous *Columbia* missions, as shown in Figure 5-20. The previously discussed theory of venting and or disturbed flow due to panel 8 damage, causing a shift in the vortices on the upper surface of the wing, is also believed to be the cause of this off-nominal behavior. The flow field and venting on the upper surface rate are constantly increasing since the mass flow rate into the RCC breach is increasing as the orbiter descends lower into the atmosphere.

At 8:50:19 EST (EI + 370 sec.), a lower surface thermocouple showed signs of off nominal, increased heating. The best explanation for the increased heating in this area is severely disturbed, turbulent flow caused by the leading edge damage on the bottom of RCC panel 8 and flow from the lower corner of this panel as discussed in Section 5.3. Langley Research Center wind tunnel testing has confirmed that wing leading edge damage (notch or protuberance) near

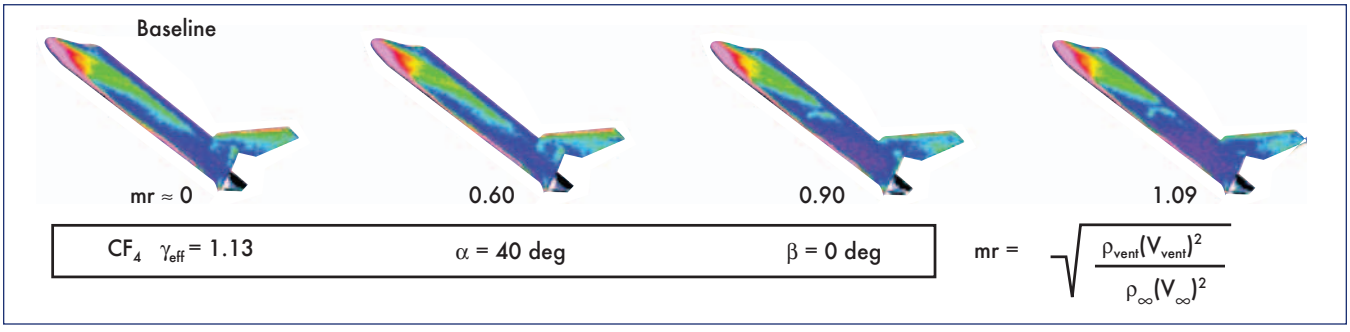

Figure 5-18. Wind tunnel model results for sensitivity of orbiter side fuselage and OMS pod heating patterns to mass addition along WLE leeside vent gap.

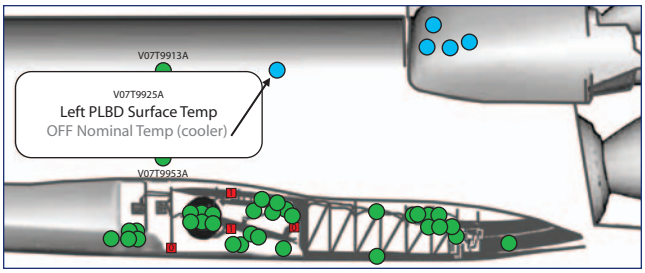

Figure 5-19. Location of left sidewall temperature sensor.

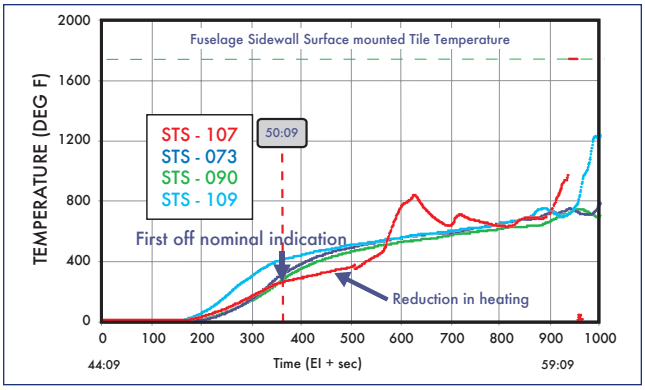

Figure 5-20. Off-nominal temperature indication on the left sidewall.

panel 8 will cause increased heating to the lower wing surface. As previously discussed, the eroded lower carrier panel tiles on panel 9 indicate this strong flow from panel 8. This is consistent with flow patterns observed on many recovered lower surface wing acreage tiles along the flow lines aft of the RCC panel 8 area. Figure 5-21 shows this temperature response as compared to other *Columbia* missions. The location of the sensor can be seen in Figure 5-22.

By 8:51:14 EST (EI + 425 sec.), the wing leading edge spar temperature began an early, off-nominal rise, shown in Figure 5-23. At the same time, the clevis temperature in the RCC panel 9/10 region continued to increase. The initial spar temperature rise was relatively slow and was caused by

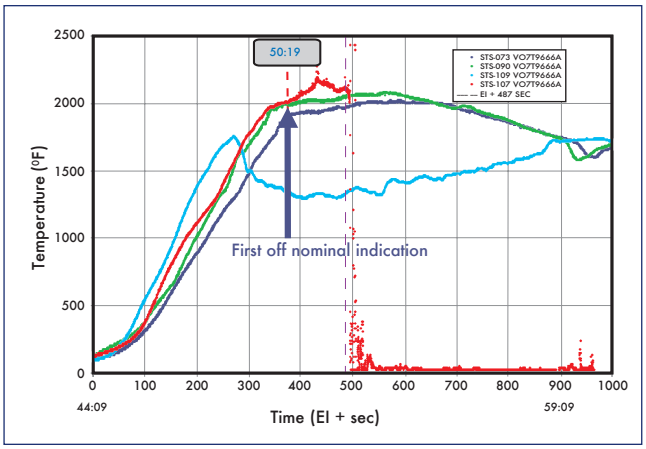

Figure 5-21. Temperature rise on tile surfaces aft of RCC panel 9.

conduction since this measurement is on the backside of the spar in the wing cavity. Eventually, the rise rate increased dramatically as first the Inconel and Cerachrome insulation and later the aluminum honeycomb were destroyed. The exact time of the spar breach is unknown; however, it is estimated to have occurred between 8:51:14 to 8:51:59 EST (EI + 425 to 470 sec.) based on the observed wing leading edge linear decrease in strain during this timeframe. A more detailed discussion of the method used to bracket the time of the wing spar breach is contained in the following section.

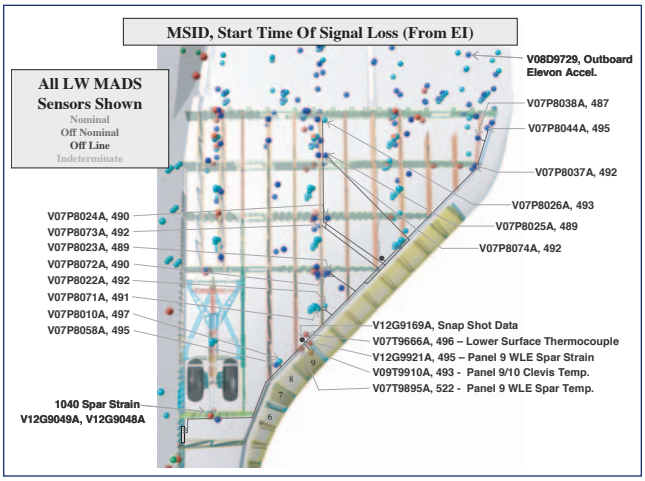

Figure 5-22. Left wing MADS sensors, including Measurement Stimulation Identification (MSID) number, and start time of loss of signal (EI + sec.).

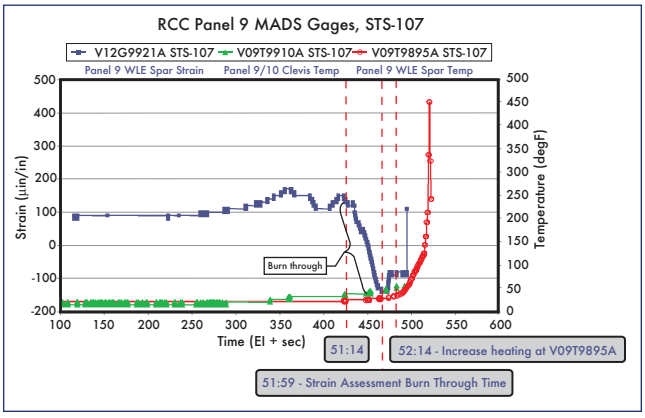

Figure 5-23. RCC panel 9 MADS strain and temperature measurements, STS-107.

At 8:51:49 EST (EI + 460 sec.), one of the left OMS pod measurements (V07T9972A) began to show an increased temperature rise, indicating that the upper surface flow has changed again. This is shown in Figure 5-24 along with this measurement on other *Columbia* missions. It is evident that the measurement rises to a higher temperature and at a faster rate than has been observed on previous missions within the next few minutes. Figure 5-25 shows other left OMS pod and fuselage temperature measurements that exhibit an off-nominal rise later in time. The sensor locations on the left side of the orbiter are also shown in Figure 5-25.

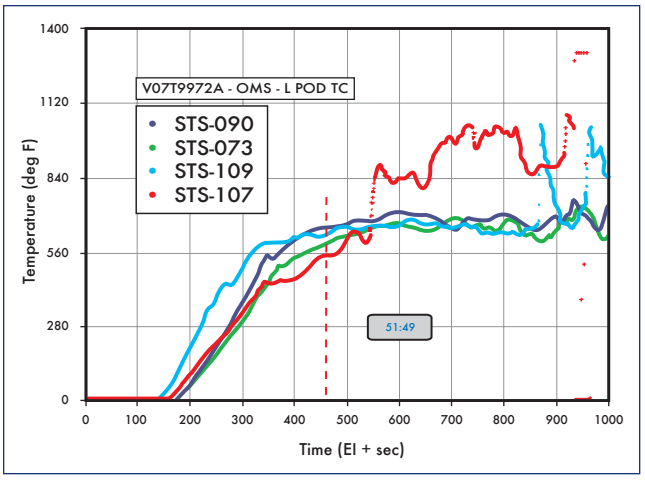

Figure 5-24. Off-nominal low OMS pod thermocouple (V07T9972A).

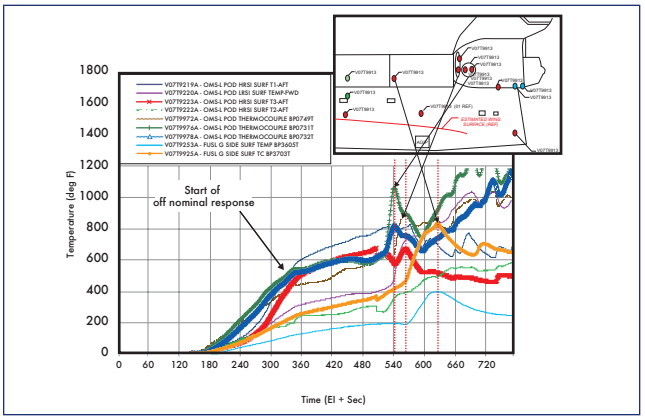

Figure 5-25. Left side fuselage/OMS pod off-nominal responses indicate increased heating.

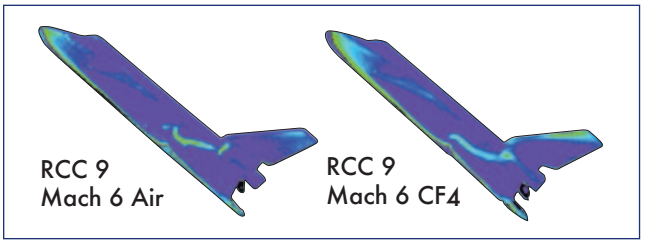

Figure 5-26. Wind tunnel test results for RCC panel 9 missing and resulting in increased heating to OMS pod.

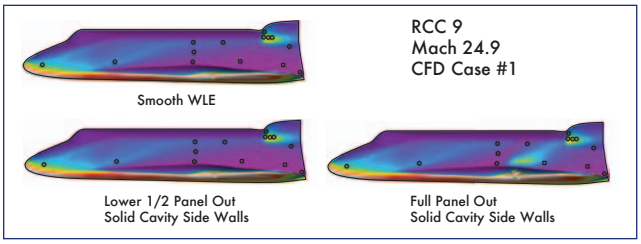

Figure 5-27. CFD results for no damage, partial damage, and full damage to RCC panel 9 show increased heating on side fuselage and OMS pod.

These off-nominal temperature rises were caused by a change in the flow field along the upper portion of the left wing as the wing leading edge (WLE) and wing spar damage progressed. The mechanism was a shift in the vortices due to venting on the upper portion of the wing and is similar to the previous discussions on lower than expected OMS pod temperatures. Wind tunnel testing and CFD analysis confirmed that WLE damage on RCC panels 8 and 9 could cause increased heating to the OMS pod due to disturbed upper surface flow or flow impingement caused by re-directed flow from the lower surface. Additionally, the molten Inconel 718 and A-286 spray onto this area are indications that this flow is the cause of these temperature rises. Figure 5-26 (from wind tunnel test results) is a representative example of increased heating on the left fuselage and OMS pod due to RCC panel 9 damage from wind tunnel test results. Figure 5-27 shows a similar picture of the left side as determined by CFD analysis. Note that neither the wind tunnel testing nor the CFD analysis accounts for increased heating that is likely due to molten metal contacting the OMS pod.

The increased heating implies that damage/erosion to the RCC panel 8 area had increased or that at least one carrier panel had been lost. The increased heating is also consistent with an increased mass flow rate due to the nature of the entry environment. The dynamic pressure and stagnation heat flux had more than doubled by this timeframe when compared to a few minutes after EI. There are three additional communication dropouts that follow at approximately 8:52:09 EST to 8:52:31 EST (EI + 480 to 502 sec.). Again, these dropouts are consistent with molten aluminum and other metals being released into the environment surrounding *Columbia*.

5.4.3 Wing Breach and Wire Failures

The next significant event was a breach through the left wing leading edge spar leading to many wire measurement failures and eventual deformation of the left wing. As discussed in Section 5.4.2, by approximately 8:52:00 EST (EI + 471 seconds), strain and temperature measurements indicated that hot gas had begun to weaken the wing spar. Figure 5-28 shows that the orbiter has entered the peak-heating region during this timeframe and would remain there for many of the ensuing events that will be discussed later.

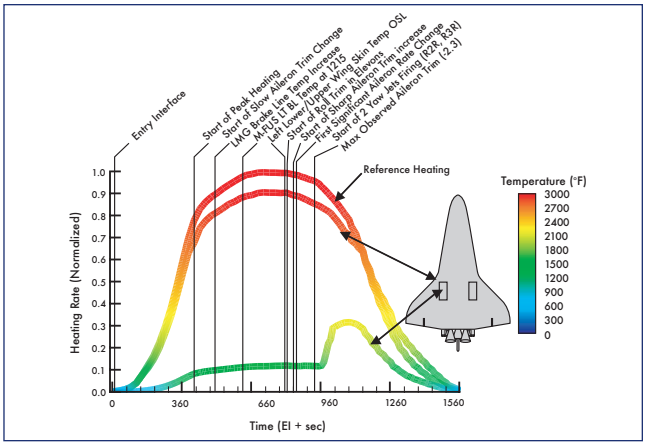

Figure 5-28. STS-107 entry heating rate profile.

The precise timing of the wing spar breach is difficult to determine, and three different techniques were used in an attempt to bound the breach time. These techniques included a structural assessment using the wing leading edge spar measurement, use of a thermal model to predict the time required to burn through the spar insulators and then the honeycomb structure, and a wire failure assessment.

The first technique used the strain response, shown earlier in Figure 5-23. On this plot, the initial strain rise that began at about 8:49:09 EST (EI + 300 sec.) is due to thermal elastic strain. It appears that the spar structural softening occurs at approximately 8:50:09 EST (EI + 360 sec.), followed by loss of the structural integrity, or breach, at approximately 8:51:14 EST (EI + 425 sec.). This appears to be completed by approximately 8:52:00 EST (EI + 471 sec.). A detailed structural model that attempted to reproduce the thermal strain response observed during this timeframe confirmed this timing. This analysis determined that the location of the spar breach must be within about 15 inches of the spar strain measurement. This would locate the spar breach near the intersection of panel 8/9, as shown in Figure 5-29. The flow through the RCC breach maintained some directionality although it was influenced by the shape of the hole, remaining RCC structure, attach hardware, and leading edge insulators. Overall, this strain response is consistent with an RCC breach in the lower part of panel 8 as previously discussed in Section 5.3. Although it is difficult to pinpoint a precise location of the RCC breach, this analysis supports the argument that the breach was closer to the panel 8/9 intersection and Tee seal 8.

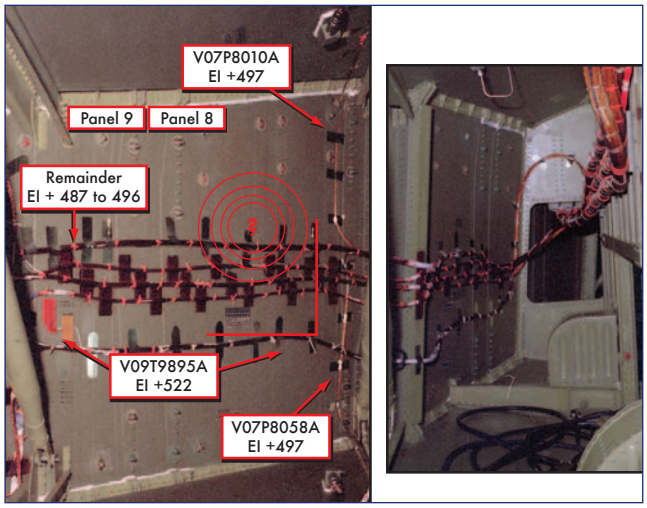

Figure 5-29. Cable routing on wing leading edge and wheel well wall.

The second technique used a detailed thermal model to determine the time required to burn through the various insulations immediately in front of the wing leading edge spar (Inconel, Nextel, Cerachrome) and then the honeycomb spar. This model assumed the equivalent heating of a six-inch diameter hole in the bottom of RCC panel 8. Using the expected aero heating rate and the various material properties, the spar burn through occurred at 8:52:19 EST (EI + 490 sec.). This time would be accelerated slightly for a larger diameter hole. The results of this thermal model are shown in Figure 5-30.

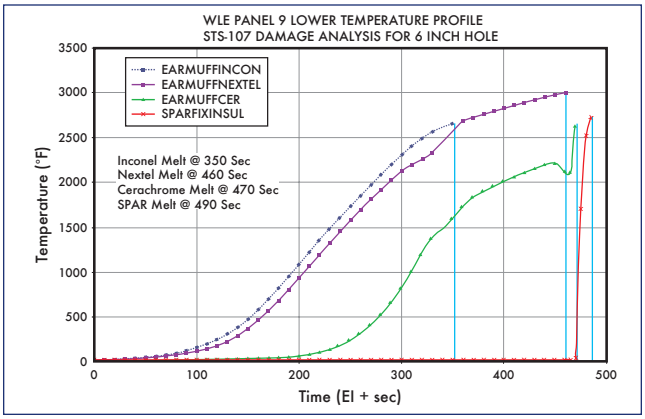

Figure 5-30. Thermal model prediction of wing spar burn through.

The final technique used was an examination of the wire failures on the wing leading edge spar. These wire runs are shown in Figure 5-29. The first measurement loss was a MADS upper left wing pressure measurement, which failed at approximately 8:52:16 EST (EI + 487 sec.). This measurement is contained in the upper wire bundle in the left photo in Figure 5-29. The combination of these three separate and distinct analyses results in a range of wing spar breach times as early as 8:51:14 EST and as late at 8:52:16 EST (EI + 425 to 487 sec.).

Immediately after the breach, hot gas inside the wing began to heat the remaining wire bundles that contained real-time telemetry and the recorded MADS measurements. Figure 5-29 shows an inside-the-wing view of the approximate breach location based on this wire failure analysis. The view on the left is of the panel 8/9 spar location. This area is not visible in the right photo, which contains the transition spar and a view of the three wire bundles along the outside of the wheel well wall. Figure 5-31 shows the overall spar breach location with respect to the rest of the wheel well. The distance from the spar to the wheel well wall in this area is approximately 56 inches, as shown in Figure 5-32. Figure

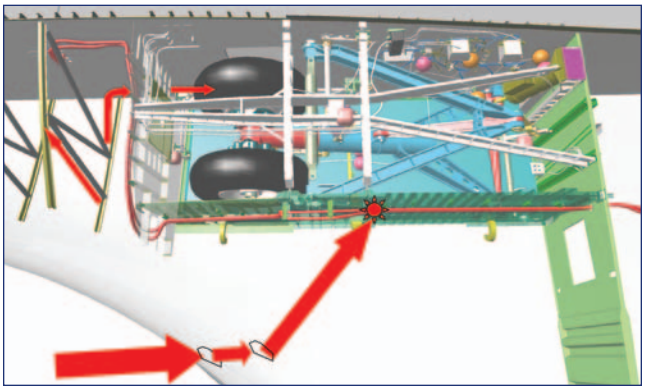

Figure 5-31. Hot gas begins to fill left wing.

5-33 shows a sketch of the venting of the left wing into the payload bay, driving the direction of the internal flow depicted in Figure 5-31. Note the 142 square inch vent into the midbody fuselage located forward of the wheel well.

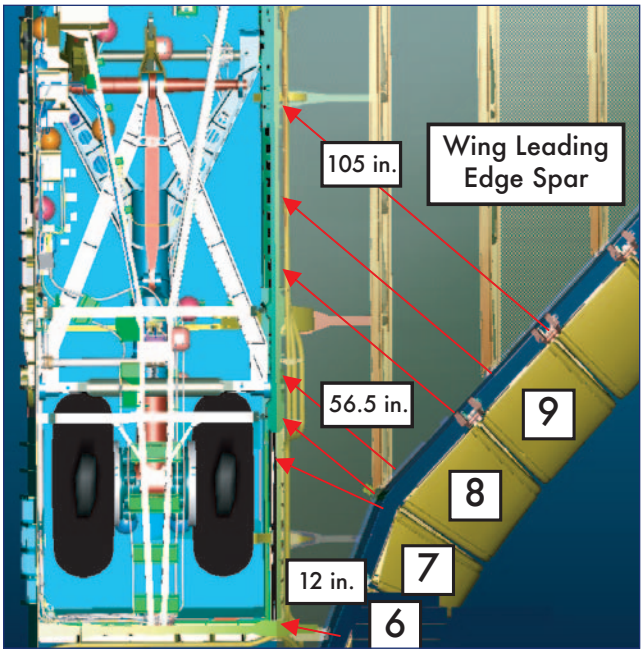

Figure 5-32. Columbia LH wing and wheel well geometry.

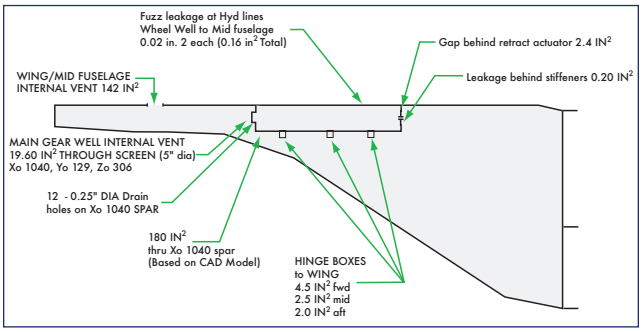

Figure 5-33. Columbia LH wing and wheel well vent model (wheel well leak paths based on Atlantis test comparison).

One hundred sixty-three other measurements failed very quickly over the next two minutes. Figure 5-34 is a plot of the percentage of measurements lost as a function of time from EI. The first measurements to fail are all located on the wing leading edge spar as shown by the purple line on the plot. Bundles 1, 3, and 4 along the wheel well (shown in Figure 5-35) began to fail about 14 seconds after the first spar measurements. This is indicative of a plume impinging on the wire bundles on the wheel well wall.

Arc-jet testing was performed in a facility at JSC to demonstrate how quickly a hole in a 0.1 inch thick aluminum plate would grow in an attempt to determine the feasibility of a rapid spar burn through followed by rapid wire measurement failures. The test configuration had an initial 1-inch diameter hole, and a stagnation heat rate of 12.13 BTU per square foot per second (equivalent to the flight environment at about 8:50 EST, EI ~ 351 sec). During the test, the aluminum plate hole grew from 1 inch in diameter to 5 inches in diameter in approximately 13 seconds. This was consistent with thermal math models developed to analytically predict hole growth. A wire bundle placed 15 inches from the heat source showed very rapid erosion after the hole grew to 5 inches in diameter. The measurement losses in this bundle were very consistent with those observed for wire bundle number 3 (see Figure 5-34). The hole would have grown to a larger diameter; however, the test set-up provided a heat sink that eliminated further hole growth. Overall, the test indicated that a hole in the aluminum honeycomb would grow rapidly, allowing a substantial plume to destroy the wire bundles on the wheel well wall.

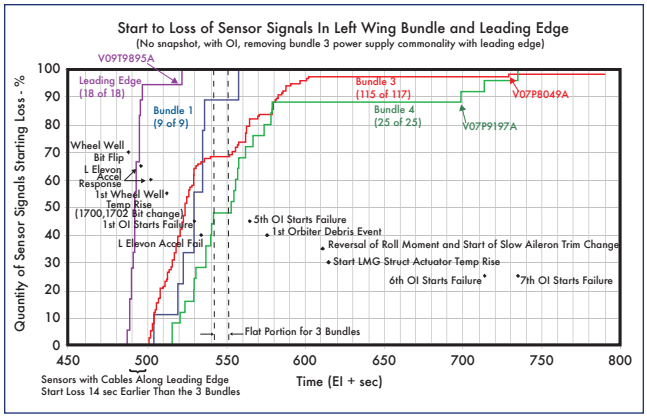

Figure 5-34. MADS data failure due to wire burning.

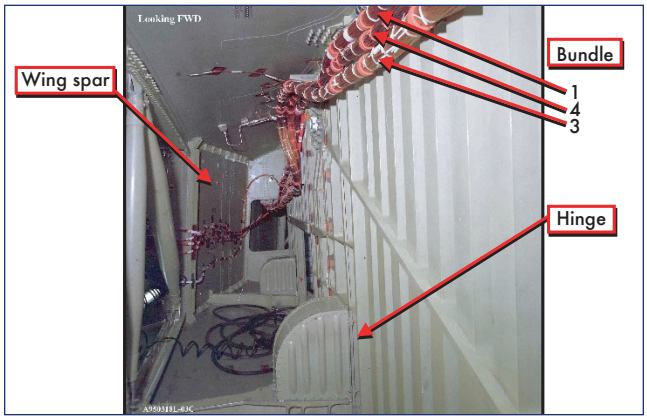

Figure 5-35. View of cables running along outside of wheel wall cavity bulkhead.

Four additional measurements failed after 8:54:16 EST (EI + 605 sec.) with the last starting to fail at 8:56:24 EST (EI + 735 sec.). This last measurement failure took over a minute to fail completely. Figure 5-34 and Figure 5-35 show the measurement loss timing and the wire bundle runs along the wheel well. Although almost all measurements internal to the wing failed, two strain measurements on the 1040 spar (forward of the wheel well) were unaffected and produced data until loss of all MADS data at 9:00:13 EST (EI + 964 sec.). Figure 5-36 shows the location of the sensors on the forward

wheel well spar. The fact that these measurements are available until loss of data are important indicators that the RCC breach could not be forward on the panel 6 area since these measurements would have been lost as well (see Figure 5-32). These measurements also record key changes in strain that help indicate some of the changes that the left wing underwent as the remainder of the entry events unfolded.

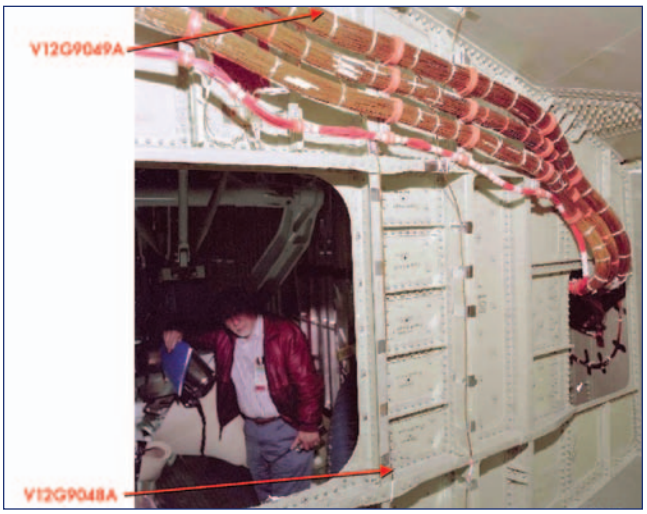

Figure 5-36. Strain measurements on 1040 spar.

A comprehensive evaluation of all MADS measurement failures in the left wing was performed to attempt to determine the spar breach progression. Each measurement's failure signature was evaluated to determine both the start time of the failure and when the wire failure was complete. As the wire burns, the short between the twisted pairs of wiring increases thereby producing the time delay effect between failure initiation and complete failure. Eighteen measurements routed on the wing leading edge and over 100 measurements in three wire bundles routed on the outboard side and external to the wheel well were used for this assessment. Seventeen of the 18 wing leading edge measurements failed in 10 seconds starting at 8:52:16 EST (EI + 487 sec.). No other MADS measurements failed during this time. The one measurement that did not fail in this time span was located in the bottom of five harnesses on the WLE. The remaining 17 measurements are in the upper four harnesses with the majority being in the top harness. This would indicate that the spar breach started near the top wire bundle and worked toward the bottom of the spar. Additionally, two of the 18 measurements join the harnesses at the panel 7 to 8 interface, making the wing spar breach outboard of panel 8 very unlikely.

5.4.4 Aerodynamic Events

Coincident with the spar breach at approximately 8:52:09 EST (EI + 480 sec.), the nose cap RCC attach clevis temperature had an off-nominal change in rise rate when compared to previous missions. This rise rate was abnormal for approximately 30 seconds and ended at 8:52:39 EST (EI + 510 sec.). The exact cause of this abnormal temperature rise is not known, but the timing is coincident with the breach of the wing leading edge spar. An explanation is that the abnormal rise is an instrumentation anomaly caused by multiple wire failures in this timeframe. This measurement response is shown in Figure 5-37 along with the same measurement for several other *Columbia* missions. This figure also shows the location of this internal nose cap measurement on the very forward portion of the left fuselage.

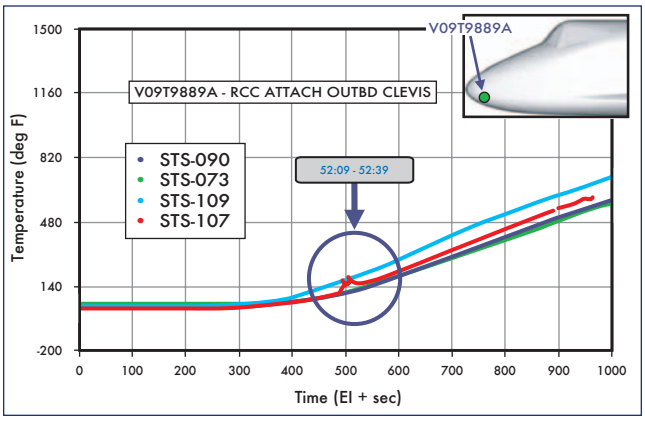

Figure 5-37. Off-nominal temperature rise rate in nose cap RCC attach clevis.

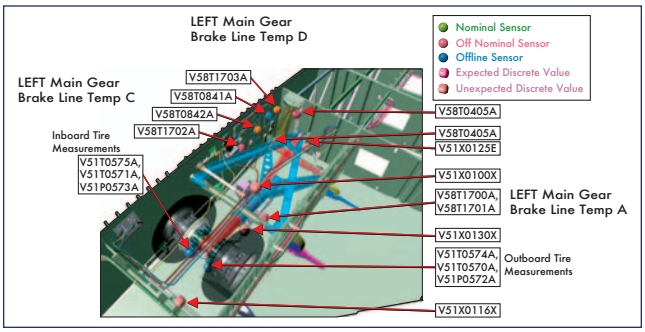

Figure 5-38. Location of sensors in the LH wing wheel well.

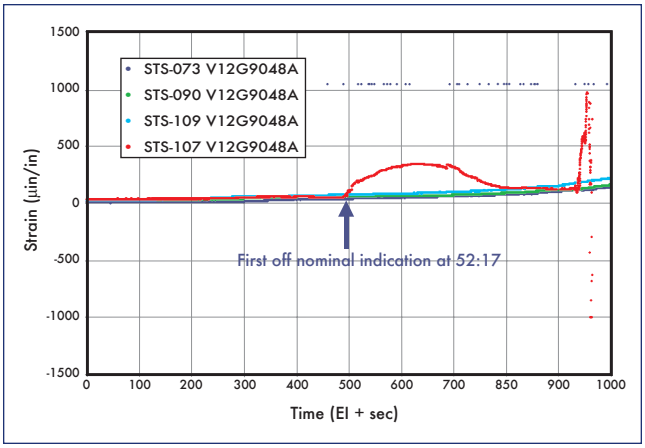

Figure 5-39. Strain rise in lower 1040 spar cap.

Until approximately 8:52:17 EST (EI + 488 sec.), there was no indication of any off-nominal situation that could be observed by the MCC or the crew in real-time. The flight control response and all orbiter telemetry measurements were

nominal. The first indication of any anomalous Operational Instrumentation (OI) was a small increase in the left main gear brake line temperature D measurement at this time (see Figure 5-38). Within one second of this time, there is a lower 1040 spar (forward wall of the wheel well) strain measurement that shows an off-nominal increase in strain (see Figure 5-39). These are both indications that the breach in the wing leading edge spar had allowed hot gas to reach the wheel well area, most likely through vent paths around the hinge covers, which allowed hot gas into the wheel well cavity.

At approximately 8:52:25 EST (EI + 496 sec.), the left outboard elevon wideband accelerometer showed an unusual 2 g peak-to-peak acceleration (see Figure 5-40). This is consistent with the timing of the many wire failures within the left wing and the timeframe when the spar breach occurs. Additionally, there are two unexplained communication dropouts in this same timeframe. Another 3 g peak-to-peak acceleration anomaly was observed at 8:52:31 EST (EI + 502 sec). Additional temperature measurements (left main gear brake line temp A and C) in the wheel well area (see Figure 5-38) began an off-nominal rise at 8:52:41 EST (EI + 512 sec.).

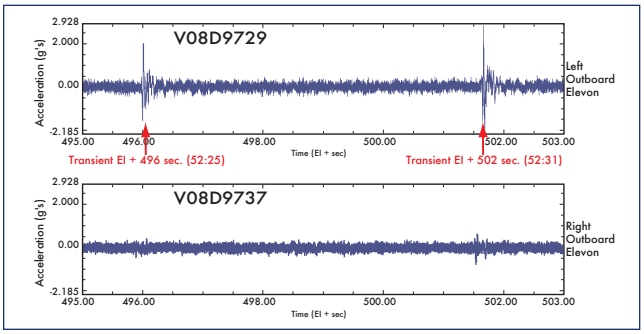

Figure 5-40. Outboard elevon accelerometer responses at 8:52:25 and 8:52:31 EST (EI + 496 and 502 sec.).

The elevon response event was followed by a change in the rise rate for two supply nozzle temperatures and the vacuum vent nozzle temperatures at 8:52:32 EST (EI + 503 sec.). The off-nominal rise rate occurred for approximately 15 seconds for the supply nozzle temperatures and 23 seconds for the vacuum vent temperatures. The location of these nozzles on the left side of the fuselage is shown in Figure 5-41, and the arrow indicates that they could have been located along a line of disturbed flow. The short, abnormal rise rate is unexplained, has not been observed on any previous Shuttle missions, and may not be associated with the upper wing disturbed flow caused by the leading edge damage. Unlike the RCC nose cap clevis temperature, the instrumentation appears to have been valid for both nozzles. Plots of this off-nominal temperature rise for one of the supply nozzle temperatures and the vacuum vent nozzle are shown in Figure 5-42.

Immediately following these events, at 8:52:44 EST (EI + 515 sec.), the aerodynamic roll and yaw coefficients that have been extracted from the flight data showed a slight negative trend (see Figure 5-43). This is indicative of more drag and decreased lift on the left wing.

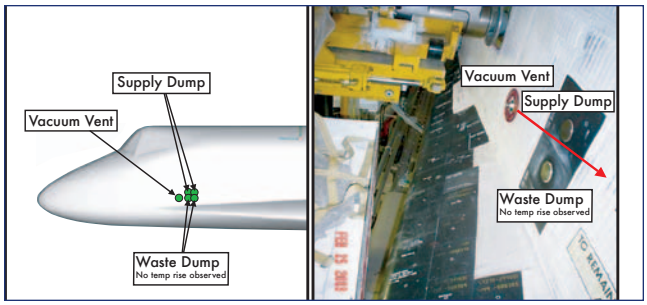

Figure 5-41. Location of supply dump and vacuum vent nozzles.

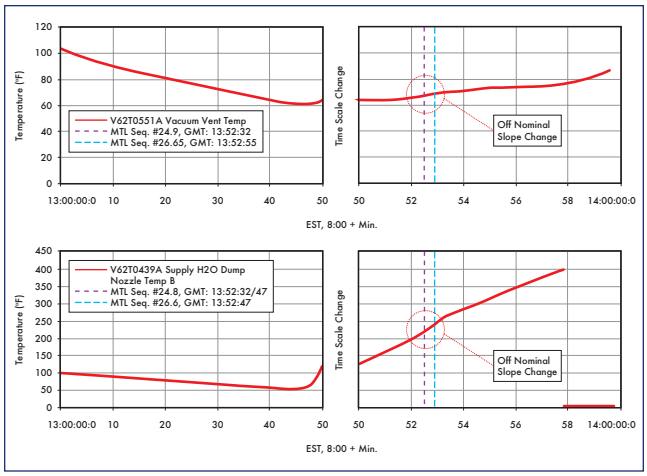

Figure 5-42. Off-nominal temperature for supply nozzle and vacuum vent nozzle.

Hypersonic wind tunnel tests indicate that both the slight negative roll and yaw deltas can be explained by leading edge damage in the lower half of RCC panel 8. This will be discussed in more detail in Section 5.4.5.

The flight control system compensated for the initial aerodynamic disturbance, and the aileron trim continued to match pre-entry predictions. To account for the increased drag the orbiter yawed slightly to the right to balance the yaw moments. The inertial sideslip exceeds flight history at 8:53:38 EST (EI + 569 sec.); however, this small departure was well within the vehicle's capability to control. There was also another communication dropout in this timeframe (8:52:49 to 8:52:55 EST, EI + 520 to 526 sec.).

By 8:53:28 EST (EI + 559 sec.), *Columbia* had crossed the California coast. After this coastal crossing, there are indications of damage progression on the left wing since the temperature response on the upper surface changes and measurement losses continue in the left wing. At 8:53:29 EST (EI + 560 sec.), several left fuselage temperature measurements showed an unusual 400 degree temperature increase over the next minute. These measurement increases were accompanied by another short communications dropout.

At 8:53:39 (EI + 570 sec.), four left OMS temperature measurements also exhibited an unusual temperature rise. This temperature rise is attributed to shifting of the left wing lead-

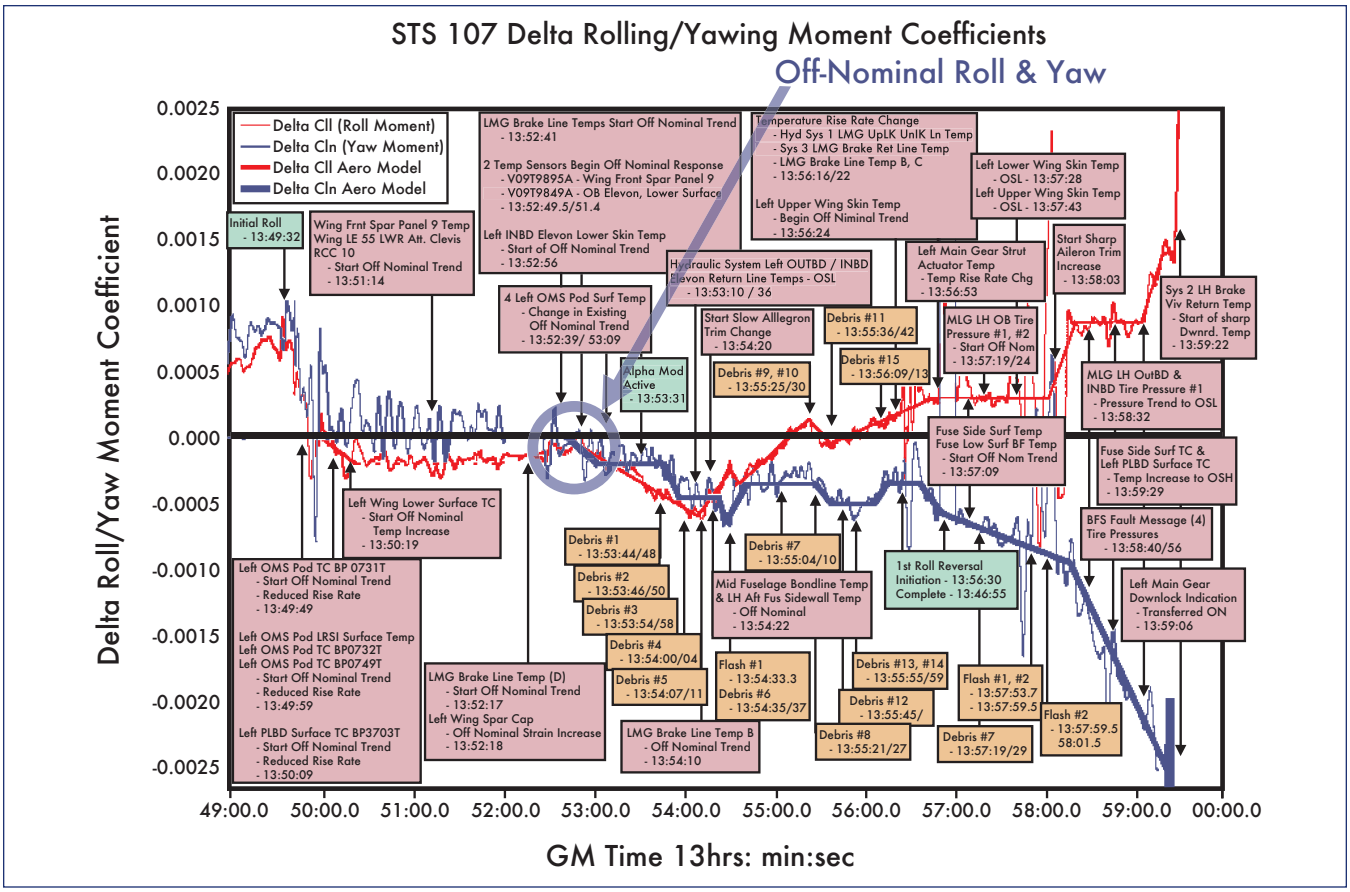

Figure 5-43. First noted off-nominal aero event.

ing edge upper surface vortices due to interaction with disturbed flow caused by damage progression in the RCC panels 8 through 9 area. During this same timeframe, the upper cap strain gauge on the 1040 spar began an off nominal increase indicating continued heating internal to the left wing.

By this point in the entry almost all measurements in the left wing had been lost and there appeared to be a temporary decrease in the measurement failure rate. It is possible that the "lull" in measurement failures was caused by a release of upper wing skin and FRSI. The breach in the upper wing surface and resulting pressure differentials internal to the wing would shift the internal plume impingement location relative to the wiring. In this same timeframe, there were multiple debris events captured on video by public ground observers beginning at 8:53:46 EST (EI + 577 sec., 20 seconds after California coastal crossing) and ending at 8:54:11 EST (EI + 602 sec.). The source of the debris may be upper wing skin and other thermal protection system (TPS) elements.

Since the wing had been ingesting hot gas for over two minutes, it is quite probable that significant internal damage to the wing occurred over this timeframe. The aluminum structure in the wing was not designed for high heating and many of the components are unlikely to survive this heating environment. For example, aluminum's melting point is ~1200 °F, but the ingested gas into the wing may have been up to 8000 °F near the breach. There were other communication dropouts in this timeframe as well (8:53:32 to 8:53:34 EST, EI +563 to 565 sec.).

In the 8:54:10 to 8:54:35 EST (EI + 601 to 626 sec.) timeframe, several key events occurred. The first event at 8:54:10 EST (EI + 601 sec.) was an indication that the temperatures in the wheel well had a greater rise rate, indicating the sneak flow or breach into the wheel area had increased. The roll moment trend changed sign at 8:54:11 EST (EI + 602 sec.) almost simultaneously with the change in wheel well temperature rise rate as shown in Figure 5-44, followed by a debris flash event at 8:54:33 EST (EI + 624 sec.). A large debris item, labeled debris event six, was seen leaving the orbiter two seconds later. This debris event and the roll moment trend change are believed to be created by growing damage to *Columbia*'s left lower wing.

There are several theories that attempt to explain this response including a change in the wing camber or shape due to deformation and a lower wing recession, caused by the loss of much of the support structure internal to the wing. Wing recession here is in reference to structural deformation of the wing surface. In this case, one or more areas on the lower wing form a more concave shaped depression of wing skin and tiles as a result of the structural support in those areas being weakened or lost. A structural analysis of both wing deformation due to the loss of three ribs internal to the wing, and the wing recession concept was performed.

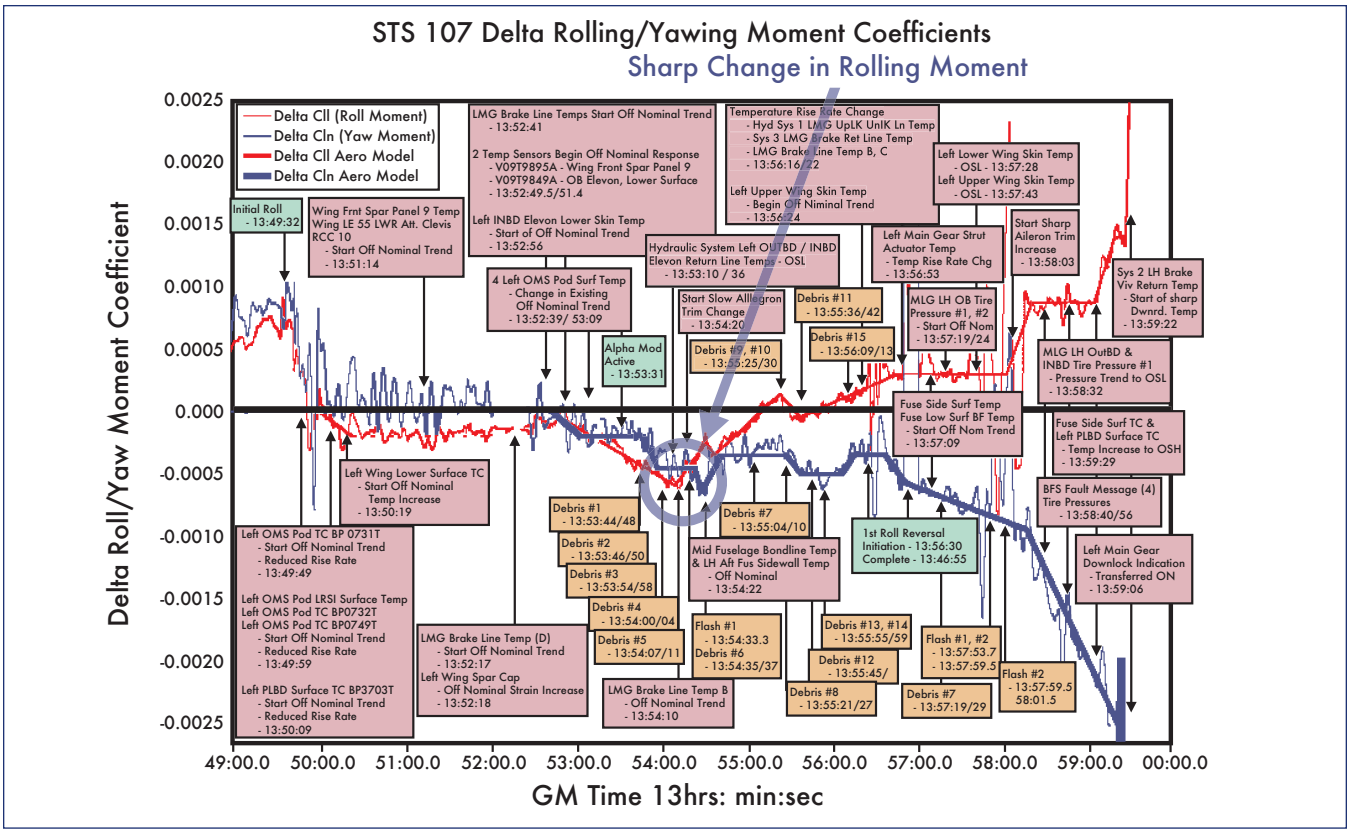

Figure 5-44. Sharp change in rolling moment.

Structural and aerodynamic analysis of wing deformation was performed without any type of recession in the wing lower surface. An assumption of 70 pounds per square foot was used for wing loading. Heat transfer coefficients were updated from previous coupled venting and thermal models for the left wing. A structural model was used along with the heating equivalent of a 10 inch diameter breach in the wing spar beginning at 8:52:16 EST (EI + 487 sec.) assuming 100 percent of the energy from this hole was transferred to the wing interior. Two different cases were analyzed: one with no breach in the upper wing skin and another with a 5 inch diameter breach in the upper skin at 8:54:37 EST (EI + 628 sec.) when a significant visual flash event was observed. Both cases showed that the temperatures of the wing skins, wing spars, and the wheel well wall were high enough by 8:58:19 (EI + 850 sec) that significant damage to the wing structure would occur. Figure 5-45 shows the potential area of damage and that significant deformation of the intermediate wing area and/or a recession in the lower surface is possible.

It is difficult to postulate the exact wing deformation that occurred. One case is localized leading edge damage, resulting in global wing deformation. Local deformation was relatively small, less than 1.0 inch in the damage area with a 0.25-inch global increase in wing tip deflection. Delta rolling and yawing moments were calculated for this case, and they were very small, approximately +0.0001 for roll and -0.0001 for yaw. Another case looked at deformation resulting from the loss of three internal ribs. Again, the local deformation

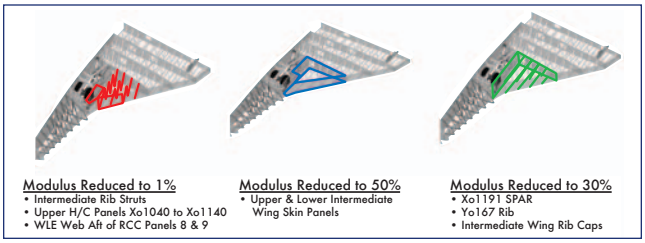

Figure 5-45. Modeling results show potential area of damage and that significant deformation of the intermediate wing area and/or a recession in the lower surface are possible.

was small (approximately 5 inches) and the resulting aerodynamic moments were small. These delta moments are in the correct direction for change in the aerodynamic moments, but are not nearly large enough in magnitude when compared to the flight derived moments for the time after the roll moment trend reversal. To achieve the aerodynamic response observed in the flight data, more significant damage to the wing would have been required.

Based on the structural analysis, it appears feasible that a wing recession occurred and resulted in the large positive slope in the delta rolling moment. The recession was caused by severe prolonged heating internal to the left wing that melted many of the support struts. Once the struts were lost, the wing skin lost structural support, a concave cavity developed, and some lower surface tiles may have been lost.

Wind tunnel testing has shown that this type of cavity can cause the change in delta aero moments derived from the aerodynamics reconstruction in this timeframe. The aero moment change is a negative yaw moment due to increased drag and a positive roll moment due to increased lift on the left wing. This testing will be discussed in more detail in the next section.

The flash event in this timeframe could indicate a loss of either upper surface wing skin or thermal blankets or a release of molten material into the environment around the orbiter. More than 10 debris events followed and were observed by various public videos in the 8:55:04 to 8:56:00 EST (EI + 655 to 720 sec.) timeframe. Several of these events were large, consisting of a shower of particles, and lead to a brightening of the plasma trail. Another communication dropout followed at 8:56:00 EST (EI + 720 sec.).

5.4.5 Wheel Well Gas Penetration and Final Aerodynamic Events

By 8:56:16 EST (EI + 727 sec.), hot gas had penetrated the wheel well wall as indicated by off-nominal rise rates in several hydraulic line temperatures (see Figure 5-46). Preliminary analysis indicates that it is feasible to have had some gas intrusion into the wheel well area as early as 8:52:39 EST (EI + 510 sec.) since a honeycomb access panel could melt as quickly as 22 seconds after the wing spar is breached. Additionally, there are various vent paths into the wheel well around the landing gear door hinge covers.

The centerline of the plume contained enough energy to begin melting the exterior of the wheel well wall by approximately 8:54:00 EST (EI + 594 sec.). The modeling described in the previous sub-section assumed the heating equivalent of a 5 inch diameter hole in the leading edge spar, but does not include the complex thermal interaction with struts and other wing spar structure internal to the wing. The intent of the analysis is to show that it is feasible to obtain the temperature response shown in Figure 5-46, including the early response that was seen in the 8:54:10 to 8:55:10 EST (EI + 601 to 666 sec.) timeframe, when several left main gear brake line temperatures and strut actuator temperatures began an off-nominal rise.

Immediately after the wheel well wall was breached, a hot gas plume began to flow on to the left main gear strut (depicted in Figure 5-47), leading to excessive strut erosion. A wheel well wall breach in this area is consistent with the erosion pattern observed on the recovered left main gear strut. Even after damage had significantly progressed into the wheel well, the orbiter initiated the first roll reversal at 8:56:30 EST (EI+741 sec.). The maneuver was completed by 8:56:55 EST (EI+766 sec.), and the vehicle was in a normal left bank. The guid-

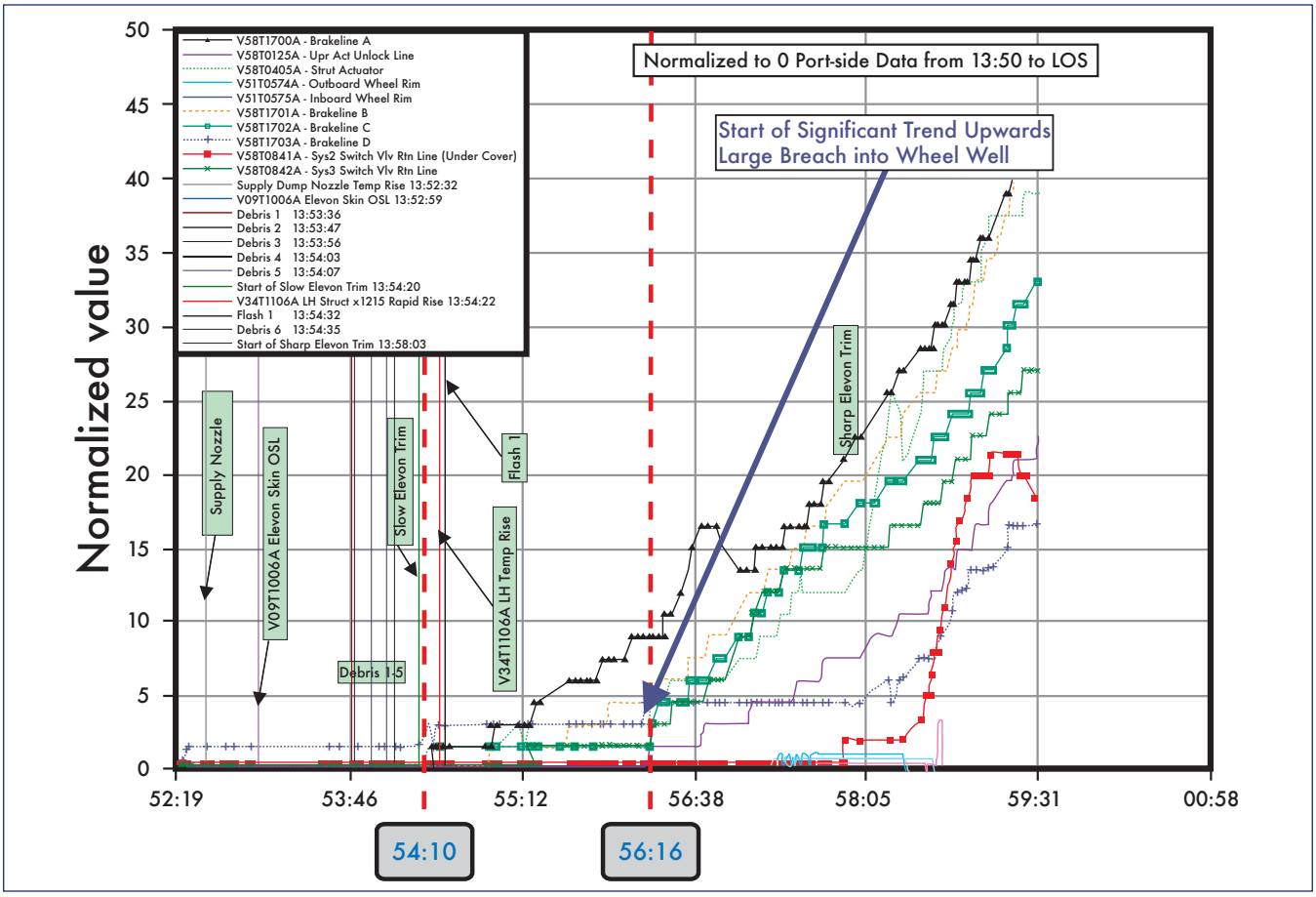

Figure 5-46. Temperature data in left wheel well trends up.

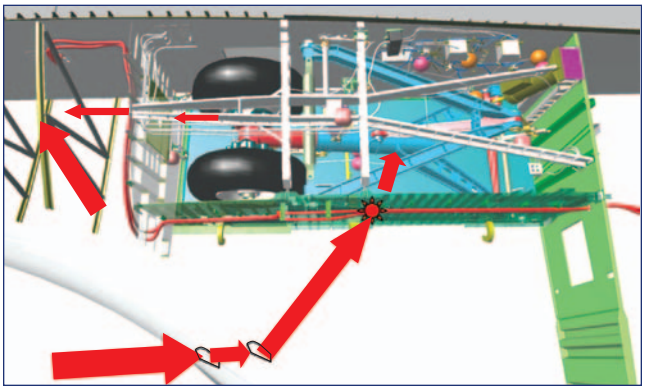

Figure 5-47. Hot gas breaches the wheel well.

ance and flight control systems were performing nominally, although the aileron trim continued to slowly change to counteract the additional drag and lift from the left wing.

Imaged at 8:57:14 EST (EI + 785 sec.), the Kirtland photo could indicate a flow disturbance on the leading edge of the left wing and/or flow leaving the leading edge of the left wing (see Figure 5-48). It also appears to show a disturbed flow leaving the trailing edge of the left wing. Other images, not shown here, also show disturbed flow on the upper side of the left wing, indicating that the damage and venting through the upper RCC vent was deflecting the flow upward. The Kirtland photo is a digital still image taken by off-duty employees of the Starfire Optical Range at Kirtland Air Force Base, New Mexico, during the STS-107 entry using a 3.5 inch telescope through a computer controlled 1 meter rotating mirror.

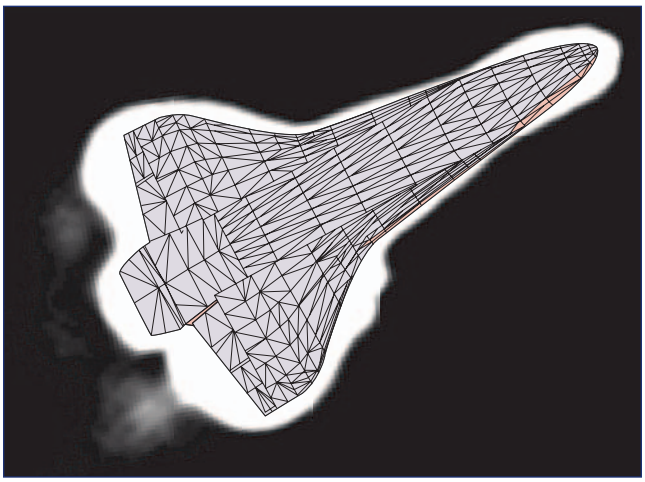

Figure 5-48. Kirtland photo with superimposed Orbiter outline.

At 8:58:32 EST (EI + 863 sec.), there was a change in stress measured on the left wing 1040 spar (main landing gear forward wall spar), as indicated by strain gauge measurements that began trending up at 8:52:18 EST (EI + 489 sec.). At 8:58:32 EST (EI + 863 sec.) the lower cap strain (near the bottom of the 1040 spar) essentially returned to a normal measurement when compared to previous flights (see previous Figure 5-39). The upper strain measurement continued to increase during this timeframe indicating that the heating was different on the upper and lower portions of the wheel well and 1040 spar. Although the response of the 1040 spar strain is not completely understood, structural analysis indicates that the strain response can be completely explained by thermal stresses caused by severe heating of the wheel well wall and internal wing components.

As shown in Figure 5-49, this strain response appears to be consistent with another sharp change in the slope of the derived delta rolling moment coefficient that occurred slightly earlier at 8:58:03 EST (EI + 834 sec.), along with several additional debris events. The vehicle responded to this event with a sharp change in the aileron trim. These events indicate that there was another significant change to the left wing configuration at this time. Wing deformation and an increase in the lower surface recession along with a loss of additional bottom tiles are possible explanations for this behavior.

At the same time as the stress was relieved on the lower 1040 spar, two left main gear outboard tire pressures began trending toward an off-scale low reading. This was preceded by a slight upward trend at 8:57:19 EST (EI + 790 sec.) for both pressure measurements. This is an indication of extreme heating of both the left outboard tire and the surrounding instrumentation. The tire has significant thermal mass and substantial heating would be required to produce the slight temperature rise. By 8:58:56 EST (EI + 887 sec.), all left main gear inboard and outboard tire pressure and wheel temperature measurements were lost indicating a rapid progression of damage or wire burning inside of the wheel well. Figure 5-38 shows the location of these pressure sensors.

At 8:59:06 EST (EI + 897 sec.), the left main gear downlocked position indicator changed state. There are indications that the gear did not come down until after Loss of Signal (LOS) because the left main gear uplock position indicator still showed the gear in the stowed position, and the left main landing gear door latch position indicator showed that the door was still closed. Additionally, there are several measurements on the strut that produce valid data until final loss of telemetry in the MCC.

As shown in Figure 5-49, there was another abrupt change in the vehicle aerodynamics caused by the continued progression of left wing damage at 8:59:26 EST (EI + 917 sec.). This change was a significant increase in the positive delta roll moment and negative delta yawing moment, indicating increased drag and lift from the left wing. *Columbia* attempted to compensate for this by firing all four right yaw jets. By this point the MCC had lost all telemetry data at 8:59:23 EST (EI + 914 sec.). Even with all four right yaw jets and a maximum rate of change of the aileron trim, *Columbia* was unable to control the side-slip angle that was slightly negative (wind on the left side of the fuselage) during much of the entry. The side-slip angle changed sign at 8:59:36 EST (EI + 927 sec.) indicating that vehicle loss of control was imminent (side-slip angle is an aerodynamics term for the angle between the relative wind velocity and the vehicle direction of motion, or velocity vector).

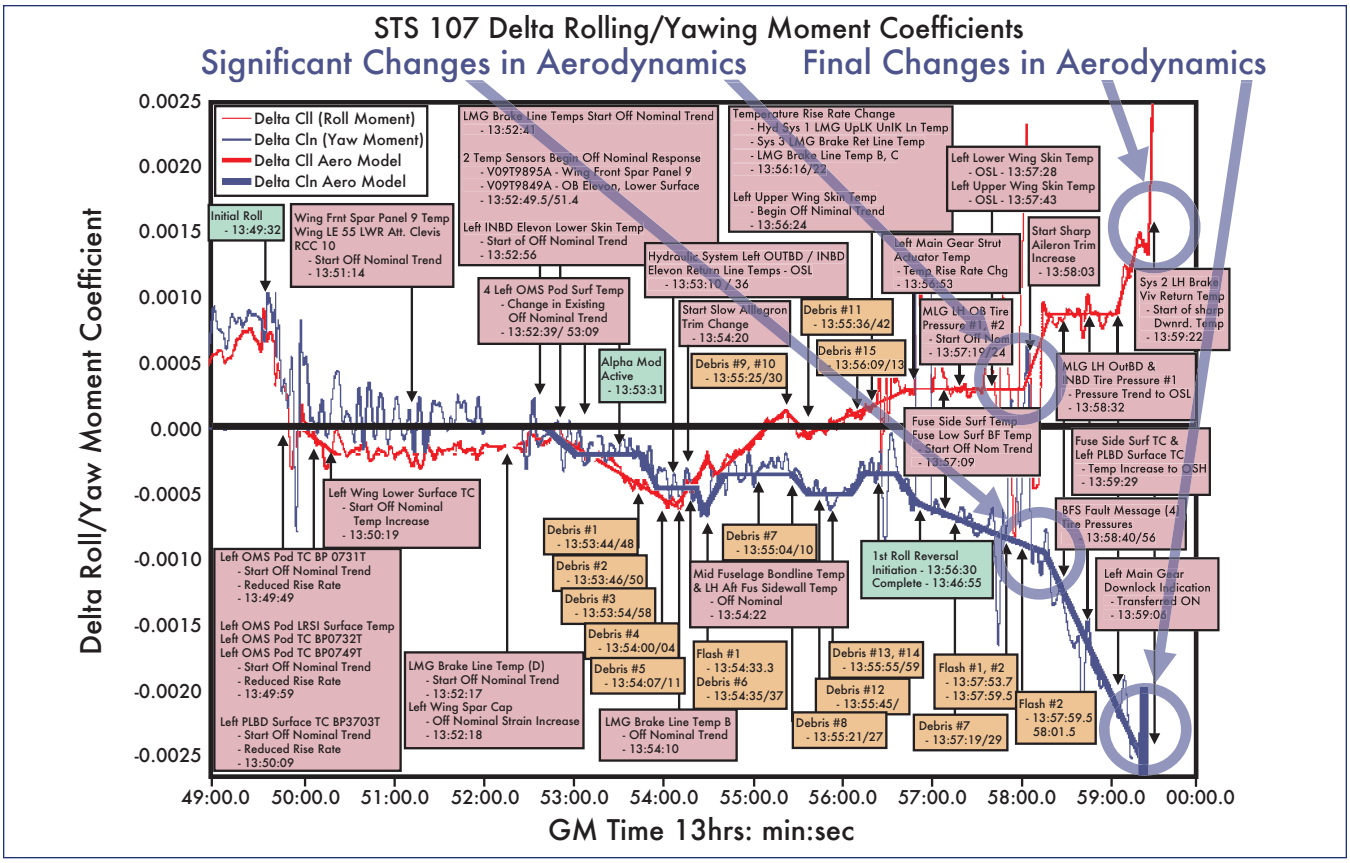

Figure 5-49. Increased wing deformation and wing recession leads to significant vehicle aerodynamic changes.

A large piece of debris was observed leaving the orbiter at approximately 8:59:46 EST (EI + 937 sec.). Five additional debris events and two flash events were observed over the next thirty seconds. MADS recorder data was lost at approximately 9:00:14 EST (EI + 965 sec.) and main vehicle aerodynamic break-up occurred at 9:00:18 EST (EI + 969 sec.), based on video imagery.

In the Mission Control Center, the Entry Flight Control Team waited for tracking data from the Eastern Range and communication link handover to the Merritt Island Launch Area (MILA) ground station. There was no radio frequency (RF) communication received from the vehicle at MILA and no valid tracking data was ever produced at the Eastern Range since the vehicle never crossed the KSC area horizon. Shortly thereafter, Mission Control's Entry Flight Director implemented contingency action procedures.

5.5 Aerodynamic Reconstruction

As previously discussed, the flight-derived aerodynamic moments use the high altitude winds and atmosphere developed by the DAO and represent the most accurate reconstruction that is possible based on available data. Many different scenarios were proposed to define the damage necessary to match this reconstruction using wind tunnel testing and CFD analyses at facilities across the United States. These scenarios include individual and multiple full or partial missing RCC panels, a missing landing gear door, a deployed left main landing gear, missing lower surface tiles, holes through the wing, lower surface deformation, and several others. The details for all of the options that did not match the flight-derived data will not be discussed here and are beyond the scope of this document.

Figures 5-50 through 5-52 show the flight derived delta roll, yaw, and pitch aerodynamic moments, respectively, along with the tested damaged configuration results that are consistent with the flight data. The intent of the remainder of this

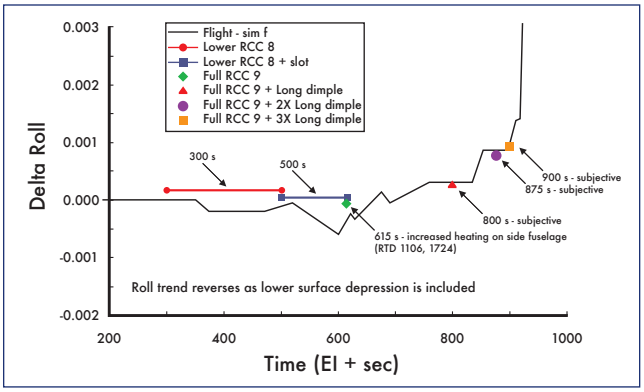

Figure 5-50. Wind tunnel testing configurations that match delta roll moment data.

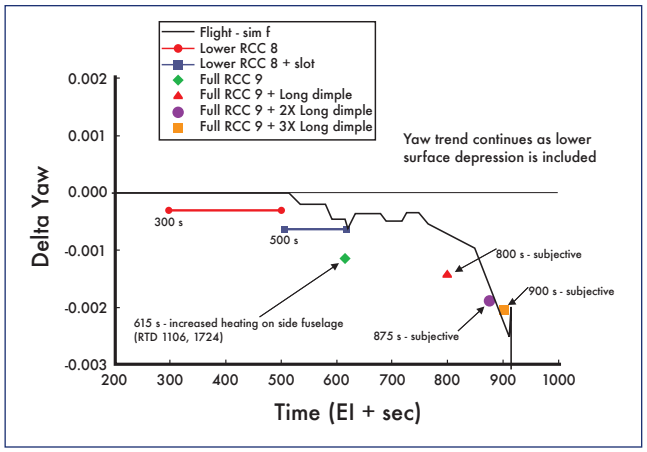

Figure 5-51. Wind tunnel configurations that match delta yaw moment data.

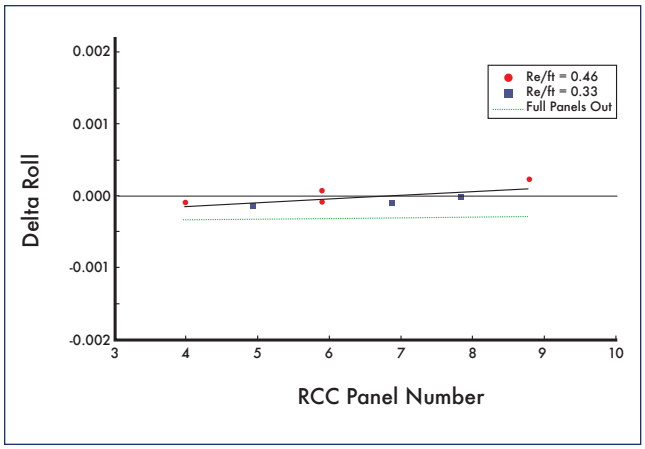

Figure 5-53. Delta roll for lower half and full panel RCC panel missing.

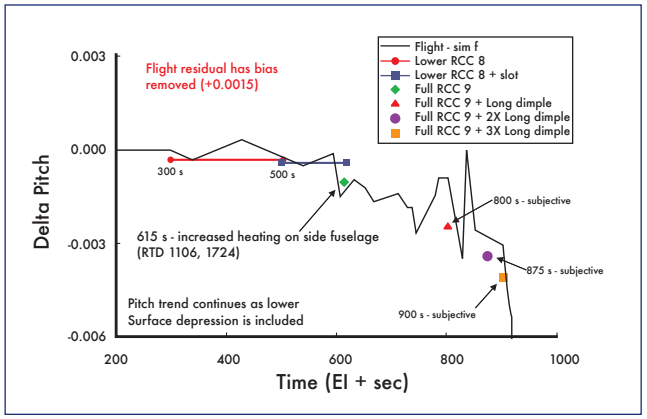

Figure 5-52. Wind tunnel configurations that match delta pitch moment data.

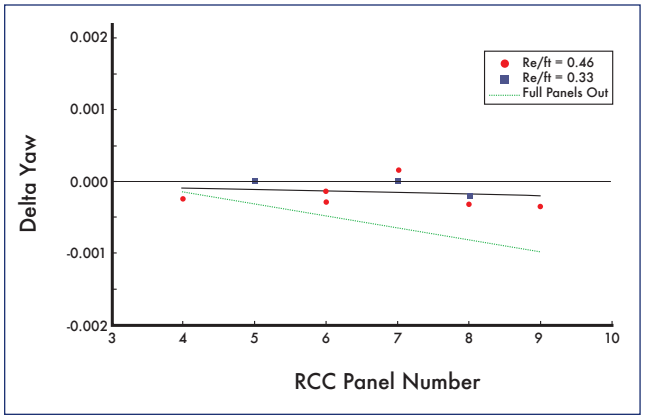

Figure 5-54. Delta yaw for lower half and full panel RCC panel missing.

section is to briefly discuss the CFD analysis and wind tunnel testing used to replicate the derived delta aero moments. Note the time scale on these plots is in seconds from EI.

As discussed previously, the reconstructed aerodynamic moments showed little to no change due to damage through 8:52:29 EST (EI + 500 sec.). Based on the forensics data discussed in Section 5.3, the most likely region of initial damage was in the lower part of RCC panel 8. Wind tunnel testing in the Langley Research Center (LaRC) CF4 tunnel indicated that a missing bottom part of RCC panel 8 (from the apex to the lower carrier panel) matches the initial aerodynamic increments, which show a minimal effect on the overall vehicle aerodynamics. In fact, even a full missing panel 8 produces only a small change to the roll and yaw aero moments. Figure 5-53 and Figure 5-54 show the results of this LaRC evaluation.

The left wing spar was breached in the 8:51:14 EST (EI + 425 sec.) to 8:52:15 EST (EI + 487 sec.) timeframe. Initially, the spar breach had little to no effect on the derived aero moments. Over time the leading edge damage progressed and a slot or upward deflection of the flow through the upper carrier panel 8 developed. The combination of flow through the wing leading edge and flow through a slot onto the upper carrier panel is consistent with the first observed aerodynamic response, which occurs at 8:52:29 EST (EI + 500 sec.). This can be observed in Figure 5-50 and Figure 5-51 as a slow negative trend in delta roll and yaw. Figure 5-55 shows the wind tunnel test results for three different cases: missing lower RCC panel 8, missing panel 8 combined with a 4 inch diameter hole in the upper carrier panel 8, and missing RCC panel 8 with a slot through the upper carrier panel. The slot was shown to produce the increased delta yaw observed during flight as well as the upper surface flow disturbances on the OMS pod and left side fuselage, which were also observed during flight by abnormal temperature rise rates.

It is possible that a hole through the upper wing developed in the 8:54:11 EST (EI + 600 sec.) to 8:54:31 EST (EI + 630 sec.) timeframe. This is consistent with a lull in the measurement failure rate in the wire bundle along the wheel well that was discussed earlier in Section 5.4.3. Wind tunnel testing and CFD analysis have shown that sizable holes through the wing have little to no effect on the aerodynamics and heating on the left side of the fuselage and OMS pod. A representative sample of this work is shown in Figure 5-55 as damage scenario number 2.

The next significant aerodynamic event occurred at 8:54:11 EST (EI + 602 sec.) when a dramatic reversal of the aero rolling moment trend occurs. By this time hot gas and an internal plume environment had severely degraded the structural integrity of some of the intermediate wing support structure leading to wing deformation. Three different configurations were tested to validate the theory of wing deformation. The first involved global wing deflection of up to 0.79 inches due to damage and is depicted in Figure 5-56. CFD analysis of this configuration showed extremely small aero moment response for yaw and roll that does not match the flight derived data. More substantial local wing skin deformation with a maximum deflection of 5.1 inches due to three ribs missing along with other internal wing damage was examined using CFD tools. Again, these results produced only small aerodynamic moment changes, which did not match the flight-derived data.

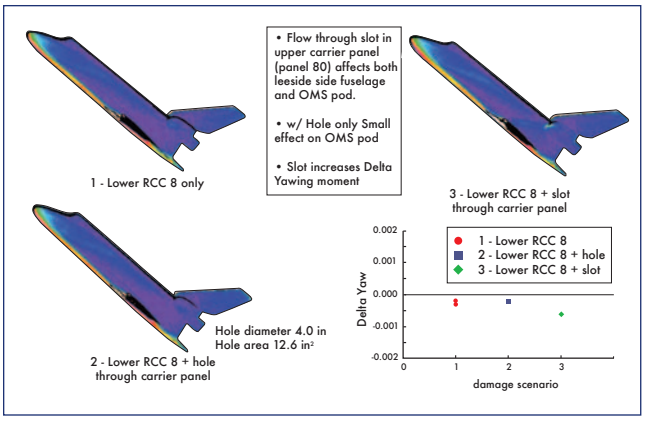

Figure 5-55. Wind tunnel testing results for missing lower carrier panel 8 and a slot and hole through wing.

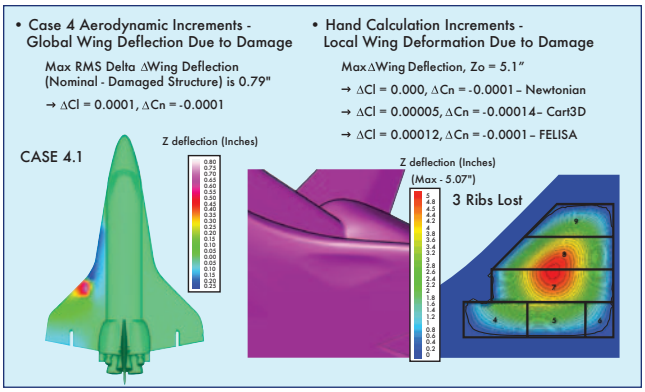

Figure 5-56. CFD analysis of wing deformation.

The third and final configuration that was tested was a depression in the lower surface of the wing caused by the significant structural damage caused by the hot gas plume environment internal to the wing. A previous section (5.4.5) discussed the internal structural damage that was most probable in this timeframe. LaRC wind tunnel testing and CFD analysis were performed for several different configurations of lower surface recessions shown in Figure 5-57. The data shows that it is feasible for a recession to cause the change in the rolling moment sign when combined with some portion of RCC panel 9 missing at 8:54:11 EST (EI + 602 sec.).

Initially, the recessed area would have been relatively small; however, it would gradually grow over time to cause the delta roll moment to increase. By 8:57:29 EST (EI + 800 sec.) wind tunnel testing showed that the depression has to be on the order of 20 feet long, two feet wide, and 5.3 inches deep along with panel 9 missing in order to duplicate the delta roll coefficient shown in Figure 5-50. This configuration provides a delta yaw moment that is slightly larger than was observed, but is consistent with a decreasing negative delta yaw moment observed in this timeframe (Figure 5-51).

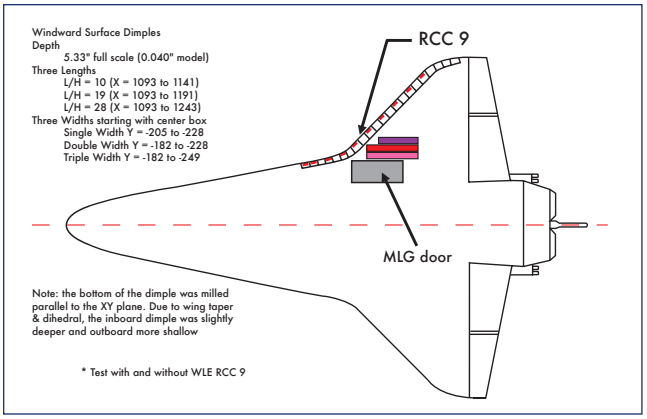

Figure 5-57. LaRC wind tunnel testing of lower surface depressions.

A little more than a minute later, at 8:58:44 EST (EI + 875 sec.), the width of this recession would need to have increased by another two feet to match the aerodynamic delta roll and yaw moments. At this point, the rate of change of the aerodynamic moments and damage progression is so great that it likely grew by about an additional two feet in width over the next 25 seconds at 8:59:09 EST (EI + 900 sec.). Additionally, the delta pitch moment was now observed to deviate from previous mission reconstructions in this timeframe. Figure 5-52 shows that the recession concept is consistent with the delta pitch moment reconstruction. Previous structural analysis indicates that by 8:58:19 EST (EI + 850 sec.) there is large-scale wing deformation and thus the possibility of a large recession is plausible in this timeframe.

In summary, the latest aerodynamic wind tunnel testing and CFD analysis performed to date indicate that the initial damage was probably relatively small, like a hole and/or missing part of the bottom of RCC panel 8. A slot then developed so that there is upward flow through the RCC vent and across the upper 8 carrier panel. Later, more of RCC panel 8 and/or panel 9 is lost along with some substantial wing deformation probably involving a locally depressed area on the lower wing surface. The wing deformation and lower surface recession gradually increased over time, and eventually the yaw and roll moments were too great for the flight control system to manage, leading to a loss of vehicle control and aerodynamic break-up.

Although this aerodynamic reconstruction represents a reasonable sequence of vehicle configurations that led to loss of control during entry, it is not meant to be interpreted as an exact literal sequence of events. The wind tunnel testing and analysis was performed using representative geometries; however, the actual specific vehicle damage is unknown and may never be known completely. The sequence of events discussed here is consistent with the reconstructed aero moments, MADS data, and forensics data and provides the best aerodynamic, thermal, and structural understanding possible for the eventual loss of *Columbia*.

6.0 Re-usable Solid Rocket Motor

All Re-usable Solid Rocket Motor (RSRM) investigation fault tree legs have been closed for the STS-107 RSRM set, RSRM-88. All Contract End Item (CEI) performance specifications were met including all flight individual and paired motor requirements. Postflight inspections revealed a tear in the right-hand nozzle flex boot that is considered an IFA (STS-107-M-01), but the tear is attributed to thrust tail-off or splashdown events. A slightly low out-of-family thrust level was observed for the right-hand motor in the 113.5 to 114.5 second interval during thrust tail-off, but the resultant thrust imbalance was still within family experience and CEI limits. The new experience has been reviewed and accepted as being within the statistical expectations for the RSRM motor population and is attributed to the increased population sample size (see Section 3.4 for more details).

7.0 Solid Rocket Booster

The Solid Rocket Booster (SRB) fault tree for the STS-107 SRB set, SRB BI116, remains open due to possible debris sources at the forward SRB/External Tank (ET) separation bolt catcher assembly and the forward Booster Separation Motors (BSM). The STS-107 SRBs performed nominally and there were no reported SRB IFAs.

Four blocks on the STS-107 SRB fault tree remain open pending completion of forward bolt catcher testing. The bolt catcher, shown in Figure 7-1, was not qualified as an assembly, and structural qualification testing was not representative of the current flight configuration. The exact magnitude of loads transmitted to the bolt catcher housing cannot be determined based on available data. The SLA-561 thermal protection system (TPS) material on the bolt catcher was qualified by test and analysis for general ET application, but no pyrotechnic shock testing was performed. There is no test data available on the bolt catcher honeycomb dynamic crush strength versus separation bolt velocity, and random pressure loading from the NASA Standard Initiator (NSI) ejection was not included in the original qualification tests. Lastly, the running torque/break-away torque was not measured during STS-107 bolt catcher fastener and ET range safety system (RSS) fairing installation, which is used to verify the insert locking feature is in place. A review has determined that the bolt catchers and RSS fairings were installed and secured for flight with the correct bolts and final torque. Testing is in work to close the four remaining fault tree blocks, but initial static tests results show failure below the required safety factor of 1.4.

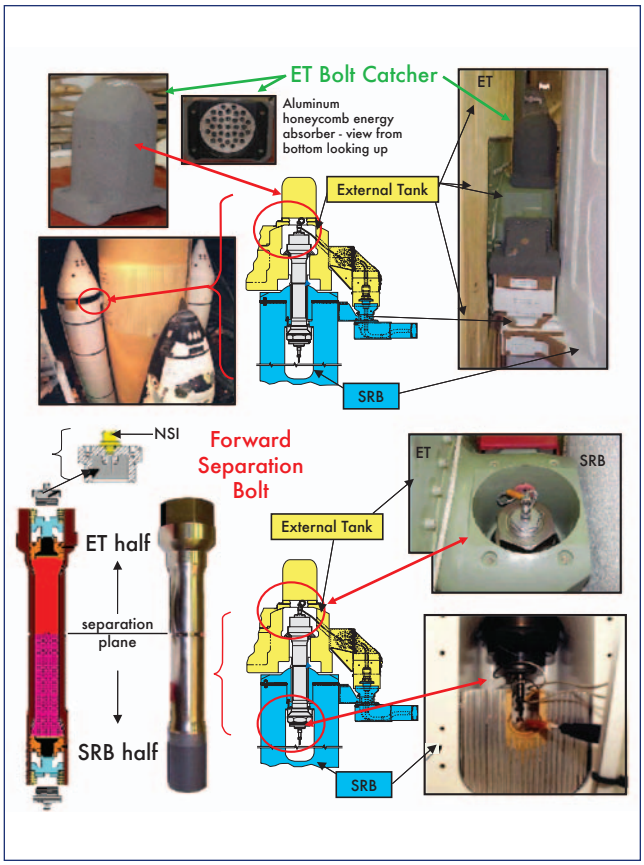

Figure 7-1. Details of SRB/ET forward separation bolt catcher assembly.

Two other blocks on the STS-107 SRB fault tree remain open that pertain to potential debris from the forward BSMs. Inspection of the forward BSMs found no indication of unburned propellant or any indication that the BSMs contained any Foreign Object Debris (FOD). The two debris related fault tree blocks will remain open pending transport and impact analysis.

8.0 Space Shuttle Main Engine

All Space Shuttle Main Engine (SSME) investigation fault tree legs have been closed. The STS-107 Block II SSMEs (center #2055, left #2053, and right #2049) performed nominally and there were no reported SSME In-Flight Anomalies (IFAs).

9.0 Environmental Factors

9.1 Introduction

A survey was conducted of the relevant environmental factors during STS-107/ET-93 processing to determine if a correlation could be drawn between those factors and ET bipod foam loss observed in flight. The data are inconclusive as to whether any correlation can be shown between environmental factors and ET bipod foam loss. The review considered ET age and exposure time, as well as weather factors such as rainfall, temperature, and humidity.

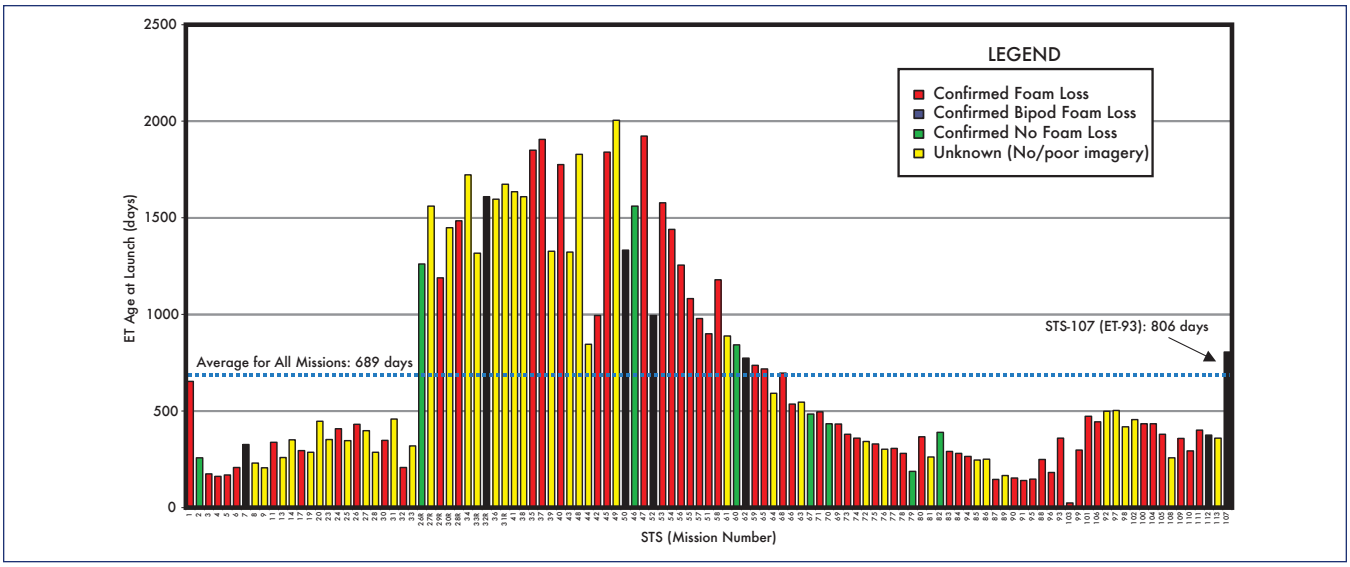

Figure 9-1. ET age for all STS missions.

9.2 Age and Exposure

The ET age was compared for various flights, presented in Figure 9-1. As shown in Figure 9-2, the ET age for STS-107/ET-93, 806 days, falls above the 95% confidence interval upper limit for the average age of all tanks, mean value 689 days, as well as the average age for all tanks with known bipod foam loss. STS-107/ET-93 also falls within the 95% confidence limit for missions with known bipod foam loss. Although the upper bound of the 95% confidence interval of the age of missions with bipod foam loss appears to be greater than the other groups in Figure 9-2, the 95% confidence interval limits of the different groups overlap each other. Therefore, data are inconclusive as to whether a correlation can be drawn about ET age and bipod foam loss.

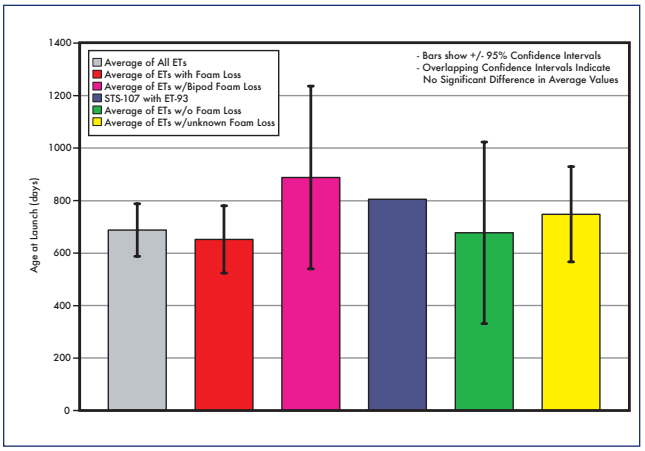

Figure 9-2. ET age for STS-107 compared to ET age for missions with and without bipod foam loss.

A similar comparison was made relating ET exposure time and bipod foam loss across the flight history (see Figure 9-3).

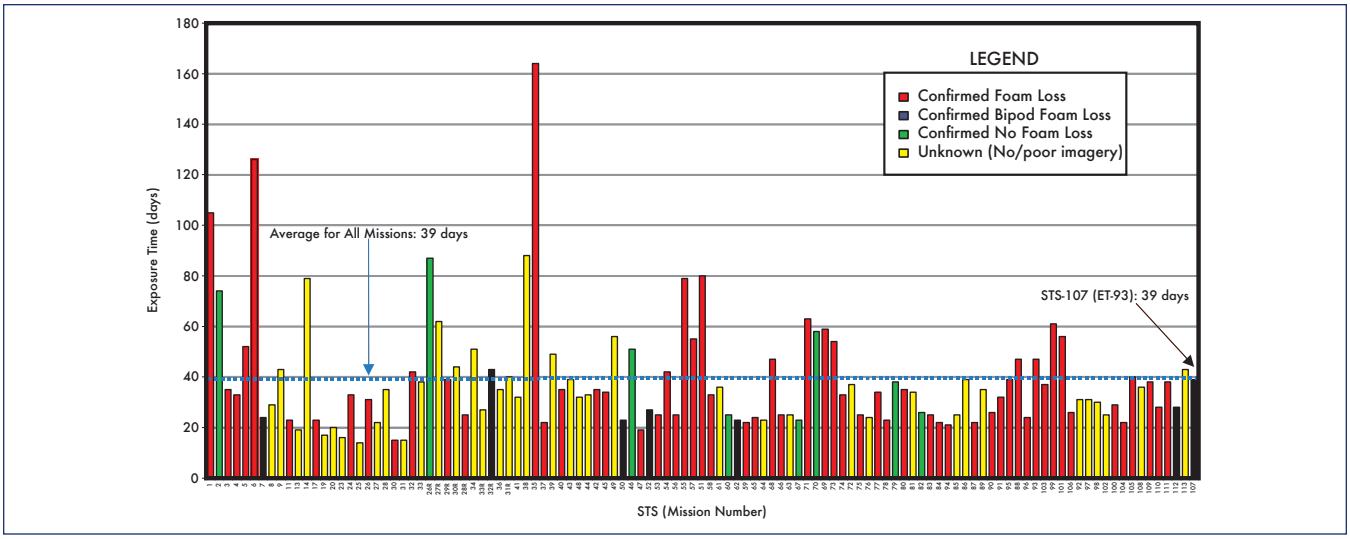

Figure 9-3. ET exposure time (to weather) prelaunch for all STS missions.

Note that the STS-107/ET-93 exposure time, 39 days, is the same as the mean value for all STS flights. As shown in Figure 9-4, the STS-107/ET-93 exposure time falls within the 95% confidence limit of all missions' ET exposure time, as well as the time confidence limits for flights with or without known bipod foam loss. The STS-107/ET-93 exposure time is larger than the 95% confidence upper bound for missions with known bipod foam loss. However, as stated above when discussing ET age, the 95% confidence limits of the different groups in Figure 9-4 overlap each other, and data are inconclusive as to whether ET exposure time and bipod foam loss can be correlated.

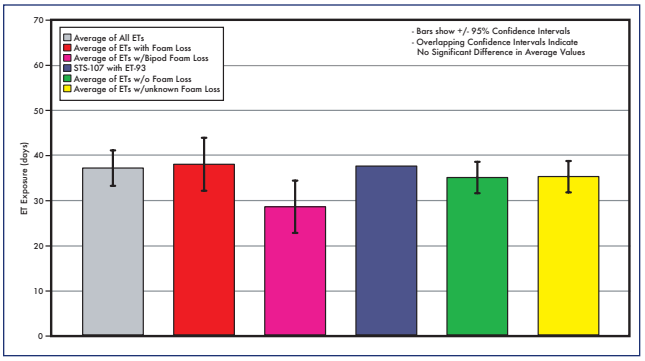

Figure 9-4. ET exposure time (to weather) for STS-107 compared to ET exposure time for missions with and without bipod foam loss.

9.3 Weather Factors

An extensive review of the relevant weather at Kennedy Space Center (KSC) was conducted in order to determine if a correlation could be derived for the weather conditions impact on ET bipod foam loss. The precipitation review examined total rainfall, maximum one-day rainfall, average daily rainfall, launch day rainfall, and L-5 days through lift-off total rainfall. Figure 9-5 shows the total prelaunch rainfall for all STS missions. As shown in Figure 9-6, although the STS-107 value for total prelaunch rainfall, 12.78 inches, is greater than the mean value for all mission, 5.45 inches, the data are inconclusive as to whether a correlation can be

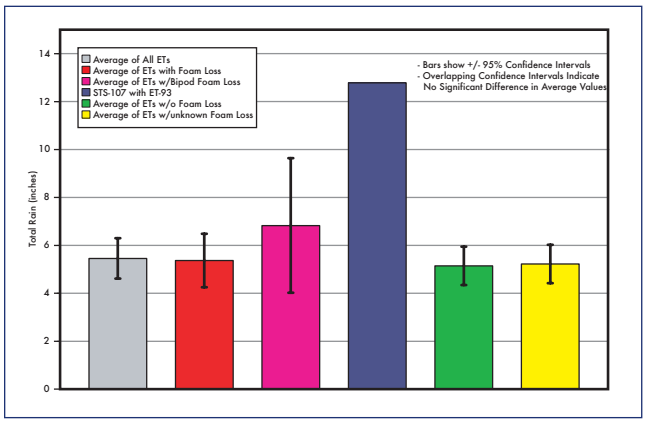

Figure 9-6. Total rainfall for STS-107 compared to total rainfall for missions with and without bipod foam loss.

made for ET bipod foam loss as a function of total rainfall prelaunch. The 95% confidence limit of the missions with ET bipod foam loss overlaps the confidence interval for all missions, as well as missions with no foam loss.

Similarly, the other rainfall parameters studied (e.g., average daily, day-of-launch) reveal no correlations for ET bipod foam loss. Figure 9-7 and Figure 9-8 show the data correlation for average daily prelaunch rainfall. The STS-

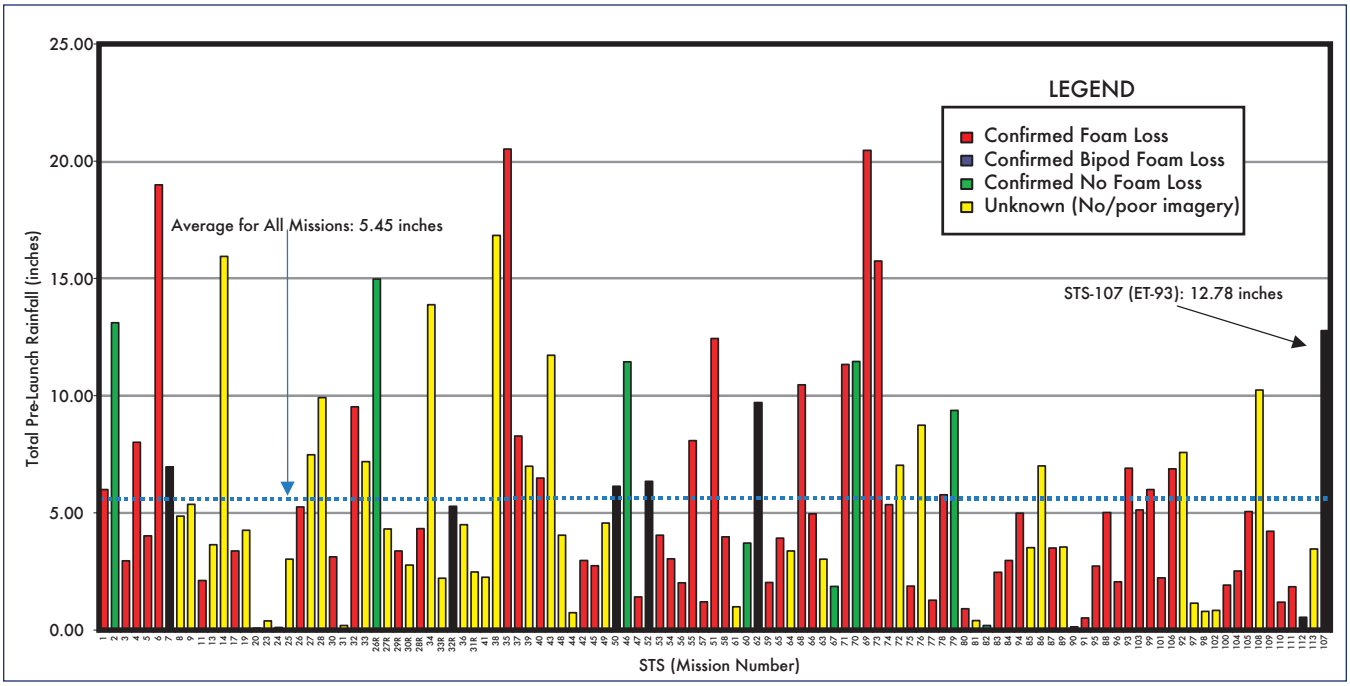

Figure 9-5. Total prelaunch rainfall for all STS missions.

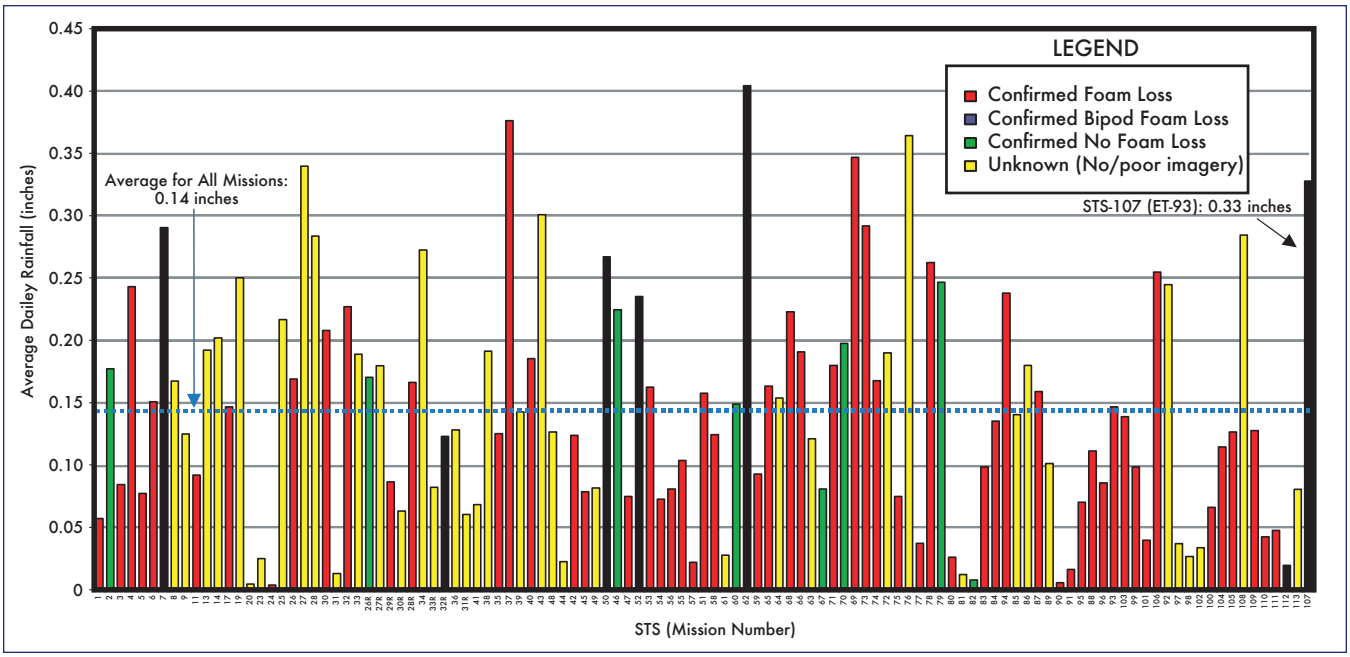

Figure 9-7. Average daily rainfall prelaunch for all STS missions (above).
Figure 9-8. Average daily rainfall prelaunch for STS-107 compared to average daily rainfall for missions with and without bipod foam loss (below).
Figure 9-9. Day-of-launch average temperature for all STS missions (bottom).

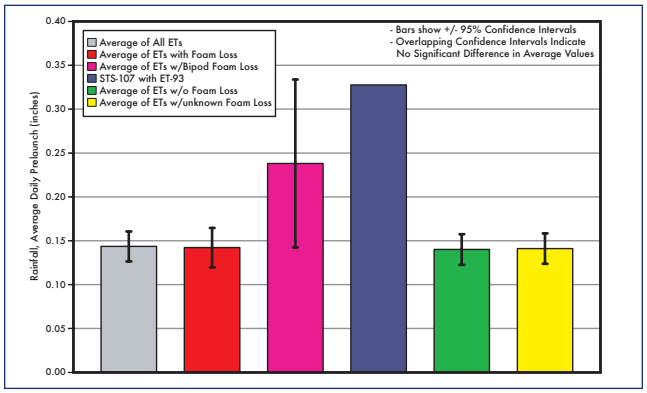

107 value, 0.33 inches, and the mean value for missions with bipod foam loss are greater than the average mission value, 0.14 inches. However, the confidence intervals overlap each other, and the data are inconclusive as to whether average daily rainfall and ET bipod foam loss can be correlated.

In addition to rainfall, the study also reviewed average, minimum, and maximum temperature, dew point, and humidity for both prelaunch and day of launch. Figure 9-9 shows the day-of-launch average temperature. The STS-107 day-of-launch average temperature, 58 °F, was less than the mean value for all missions, 71 °F, but no correlation can be made between day-of-launch average temperature and ET bipod

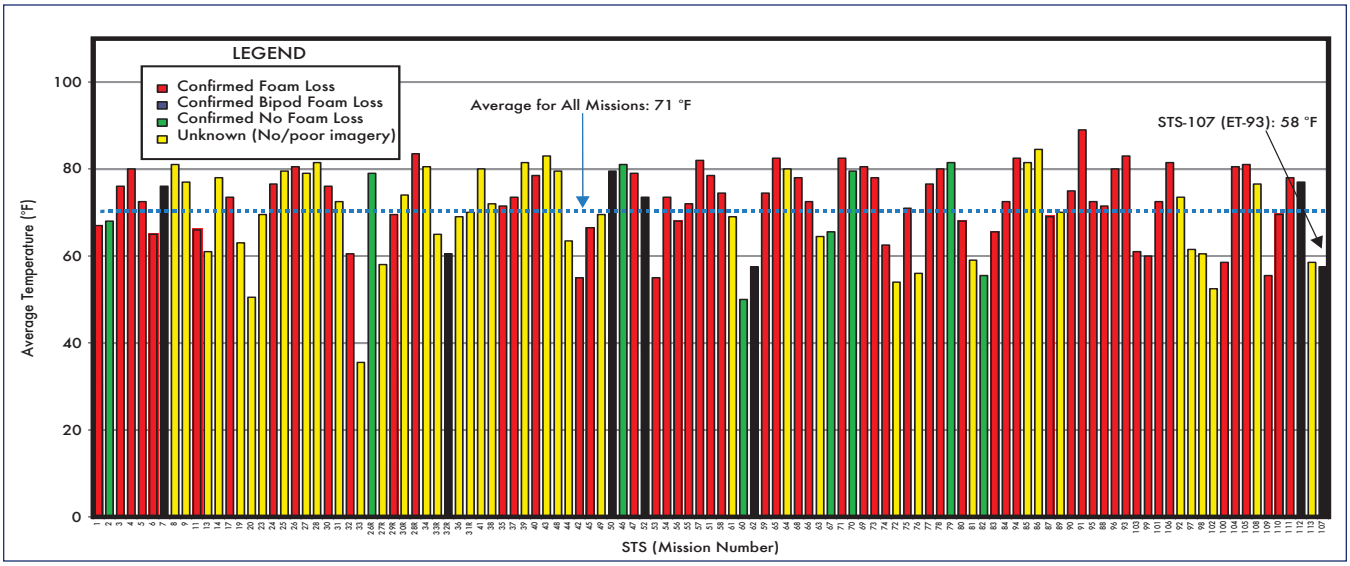

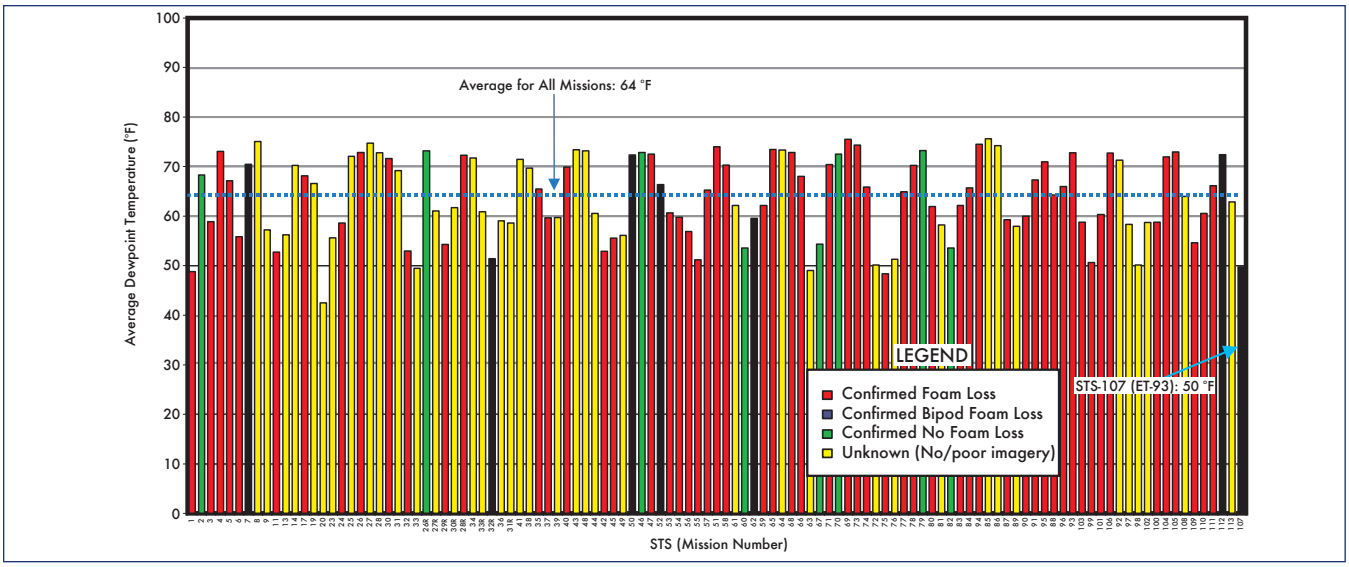

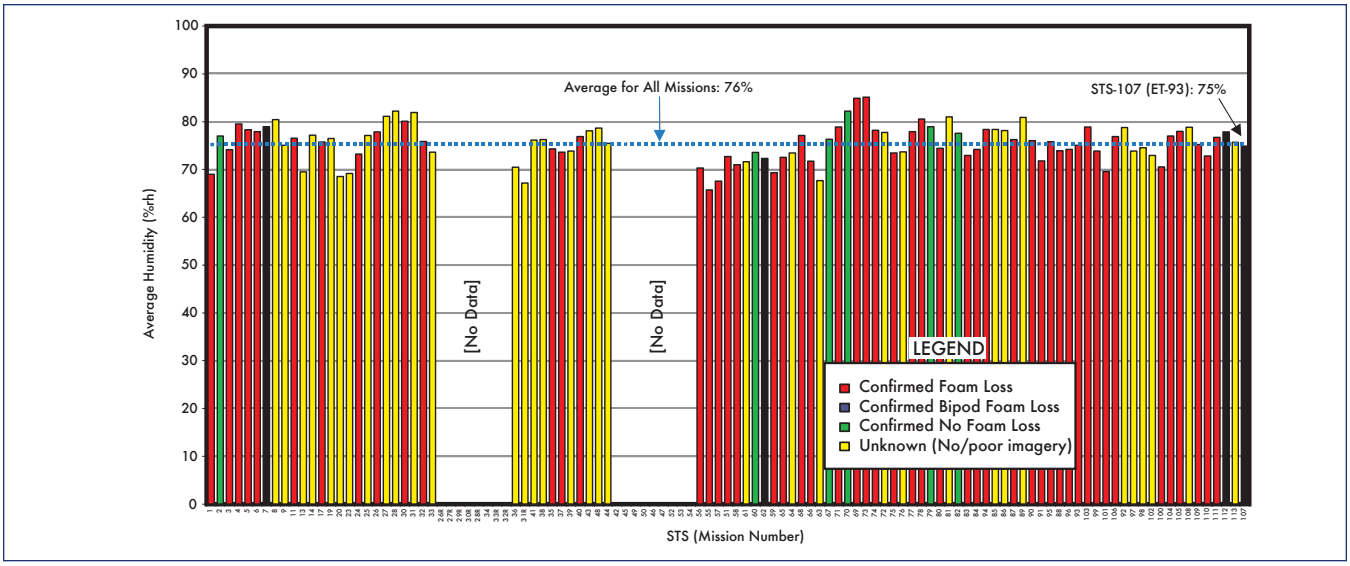

Figure 9-10. Prelaunch average dewpoint for all STS missions (top).
Figure 9-11. Prelaunch average humidity for all STS missions (above).

foam loss. Similar comparisons made for other temperature samplings, dew point (Figure 9-10), and humidity (Figure 9-11), yielded no correlations either.

10.0 Left Wing Processing and RCC Design

10.1 Introduction

This section summarizes the processing effort performed on the left wing of the Space Shuttle *Columbia* from the last Orbiter Major Maintenance (OMM) period through the launch of STS-107, and provides some background on the design of the RCC panels used on the orbiter. The processing includes all work done on *Columbia* from the major maintenance period (*Columbia* J3-OMM) through the flight of the STS-109 mission and all the normal preflight work done in preparation for the STS-107 mission.

10.2 Left Wing Processing (Palmdale, J3-OMM)

Columbia was in Palmdale, California, for its most recent OMM from September 1999 through March 2001. The work performed on the left wing included work on the electrical power and distribution system, instrumentation, mechanisms, structures, and the Thermal Protection System (TPS). There were 29 Problem Reports (PRs) on the electrical system, mostly wire lead discrepancies and wire stow issues. Two pyrotechnic connectors were found out of configuration and repaired. Instrumentation sensors and wire splices accounted for 20 PRs on the left wing and all were appropriately resolved. In the mechanisms area, a main landing gear door rotational pin inspection was partially performed at Palmdale and subsequently completed at the KSC. Slight damage to the Chromium plating of the forward inboard gear door hook was repaired. The gear downlock bungee was sent to the vendor for refurbishment.

Palmdale logged 62 PRs to the left wing structure that addressed elevon cove corrosion, elevon flipper door modification (material change from Inconel to Aluminum), and minor work on the main landing gear door.

All Reinforced Carbon-Carbon (RCC) upper and lower wing Leading Edge Structural Subsystem (LESS) access panels, spar insulators, ear muff insulators, wing leading edge RCC panels, and spar fittings (see Figure 10-1 and Figure 10-2) were removed and inspected for discoloration and damage. Visual pinhole inspections were performed on each RCC panel and the wing leading edge spar was inspected for damage. Oversized pinholes were originally reported in RCC panels 8 and 19, but after further evaluation with an optical comparator, it was determined that the pinholes were acceptable. No other significant damage was noted. Leading edge RCC panels 6 and 13 through 17 were sent to the vendor (Vought) for refurbishment. New shims were installed to accommodate the reinstallation of the spar insulators.

The panels and spar fittings were reinstalled and all step and gap measurements were taken. At that time, gaps were found to be unacceptable in numerous locations. Wing leading edge RCC panels 11, 12, 17, and 18 were removed and additional anomalies were noted, which included insufficient step and gap, spar fitting shims not per design (too small), and the lower access panel nutplates debonded and/or with low running torque. The low torque was due to a combination of the shim problem and a procedural error on the torque sequence. All 22 RCC panels were removed a second time. The nutplate issues were resolved by removing and replacing the nutplates that were accessible and securing with safety wire those that were not accessible. All anomalies identified were repaired, reworked, or accepted by Material Review (MR).

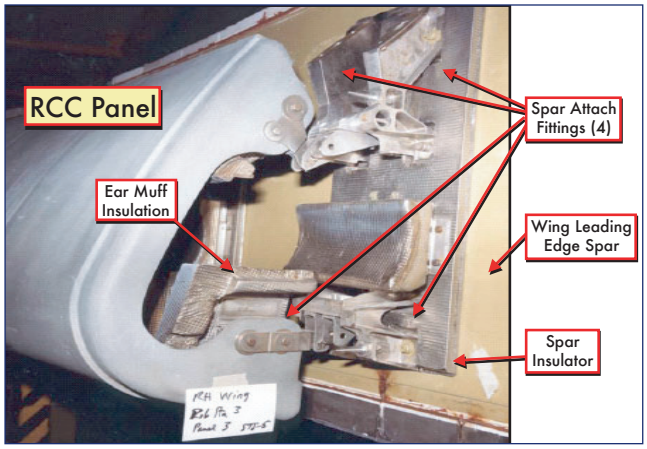

Figure 10-1. RCC components.

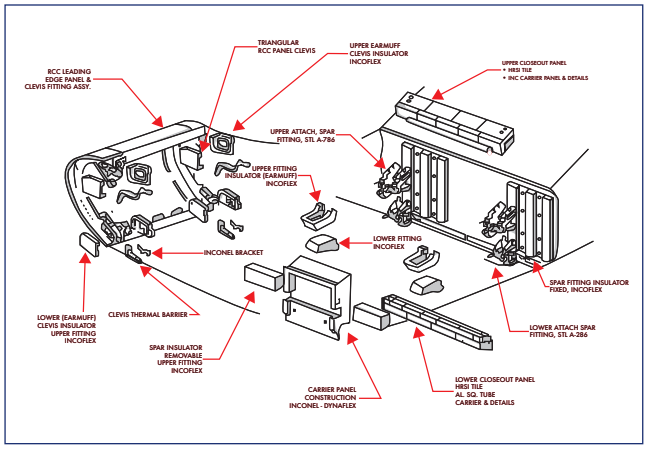

Figure 10-2. RCC panel assembly.

Tiles are attached to a strain isolation pad and then to the orbiter structure by a Room Temperature Vulcanized (RTV) adhesive. The outer tile surfaces must be flush with one another to preclude steps that would lead to excessive heat damage of surrounding tiles due to aerodynamic heating (Figure 10-3). Gaps present between adjacent tiles must be adequately sealed. There were 200 tile PRs worked for step and gap, gap fillers, and repair on the elevon cove area tile. One hundred thirty one (131) upper and lower wing surface tiles were replaced for various reasons, including baseline removal and replacements, damaged tile, instrumentation problems, and structural inspections. Wear and tear accounted for 27 maintenance items. Tile gap filler replacements numbered 58 with no issues noted. There were 100 discrepancy reports for minor tile putty repairs. Six chits (change items) were worked on the left side, mostly in the landing gear area. The main landing gear rotational pins, wheel well wire, and landing gear structural components were all inspected. The left inboard brake interference was slightly out of tolerance, but was corrected. One chit addressed the application of corrosion protection coating to the forward wing spar.

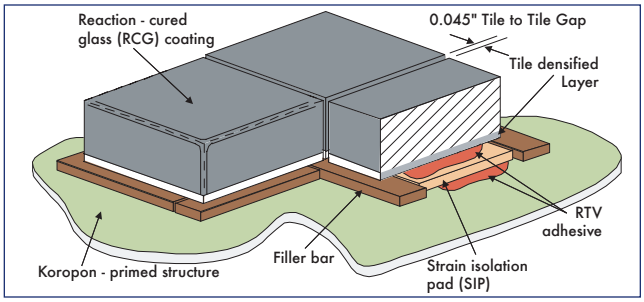

Figure 10-3. Typical tile installation.

Twenty Master Change Records were incorporated during the period. They included the replacement of the aluminized Mylar tape that lines the wheel well walls, the deletion of some non-functional acoustic sensors, and the removal of inactive Modular Auxiliary Data System (MADS) instrumentation. An additional part of that effort was the modification of the elevon columbium seal springs, some wing leading edge protective shielding, and enhancements to various gap fillers.

The 22 left wing Line Replaceable Units (LRUs) that were replaced included the RCC panels previously mentioned, a hydraulic retract valve, the landing gear extend isolation valve, left main landing gear bungee, Tee seals, and an Inconel (Incoflex) insulator.

All items not completed at Palmdale were dispositioned and transferred to KSC for completion.

10.3 Left Wing Processing (STS-109)

Once *Columbia* was delivered to KSC in March 2001, the outstanding main landing gear work was completed. This work included the left inboard axle rework to improve brake clearance and the completion of the rotational pin inspections. The elevon flipper doors had a few PRs for Wear and Tear issues that were resolved. The lower elevon cove columbium seals/springs were out of configuration as compared to drawing requirements, and minor adjustments were successfully made. When it was discovered that there was excessive corrosion protection coating applied to the elevon cove area, work was done to clean that area. There was minor corrosion in the elevon cove area that was removed as well.

There were also numerous tile inspections and verifications performed during the processing flow for STS-109. No work was done on the wing leading edge RCC panels or Tee seals after *Columbia* returned from OMM and prior to STS-109. During that flow work was done on the LESS lower access panels 3, 6, 15, 17, 21, and 22 for step and gap issues and frayed horse collar gap concerns. Upper access panel 14 was replaced due to out-of-tolerance gap and out-of-tolerance Strain Isolation Pad (SIP). No lower tile acreage was replaced during the STS-109 flow, but the upper wing area had a few minor repair areas. All the leading edge and trailing edge panels for the left inboard elevon cove were replaced. Discrepancies were noted at Palmdale and corrected at KSC for the primary and secondary sealing circuits in the elevon cove seal assembly. The seals were operating within acceptable limits, but work was performed to repair leak paths and improve flow rate. There were 1,481 tiles that were suspect and had a manual deflection test performed on them in support of the corrective action required after one wing lower surface tile was found missing/debonded after the STS-103 (orbiter *Discovery*) mission. Thirteen thermal barriers were replaced in the main landing gear door area. There were 14 total MR items for STS-109.

10.4 Left Wing Processing (STS-107)

During the STS-107 flow, damage was noted to the left main landing gear axle sleeve and axle nut. A review of the entire shuttle fleet revealed similar conditions on other vehicles. The tire separation harness for the tire temperature and pressure measurements was found caught in the brake mechanism and had to be removed. The tires were deflated and removed in order to inspect the wheel half-tie bolts. Due to the discovery of corrosion in the tie bolt holes in wheels throughout the fleet, wheels with sleeved tie bolt holes were installed.

The angle seal at RCC panel 1 on the left wing leading edge (see Figure 10-4) was removed to support the evaluation of the horse collar gap filler between the adjacent tiles. During the removal attempt, the upper bushing remained bound with the shipside clevis. During subsequent attempts, the angle seal was manually manipulated to try and remove the preload. During the KSC paper review, structures engineers realized that the load applied to the angle seal was specified to be kept below 20 pounds, but was never recorded in the

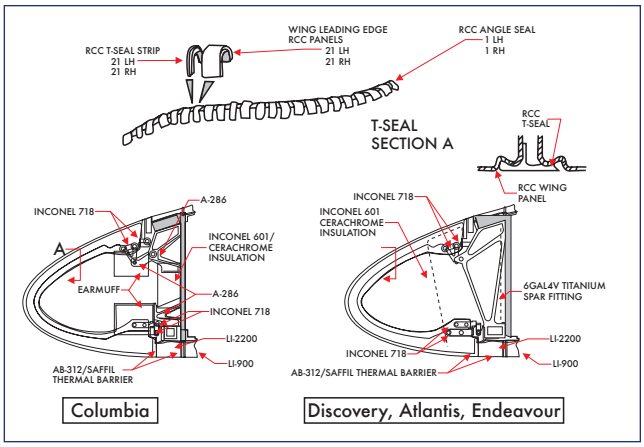

Figure 10-4. Wing leading edge RCC.

paper. The RCC specification requires that RCC panel loads be kept below 30 pounds. Subsequent tests at KSC verified that the angle seal load was below the 30-pound requirement. The LESS prevention and resolution team is addressing the issue of how to measure the load and how to support the seal in future operations. Work continued on the elevon flipper doors. Flipper door 1 blade seal was not making contact with the rub channel, potentially leading to excessive venting from the elevon cove area. This issue surfaced twice during this flow and was Material Review (MR) accepted to fly as is. Modification was made to the Inconel trailing edge seal and bulb seal on the elevon. Additional work was performed on the elevon cove corrosion protection again to reduce the excessiveness of the application.

An uncharacteristic number of access panels were removed during the STS-107 processing flow. Most of the upper (14 of 22) and lower (13 of 22) access panels were removed due to misinterpreted requirements to check for excessive movement in the panels. Wing leading edge upper and lower access panels at RCC 15 had to be removed to retrieve a burned ball of tape that had been inadvertently left from previous work performed during OMM. Upper access panel 18 was removed to investigate the possibility of water intrusion from a water deluge system mishap in the orbiter processing facility, but no damage was noted. Tee seal 10 was removed and shipped to the vendor for repair. No other wing leading edge RCC panels were removed in preparation for the STS-107 mission. Only one access panel was replaced on the left outboard elevon cove area, but there were three other minor tile repairs performed on the left elevons. There were four tiles replaced on the under side of the left wing in front of the left outboard elevon because a gap filler had protruded 0.8 inches. This caused charred filler bar, SIP damage, and instrumentation wiring damage. None of the tiles in these areas is believed to affect the failure scenario. There were 36 total MRs for STS-107.

10.5 RCC Design

The RCC material is the basic structure of the wing leading edge panels (Figure 10-4), the nose cone, the chin panel between the nose cone and the nose landing gear door, and the

forward external tank attach fitting cover plate on the orbiter. Its purpose is to protect the orbiter from local temperatures in excess of 2300 °F. Most RCC panels are designed with a 100-mission fatigue life, but RCC panels 8 through 12 have reduced lives due to higher temperature exposures. Panel 9 has the shortest mission life of 61 missions because it has the highest heating load during entry. RCC panel 17 has the highest aerodynamic load.

The panels were originally arc jet tested. Test data indicated that the multi-use temperature limit of 2960 deg F could be sustained for approximately 600 seconds. They were structurally tested up to a 1.2 factor of safety and eventually certified by analysis up to a 1.4 factor of safety. With these parameters, the panels are certified to 140% of their expected load up to the ultimate strength of the panel. Other significant testing of the RCC panels was not performed due to lack of sufficient time to accomplish the testing prior to the first flight of *Columbia*. RCC panels show no obvious aging effects due to calendar life, but the panels normally lose mission life due to the combined effects of oxygen, high temperature, and high pressure during the entry of each mission.

On *Columbia*, the structure supporting the RCC panels consisted of four attach fittings to mount each RCC panel to the aluminum honeycomb wing leading edge spar. In an effort to reduce the orbiter weight, wing components affecting the RCC installation were redesigned on subsequent vehicles. Beginning with the orbiter *Discovery*, the RCC attachment was accomplished using a single Titanium attach fitting. The wing leading edge spar became a corrugated Aluminum structure. Additional insulation was installed behind each RCC panel on all orbiters to shield the underlying structure from radiative heat damage from the high temperatures that the RCC reaches during entry.

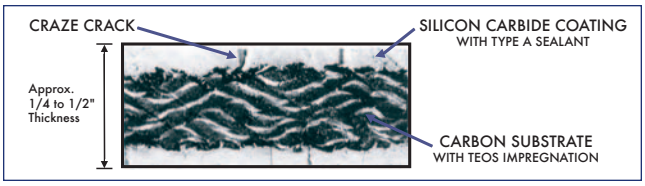

Figure 10-5. RCC cross section.

The RCC is composed of a carbon-based substrate (see Figure 10-5) that provides essentially all of the RCC strength. It is composed of graphitized rayon fabric impregnated with a phenolic resin called Tetraethyl Orthosilicate (TEOS) to provide internal protection against porosity within the laminate. The substrate is covered with a silicon carbide coating also enhanced with TEOS and sealed with a sealant to protect it from oxidation within the substrate. The silicon carbide coating provides no thermal protection for the RCC.

During the manufacturing process, the silicon carbide surface acquires surface craze cracks due to differential contraction during the cooling process. The silicon carbide coating cools faster and contracts more than the carbon substrate during the cooling process. The craze cracks sometimes extend completely through the silicon carbide coating to the carbon substrate. A sodium silicate solution called "Type A Sealant" is applied to the silicon carbide coating to decrease porosity in the surface and fill the crazing cracks. Any erosion of the type A sealant and/or the silicon carbide coating could lead to direct exposure of the carbon fibers in the substrate. This provides a path for oxidation and can potentially lead to subsequent burn through of the RCC panel during entry. Development tests for the RCC never identified a susceptibility to oxidation; therefore, *Columbia* was not treated with the type A sealant until after the first five flights. Beginning in 1992, a double type A (DTA) sealant program was instituted on all vehicles to further enhance the corrosion protection on the wing RCC.

Each time a vehicle returns from space, the entire RCC and Thermal Protection System (TPS) are visually inspected to determine the extent of any damage. Inspections look for RCC impact damage and any indications of flow in the interface between the TPS (tiles) and adjacent RCC. There also exists a test method whereby the RCC panel is pressed with a gloved hand in the vicinity of RCC cracks to determine the integrity of the panel and the existence of potential unacceptable subsurface oxidation. This same test is always performed on RCC panels 6 through 17 near each of the adjoining Tee seals. During each OMM, all RCC components are visually inspected including all the attachment hardware and underlying attachment structure.

During the inspections, a determination is made to either repair, refurbish, or replace the panel as necessary. Repairs are required when there is noticeable damage to the surface of the panel. Field repairs can be made at KSC or Palmdale unless the carbon substrate is exposed. In that case the panels must be sent to the vendor for repair. Refurbishment is required at regular intervals to recoat the panels to increase their resistance to oxidation and mass loss. Occasionally, complete replacement of RCC panels is necessary due to unrepairable damage. Each wing leading edge RCC panel is paired with an associated Tee seal and both of these components are generally replaced/refurbished as a unit.

Columbia has only had three panels/Tee seals replaced over its history. Panels 12R and 10L were removed for destructive testing and pinhole evaluations. Panel 11L had fit problems and was sent to spares. Also, over *Columbia*'s lifetime, seven RCC panels and six seals on the left wing were repaired, and 11 panels and 12 seals were refurbished. All of the *Columbia* RCC panels were within their predicted mission life limits, and most were original panels.

10.6 RCC Impact Resistance

The RCC was not considered part of the TPS for the purposes of impact resistance. The TPS was designed to accommodate particle impacts, such as from hail, rain, runway debris, etc., whose impact energy did not exceed 0.006 foot-pounds to the surface. The wing leading edge RCC impact resistance allowed no damage to the RCC with the application of up to 16 inch-pounds of energy. Figure 10-6 shows RCC impact resistance ranging from 4 to 26 inch-pounds depending on the increasing thickness of the RCC element. Different tests including low velocity and hypervelocity tests have been

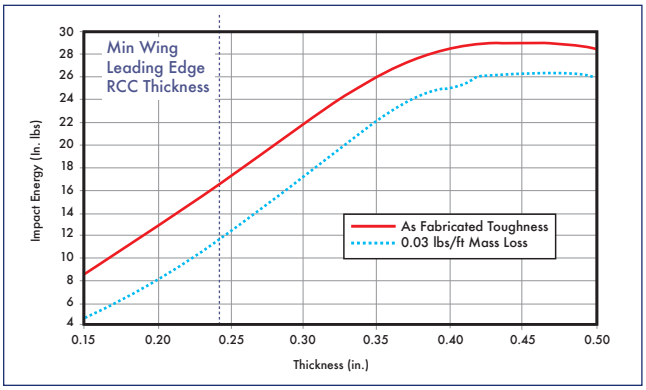

Figure 10-6. RCC impact resistance.

conducted to determine the actual impact resistance of the RCC. Test projectile materials have included nylon, glass, aluminum, steel, lead, and ice and have taken shapes of spheres, bullets, and cylinders. The test results vary widely and appear to be significantly dependent on impact velocity, projectile type, and angle of incidence of impact. Because of the variability of the test results, no actual impact resistance could be defined.

In support of the STS-107 investigation, RCC impact testing was performed at Southwest Research Institute in San Antonio, Texas, by propelling a large piece of foam at high velocity at a previously flown RCC panel. These tests were described earlier in Section 3 and show that RCC material can be damaged by ET foam at impact velocities matching STS-107 debris impact conditions.

10.7 RCC Corrosion

The RCC panels are subject to mass loss due to loss of sealant that can be caused by normal entry heating, impact damage, or even undetected chemical attack. Mass loss results in a decrease in strength, burn resistance, and RCC mission life. Under the high temperatures of entry, the sealant may become molten in the vicinity of pinholes or debris impact areas and migrate, allowing an active oxidation process to begin at the surface. Some mass loss occurs normally during each mission. Mass loss is cumulative over mission life and is determined by analysis. Previously damaged RCC panels have been measured for mass loss using computer tomography, and that data is used in the analysis for all other RCC panels' mass loss determinations. When analysis shows that the 1.4 factor of safety can no longer be maintained, the RCC panel is removed from service. The silicon carbide sealant does not prevent mass loss, but it does help increase corrosion resistance. The sealant must be refurbished periodically, but is usually performed during the most convenient OMM that does not violate the limits listed in Table 10-1.

Subsurface oxidation has been discovered beneath the silicon carbide surface cracks in the sealant and coating which allow the oxidation process to thrive. This process is considered to be an impact to RCC mission design life, but is not generally considered to be a safety of flight issue. This oxidation process (Figure 10-7) starts with the breakdown of

Panels	*Refurbishment Interval*
1-5, 20-22	As required based on visual inspection
6-17	16-18 missions, no calendar limit
18-19	32-36 missions, no calendar limit
Nose Cap	29 missions, no calendar limit

Table 10-1. RCC refurbishment limits.

the coating due to entry heating. Surface craze cracks allow oxygen to migrate to the subsurface carbon fibers and react with them. This increase in oxidation develops into larger crazed areas, which eventually allow pieces to become dislodged due to vibration, aerodynamic, or thermal loads. Once the pieces dislodge, they leave a large path for the oxidation process to continue.

Dry ultrasonic and real-time radiographic inspections have been performed on the panels in the past to look at coating damage. More recently, special non-destructive examinations are being evaluated which include infrared thermography to determine the extent of coating loss.

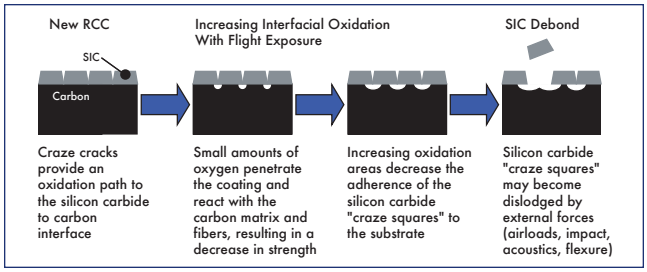

Figure 10-7. RCC corrosion process.

Each wing leading edge RCC panel shares a Tee seal that is used to close the gap between adjacent RCC panels. Following STS-43 (*Atlantis*) in August 1991, routine inspections identified cracks in the web of a Tee seal. The cracks were in the silicon carbide coating and occasionally in the substrate, and were due to normal shrinkage. They were typically less than 1/2 inch long, were not visible to the naked eye, and usually occurred in the web of the seal, on the backside of the seal (Figure 10-8) near the apex rather than on the leading edge. Further examination of the remainder of the shuttle fleet identified 20 (of 132) cracked Tee seals. *Columbia* had 11 Tee seals identified with possible cracks. Detailed inspections determined that all the cracks were typical of the surface craze cracks in the coating. The Tee seal cracks were determined to be caused by warping of the substrate fabric during lay-up during the original build. The Tee seal cracking (Figure 10-9) leads to a reduction in mission life and loss of oxidation protection. All the seals were refurbished with new coating and sealant and were reinstalled. Failure analysis showed that cracks would form after excessive wishbone loading (bending) caused the brittle coating to crack. Crack testing was performed in 1991 on Tee seal 10 (attached to RCC panel 9) from the left wing of *Columbia* to try to determine the crack mechanism. The Tee seal was cycled 400 times in bending up to 70% of its ultimate load and no dis-

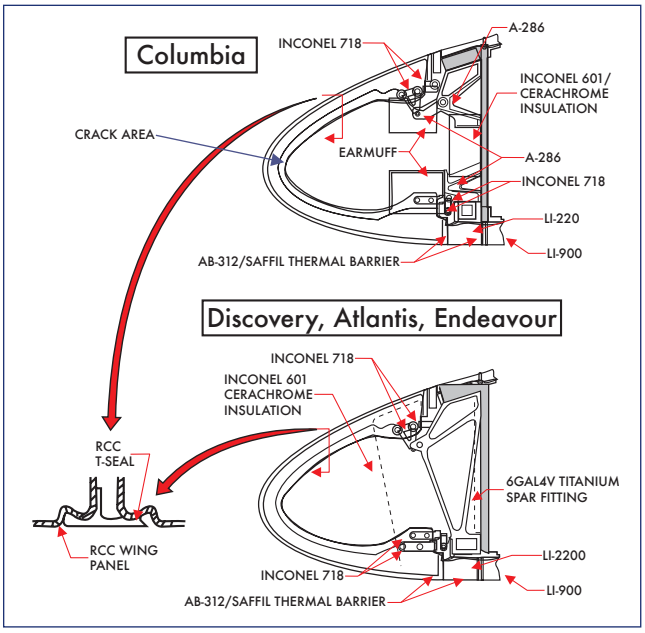

Figure 10-8. Tee seal crack location.

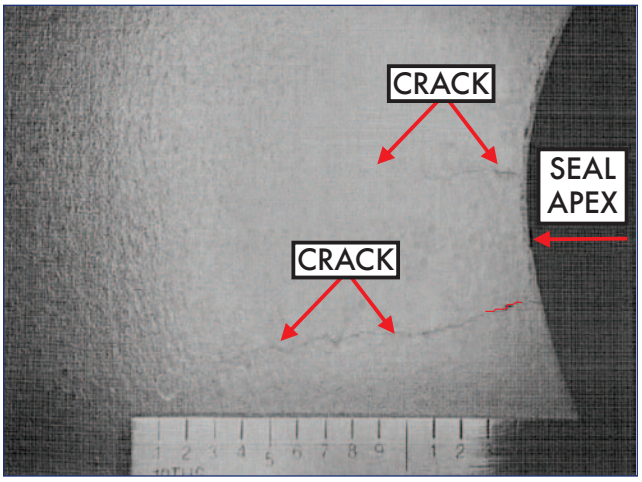

Figure 10-9. Tee seal cracking.

cernable damage was noted. After an engineering evaluation was performed on the health and strength of the Tee seal, it was subsequently reinstalled on *Columbia*.

Another phenomenon, discovered first on *Columbia* after STS-50 landed, was the existence of pinholes (Figure 10-10) in the RCC panels. The pinholes were found primarily in the wing leading edge RCC and were subsequently identified on all orbiters. Testing has shown that the pinholes are most likely the result of the accelerated oxidation process involving zinc oxide and the silicon carbide coating. The reaction of the zinc oxide and the silicon carbide produces a silica (glass) exudate that flows out of the pinhole area. The presence of zinc oxide is theorized to originate from the paint primer used to recondition the launch pad after each mission and is considered an accelerator to the oxidation process. The zinc-based contamination accumulates on the wing leading edge RCC as rainwater drips off of the launch pad. This contamination rests on the RCC without reacting to the surface material while at ambient conditions at the pad. All of the damaging oxidation occurs once the RCC is exposed to the high temperatures, pressures, and excess oxygen of reentry. Only a few pinholes have been observed on the nose cap RCC, most likely because the nose cap remains under a protective cover while at the launch pad. It is also believed that sodium chloride contributes to the oxidation process, but to a much lesser extent than the zinc oxide.

In 1997, pinhole acceptance criteria were established. Pinholes with surface dimensions less than 0.040 inches discovered during routine processing flows are acceptable to fly as is for up to 16 missions unless the carbon substrate is exposed, in which case the panel must be repaired. Pinholes discovered at OMM greater than 0.040 inches are unacceptable. Although the pinholes themselves constitute only a small mass loss, they are not considered to be a safety-of-flight issue by themselves. Analysis has identified that the sustainable thru-hole size in-flight due to orbital debris is 0.25 inches in the lower surfaces of RCC panels 5-13. A hole under 1 inch in diameter anywhere else in the RCC is considered survivable for a single mission.

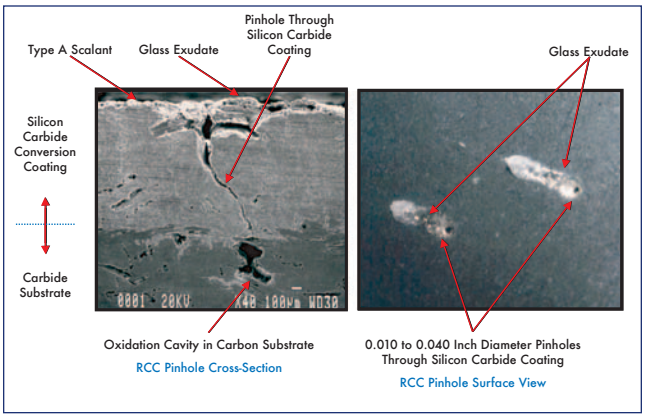

Figure 10-10. RCC pinholes.

There have been damaged RCC panels that were discovered after the vehicle returned from space on various missions. Some of the impact damage was only to the surface, but some even caused damage to the coating on the backside of the panel. In 1992, after STS-45, significant impact damage (overall length of ~1.75 inches) was noted on RCC panel

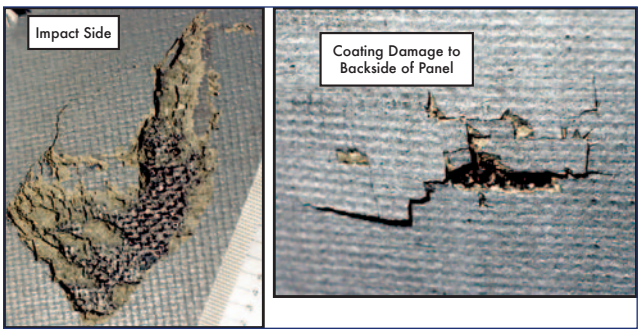

Figure 10-11. RCC impact damage.

10R on *Atlantis*. The damage (Figure 10-11) was theorized to come from orbital debris or micrometeorite impacts during the mission. This type of RCC damage is of particular concern in that a significant impact could cause a hole in the RCC large enough to lead to wing spar burn through and subsequent loss of crew and vehicle. At that time, the maximum acceptable hole size (0.040") criterion was established for processing flows and advanced wing leading edge internal insulation was modified to reduce the risk should hot gas penetrate the RCC.

There has been a history of loose bolts on access panels on all orbiters. Following STS-87, the right-hand lower access panel 4 had a loose bolt. All other installations were inspected and several additional bolts were found with low torque. All bolts were subsequently torqued to their proper values. During STS-95, the OMS pod Y-web door area had some damaged insulation. It was determined post-flight that there were bolts in the area that had low torque. A review of other orbiters identified low torque bolts on *Discovery* and *Endeavour*. Low torque bolts were also found during *Columbia*'s last OMM. The low torque was attributed to the performance of an improper torque sequence. All attach fittings were removed and reinstalled using the correct torque sequence.

11.0 External Tank

11.1 Introduction

The External Tank (ET) used for STS-107 was Light Weight Tank (LWT) number ET-93. This tank was the first LWT to be used with a cluster of three Block-II Space Shuttle Main Engines (SSMEs). As discussed in Section 3, there is significant visual and debris trajectory data to implicate the left bipod ramp area as the source of debris. Contributors to forward bipod thermal protection system (TPS) foam loss were: (1) the design, verification, and process validation did not encompass all material and processing variability or adequately address all failure modes, and (2) the acceptance testing and inspection techniques and procedures were not designed to be capable of rejecting ramps with adverse "as-built" features which would threaten the TPS integrity.

11.2 TPS Requirements

During prelaunch, the ET TPS minimizes ice formation and maintains the quality of cryogenic propellant. During ascent, the ET TPS maintains the structure within design temperature limits. Program requirements (NSTS 07700, Vol. X, Book I, Paragraph 3.2.1.2.14) indicate that the ET "shall be designed to preclude the shedding of ice and/or other debris that would jeopardize the flight crew, vehicle, mission success, or would adversely impact turnaround operations." During ET entry, the TPS assures a predictable, low altitude ET break-up that meets the ET entry impact footprint boundary limits.

The ET TPS itself is designed to have low density to maximize Shuttle payload capacity, high adhesion to cryogenic surfaces (-423 °F), resistance to thermal abrasion and degradation from aerodynamic shear, consistency (material qualified is the material flying), and environmental resistance to ultraviolet radiation, rain, etc. The application of ET TPS materials includes computer controlled automatic spray cells and manual application in normal working environments.

11.3 History of Foam Changes and Debris Events

The ET TPS history is marked by multiple material and configuration changes resulting from ET TPS and ice loss events, design enhancements, environmental regulations (especially blowing agent changes), and supplier changes. The history of foam changes is outlined in Figure 11-1, and Table 11-1 lists the ET flight history, as well as age and exposure data. Thousands of tests have been conducted to develop and qualify the ET TPS. There were no first time ET TPS changes on STS-107/ET-93 except for rework of the TPS on the upper aft ET/Solid Rocket Booster (SRB) fitting fairing (following SRB demate) using BX-265. Basic bipod TPS materials had not changed from the beginning of the program until after ET-93. The bipod TPS configuration has been stable since 1983, when with ET-14 the ramp angle was changed. At ET-76 in 1995, there was one minor change to the ramp intersection with the ET intertank area. At ET-116 in 2002, the bipod material was changed to BX-265, but ET-93 had been constructed with BX-250. No indication has been found that any specific ET TPS foam change or any combination of historical ET TPS foam changes alone caused the bipod foam loss on STS-107/ET-93.

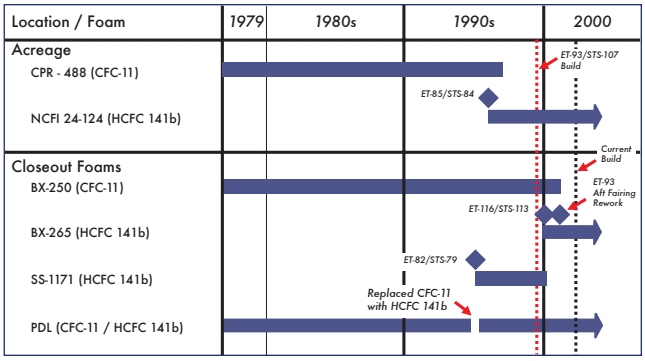

Figure 11-1. History of foam changes. Blowing agent shown in parentheses. No changes to SLA.

ET debris has been observed throughout program history, including both ET TPS and ice debris. Since STS-1, imagery was available on about 80 missions, and debris has been confirmed on at least 62 missions. At least six missions lost portions of the left bipod ramp (see Section 3.5). TPS loss on the right bipod ramp has never been observed. A portion of the left bipod ramp was lost during STS-112 ascent and impacted the left SRB Integrated Electronics Assembly. No changes were made to STS-113 or STS-107 bipod ramp configurations after this event.

The majority of ET debris events have been limited to small mass (< 0.2 lbs). A definitive correlation to orbiter damage is difficult except for major debris events such as STS-27R, which was identified as SRB ablator debris, and STS-87,

which was attributed to ET intertank foam loss. Based on available historical data, the bipod ramp represents the source of the largest pieces of ET debris (estimated > 1.0 lbs), and LO2 feedline bellows ice is second (estimated < 0.3 lbs).

11.4 STS-107/ET-93 Chronology

Ascent film indicates that the origin of STS-107 ET TPS loss was from the forward bipod area (see Section 3). Image-based size estimates support this to be the bipod ramp rather than flange or acreage foam. The history of bipod TPS loss provides additional supporting evidence. Available data supports the bipod ramp as the most probable point of origin of STS-107 debris.

11.4.1 Bipod Ramp TPS Configuration

The forward bipod TPS configuration includes a complex combination of foams, Super Light Ablator (SLA), and underlying bipod structural substrate elements. The bipod ramp configuration has been essentially stable since early in the program. There have been no changes in material until after ET-93 and only minimal changes to configuration, processing, and personnel certification and training. The BX-250 ramp angle has been constant since 1983, when with ET-14, the ramp angle was changed to 30° maximum with a 5.0 ±1.0 inch radius at the forward edge (changed from 45° ± 5.0° with no radius at the forward edge). This was changed as a result of suspected foam debris on STS-7/ET-6. For ET-76 in 1995, there was one minor change to the forward ramp intersection with the ET intertank area; the 5.0 ±1 inch radius was changed to a straight termination line with a 0.25-inch step allowed. At ET-116 in 2002, the bipod material was changed to BX-265, but ET-93 was BX-250. There has been no indication that the bipod ramp configuration changes affected the observed STS-107/ET-93 bipod foam loss.

STS	STS aka	OV	ET	ET wt.	Date	ET Age @ Launch (days)	ET Exposure @ Launch (days)
1		Columbia	1	ET	04/12/81	653	105
2		Columbia	2	ET	11/12/81	258	74
3		Columbia	3	ET	03/22/82	175	35
4		Columbia	4	ET	06/27/82	161	33
5		Columbia	5	ET	11/11/82	169	52
6		Challenger	8	LWT	04/04/83	208	126
7		Challenger	6	ET	06/18/83	327	24
8		Challenger	9	LWT	08/30/83	230	29
9		Columbia	11	LWT	11/28/83	206	43
11	41B	Challenger	10	LWT	02/03/84	339	23
13	41C	Challenger	12	LWT	04/06/84	259	19
14	41D	Discovery	13	LWT	08/30/84	352	79
17	41G	Challenger	15	LWT	10/05/84	295	23
19	51A	Discovery	16	LWT	11/08/84	286	17
20	51C	Discovery	14	LWT	01/24/85	448	20
23	51D	Discovery	18	LWT	04/12/85	353	16
24	51B	Challenger	17	LWT	04/29/85	409	33
25	51G	Discovery	20	LWT	06/17/85	347	14
26	51F	Challenger	19	LWT	07/29/85	431	31
27	51I	Discovery	21	LWT	08/27/85	398	22
28	51J	Atlantis	25	LWT	10/03/85	287	35
30	61A	Challenger	24	LWT	10/30/85	348	15
31	61B	Atlantis	22	LWT	11/26/85	459	15
32	61C	Columbia	30	LWT	01/12/86	208	42
33	51L	Challenger	26	LWT	01/28/86	319	38
26R		Discovery	28	LWT	09/28/88	1261	87
27R		Atlantis	23	LWT	01/02/89	1561	62
29R		Discovery	36	LWT	03/13/89	1189	39

Table 11-1. STS-Orbiter-ET configuration, age, and exposure.

[continued on next page]

STS	STS aka	OV	ET	ET wt.	Date	ET Age @ Launch (days)	ET Exposure @ Launch (days)
30R		*Atlantis*	29	LWT	05/04/89	1450	44
28R		*Columbia*	31	LWT	08/08/89	1484	25
34		*Atlantis*	27	LWT	10/18/89	1723	51
33R		*Discovery*	38	LWT	11/22/89	1317	27
32R		*Columbia*	32	LWT	01/09/90	1609	43
36		*Atlantis*	33	LWT	02/28/90	1597	35
31R		*Discovery*	34	LWT	04/24/90	1674	40
41		*Discovery*	39	LWT	10/06/90	1635	32
38		*Atlantis*	40	LWT	11/15/90	1609	88
35		*Columbia*	35	LWT	12/02/90	1850	164
37		*Atlantis*	37	LWT	04/05/91	1906	22
39		*Discovery*	46	LWT	04/28/91	1327	49
40		*Columbia*	41	LWT	06/05/91	1776	35
43		*Atlantis*	47	LWT	08/02/91	1323	39
48		*Discovery*	42	LWT	09/12/91	1829	32
44		*Atlantis*	53	LWT	11/24/91	846	33
42		*Discovery*	52	LWT	01/22/92	994	35
45		*Atlantis*	44	LWT	03/24/92	1840	34
49		*Endeavour*	43	LWT	05/07/92	2005	56
50		*Columbia*	50	LWT	06/25/92	1333	23
46		*Atlantis*	48	LWT	07/31/92	1561	51
47		*Endeavour*	45	LWT	09/12/92	1923	19
52		*Columbia*	55	LWT	10/22/92	994	27
53		*Discovery*	49	LWT	12/02/92	1577	25
54		*Endeavour*	51	LWT	01/13/93	1440	42
56		*Discovery*	54	LWT	04/08/93	1256	25
55		*Columbia*	56	LWT	04/26/93	1082	79
57		*Endeavour*	58	LWT	06/21/93	979	55
51		*Discovery*	59	LWT	09/12/93	900	80
58		*Columbia*	57	LWT	10/18/93	1180	33
61		*Endeavour*	60	LWT	12/02/93	889	36
60		*Discovery*	61	LWT	02/03/94	842	25
62		*Columbia*	62	LWT	03/04/94	773	23
59		*Endeavour*	63	LWT	04/09/94	737	22
65		*Columbia*	64	LWT	07/08/94	718	24
64		*Discovery*	66	LWT	09/09/94	591	23
68		*Endeavour*	65	LWT	09/30/94	697	47
66		*Atlantis*	67	LWT	11/03/94	535	25
63		*Discovery*	68	LWT	02/03/95	546	25
67		*Endeavour*	69	LWT	03/02/95	484	23
71		*Atlantis*	70	LWT	06/27/95	495	63
70		*Discovery*	71	LWT	07/13/95	435	58

Table 11-1 (continued). STS-Orbiter-ET configuration, age, and exposure. *[continued on next page]*

STS	STS aka	OV	ET	ET wt.	Date	ET Age @ Launch (days)	ET Exposure @ Launch (days)
69		Endeavour	72	LWT	09/07/95	433	59
73		Discovery	73	LWT	10/20/95	381	54
74		Atlantis	74	LWT	11/12/95	360	33
72		Endeavour	75	LWT	01/11/96	342	37
75		Columbia	76	LWT	02/22/96	330	25
76		Atlantis	77	LWT	03/22/96	303	24
77		Endeavour	78	LWT	05/19/96	307	34
78		Columbia	79	LWT	06/20/96	281	23
79		Atlantis	82	LWT	09/16/96	188	38
80		Columbia	80	LWT	11/19/96	368	35
81		Atlantis	83	LWT	01/12/97	262	34
82		Discovery	81	LWT	02/11/97	390	26
51		Discovery	59	LWT	09/12/93	900	80
58		Columbia	57	LWT	10/18/93	1180	33
61		Endeavour	60	LWT	12/02/93	889	36
60		Discovery	61	LWT	02/03/94	842	25
62		Columbia	62	LWT	03/04/94	773	23
59		Endeavour	63	LWT	04/09/94	737	22
65		Columbia	64	LWT	07/08/94	718	24
64		Discovery	66	LWT	09/09/94	591	23
68		Endeavour	65	LWT	09/30/94	697	47
66		Atlantis	67	LWT	11/03/94	535	25
63		Discovery	68	LWT	02/03/95	546	25
67		Endeavour	69	LWT	03/02/95	484	23
71		Atlantis	70	LWT	06/27/95	495	63
70		Discovery	71	LWT	07/13/95	435	58
69		Endeavour	72	LWT	09/07/95	433	59
73		Discovery	73	LWT	10/20/95	381	54
74		Atlantis	74	LWT	11/12/95	360	33
72		Endeavour	75	LWT	01/11/96	342	37
75		Columbia	76	LWT	02/22/96	330	25
76		Atlantis	77	LWT	03/22/96	303	24
77		Endeavour	78	LWT	05/19/96	307	34
78		Columbia	79	LWT	06/20/96	281	23
79		Atlantis	82	LWT	09/16/96	188	38
80		Columbia	80	LWT	11/19/96	368	35
81		Atlantis	83	LWT	01/12/97	262	34
82		Discovery	81	LWT	02/11/97	390	26
83		Columbia	84	LWT	04/04/97	291	25
84		Atlantis	85	LWT	05/15/97	281	22
94		Columbia	86	LWT	07/01/97	266	21
85		Discovery	87	LWT	08/07/97	246	25

Table 11-1 (continued). STS-Orbiter-ET configuration, age, and exposure.

[continued on next page]

STS	STS aka	OV	ET	ET wt.	Date	ET Age @ Launch (days)	ET Exposure @ Launch (days)
86		Atlantis	88	LWT	09/25/97	251	39
87		Columbia	89	LWT	11/19/97	146	22
89		Endeavour	90	LWT	01/22/98	167	35
90		Discovery	91	LWT	04/17/98	154	26
91		Discovery	96	SLWT	06/02/98	141	32
95		Discovery	98	SLWT	10/29/98	147	39
88		Endeavour	97	SLWT	12/04/98	249	47
96		Discovery	100	SLWT	05/27/99	183	24
93		Columbia	99	SLWT	07/23/99	360	47
103		Discovery	101	SLWT	12/19/99	24	37
99		Endeavour	92	LWT	02/11/00	298	61
101		Atlantis	102	SLWT	05/19/00	473	56
106		Atlantis	103	SLWT	09/08/00	444	26
92		Discovery	104	SLWT	10/11/00	498	31
97		Endeavour	105	SLWT	11/30/00	503	31
98		Atlantis	106	SLWT	02/07/01	418	30
102		Discovery	107	SLWT	03/08/01	455	25
100		Endeavour	108	SLWT	04/19/01	434	29
104		Atlantis	109	SLWT	07/12/01	435	22
105		Discovery	110	SLWT	08/10/01	380	40
108		Endeavour	111	SLWT	12/05/01	258	36
109		Atlantis	112	SLWT	03/01/02	358	38
110		Atlantis	114	SLWT	04/08/02	294	28
111		Endeavour	113	SLWT	06/05/02	401	38
112		Atlantis	115	SLWT	10/07/02	376	28
113		Endeavour	116	SLWT	11/23/02	360	43
107		Columbia	93	LWT	01/16/03	805	39

Table 11-1 (concluded). STS-Orbiter-ET configuration, age, and exposure.

11.4.1.1 Left and Right Bipod Ramp Differences

TPS loss on the right bipod ramp has never been observed. Launch/ascent imagery from ground assets is less favorable for seeing right bipod foam loss as compared to the left bipod, and post-ET separation crew imagery is random between imaging the left or right bipod ramps.

There is no flight or test data to explain why the –Y (left) bipod looses foam and the +Y (right) does not. The Shuttle Program only provides the –Y ramp air loads as a worst case for ET project analysis. There are several bipod configuration differences that may contribute to foam not coming off the +Y ramp. First, the foam ramp is configured slightly differently to accommodate the inboard strut for the LO2 feed line support structure (see Figure 11-2). Second, the proximity of the right bipod to the LO2 feedline could potentially influence local surface pressure causing a lower internal to

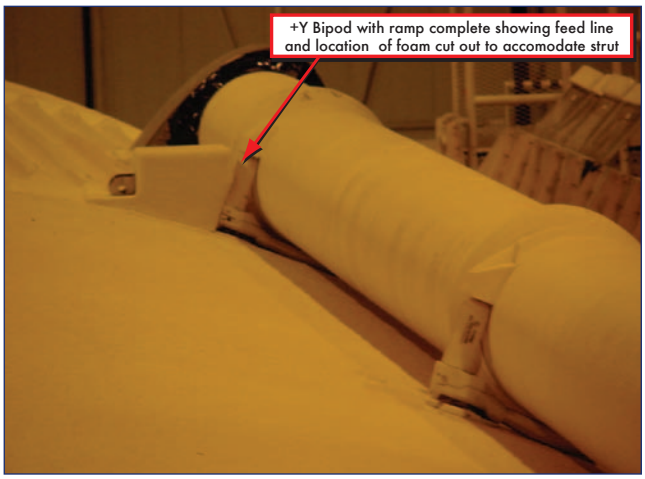

Figure 11-2. Right (+Y) bipod ramp.

external pressure differential (see Figure 11-3). Finally, the outboard and aft facing surface of the –Y bipod may experience lower surface pressure due to flow separation and other local effects relative to the +Y side. If the internal ramp pressure was high due to adverse "as-built" features in the ramp, this could lead to a higher differential pressure on the –Y versus the +Y ramp. However, the aerodynamic loads analysis reviewed in Section 3.5 shows that the loads on both ramps are below their design requirements.

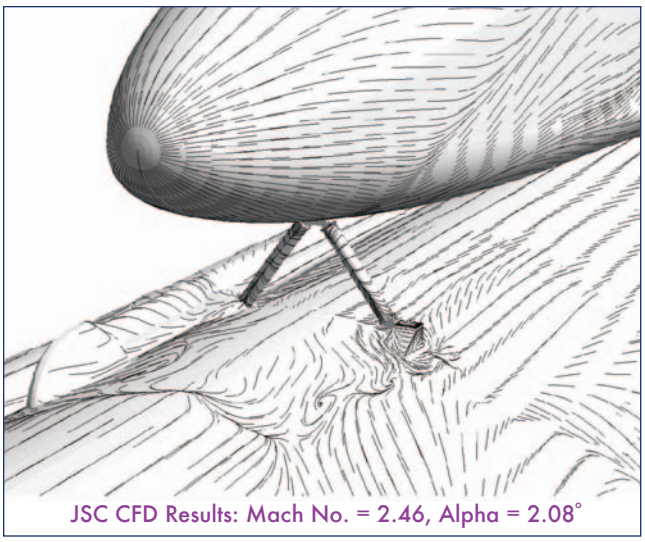

Figure 11-3. Left and right bipod ramp flow differences, CFD results.

11.4.2 Bipod Ramp Certification

The BX-250 foam was supplied to the ET project as a flight verified material from the Saturn Program. A review of material properties certification indicated forward bipod materials met material performance requirements including thermal recession properties at design ascent heating rates, thermal conductivity to preclude ice formation and to maintain cryogenic propellant quality during prelaunch, and mechanical properties.

Process validation was performed by similarity of "flight-like" design substrate configurations. There had been no specific bipod dissection prior to the STS-107/ET-93 investigation. Dissection of the bipod ramps from the production flow provided insight that the bipod ramp could contain unique adverse "as-built" features. The features identified during these recent dissections could potentially reduce the strength of the foam and result in foam failure and subsequent debris.

For the bipod ramp, there was no robust evaluation of the manual spray process. The complexity of the manual spray process of the forward bipod TPS closeout leads to unique defects in this area including voids, rollovers, and TPS discontinuities. The configuration of the forward bipod BX-250 foam was verified based on similarity to the Protuberance Air Load (PAL) ramp, which did not address all aspects and failure mechanisms in combination with critical environments (adverse "as-built" features). The interaction of the underlying SLA configuration interfacial boundary and the potential effects of cryopumping were not considered. The design, verification, and process validation did not encompass all material and processing variability or adequately address all failure modes.

11.4.3 Bipod Ramp Build Process

Experienced certified practitioners performed the ET-93 bipod ramp BX-250 sprays, each with over 20 years experience. No indications of sprayer error were found. Procedures were followed and documented, and processes were within control limits (e.g., material specifications, temperature, and humidity) except that the process plan review found no Quality Control (QC) verification of overlap timing. There is no requirement to verify the overlap timing, and the impact of the overlap timing verification is not known.

Dissection results of five ET TPS configurations demonstrated the forward bipod as the configuration with the most significant defects. Defects are driven by the variable manual spray process and complex contour substrate. This creates the potential for a combination of large voids or defects at critical locations needed to produce a significant foam loss. The designed-in process plan controls related to QC buy-off of critical parameters did not preclude introduction of adverse "as-built" features resulting from the complex and variable forward bipod manual spray operation. There is also variability in the response of the foam based on inherent randomness of the foam cell structure. It may not be possible to control a manual process well enough to preclude defects in the bipod ramp.

11.4.4 Bipod Ramp Foam Acceptance/Non-Destructive Evaluation

ET BX-250 ramp foam build acceptance processes include localized plug pull and core tests of the ramp material prior to final trim configuration. The plug-pulls are taken from trimmed-off over-spray lead-in/lead-out areas (witness, or sample panels) on either side of the ramp to provide density, final visual inspections, and dimensional features. Post-build inspection techniques are limited to visual inspections only. There were no anomalies found with the STS-107/ET-93 forward bipod ramp using inspection and acceptance techniques available at Michoud Assembly Facility (MAF).

Previous efforts to implement robust foam Non-Destructive Evaluation (NDE) techniques were unsuccessful (a variety of techniques were attempted). Some progress was made in certain areas, but it never reached a fully qualified approach and the MAF effort was discontinued in 1993. Development efforts found many false positives and many missed defects. NDE methods in use at MAF were not able to identify adverse "as-built" features in the forward bipod BX-250 ramp, which could combine with nominal environments and create debris. Acceptance testing and inspection techniques and procedures were not designed to be capable of rejecting ramps with adverse "as-built" features that would threaten the TPS integrity.

11.4.5 ET Shipping and Handling

Post-build activities include storage at MAF, shipment to Kennedy Space Center (KSC), storage at KSC, and mating to the SRBs and orbiter. Extensive documentation governs the steps taken to care for the ET. Documentation review found no issues in ET-93 processing paperwork. Storage took place in locked, limited-access facilities. The tanks were shipped pressurized with nitrogen to 6.0 ± 0.5 psi per requirements. At KSC, the LH2 tank pressurant is changed to helium and the pressure on each tank is checked at least twice per week per requirements. Visual inspections were performed every 90 days while in storage. ET-93 was inspected seven times between arrival at KSC and launch, not counting additional daily inspections when mated to the SRBs. Processes were in place and followed to ensure that shipping and handling were performed in a manner that minimizes damage to the ET.

11.4.6 KSC Processing Activities

The shuttle flight manifest was delayed due to cracks found during inspections of Main Propulsion System feedline flow liners on *Atlantis* in June 2002. The final manifest moved STS-112 and STS-113 ahead of STS-107. ET-93 was demated from SRBs BI-114/RSRM-86 and later mated to SRBs BI-116/RSRM-88, and SRBs BI-114/RSRM-86 were used for STS-113. All mate/de-mate operations were carried out in accordance with standard procedures, and are outlined in Figure 11-4. There are no indications that KSC ET processing (ET shipping, handling, and processing) contributed to the bipod foam loss on STS-107/ET-93.

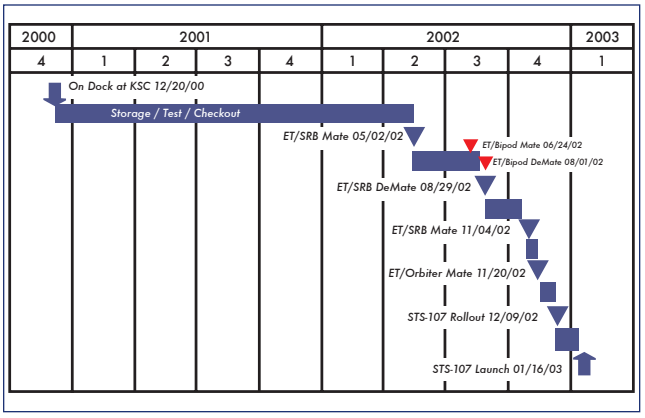

Figure 11-4. ET-93 processing timeline at KSC.

11.4.6.1 ET-93 Mate/De-Mate/Re-Mate

The ET-93 bipod struts were installed, and then later removed during de-mate and re-installed. This process has been performed at least six times during the Shuttle program. ET-11 was used on STS-9, but there is no imagery to confirm ET foam loss. ET-13 was used on STS-14 (41D), but again there is no imagery to confirm ET foam loss. ET-23 was used on STS-27R with handheld video imagery available that does not show the bipod ramps, but no foam loss was observed elsewhere. ET-23 was mated and de-mated during checkout of the Vandenberg Air Force Base facilities. STS-27R had a great amount of tile damage thought to be due to the loss of SRB ablator during launch. ET-37 was used on STS-38 but there is no imagery to confirm ET foam loss. ET-80 was used on STS-80, and there were two lost divots on the flange under the bipod and one 10-inch diameter divot on the intertank forward of the bipods. ET-86 was used on STS-94 and the left bipod strut was installed upside down then re-installed correctly. The bipod ramps were visible and no bipod foam loss was noted.

11.4.6.2 ET-93 Crushed Foam

On ET-93, crushed foam (1.5" x 1.25" x 0.187") was seen after the –Y strut removal at the clevis. The thickness of foam in this area is 2.187 inches. Exposed crushed foam is not permissible outside of specific acceptance criteria, so a Problem Report (PR VG-389216) was written to evaluate the condition. The crushed foam was essentially covered up after mating to a new set of bipod struts. No data is available to determine if this section of foam could have been the source of, or contributed to, a void or leak path for liquid or gas.

Inspection of the region after installation of the bipod struts showed that the crushed foam did not extend farther than 0.75" beyond the bipod fitting-clevis joint, which is within acceptable limits. Dye penetration testing with recreated conditions indicated that the damage extended 0.25 inches from the visible mark and 0.5 inches into the surface of the foam, where the damage stopped.

The Material Review Board (MRB) decided to "use as is," and STS-107 launched with crushed foam contained behind the –Y bipod strut clevis. Crushed foam in this area is a nominal configuration, and the PR was only written for documentation for bipod strut removal and future inspections. Available data indicates that every flight may have crushed foam beneath the bipod strut. Review of the ET-93 PR, MAF testing, and the ET-117 strut removal provided evidence that crushed foam had no impact on performance, both thermal and structural. Data are inconclusive as to whether the crushed foam and bipod foam loss are associated.

11.4.7 ET Pre-launch Operations

The electrical system performance was nominal based on evaluation of pre-launch data and post flight inspection of ground electrical interfaces and SRB hardware. No anomalous conditions were identified during STS-107 visual inspections during launch operations: preflight, tanking ice team, video surveillance, and postflight walk down. There are no indications that ET pre-launch operations at KSC contributed to bipod foam loss on STS-107/ET-93.

11.4.8 Launch/Ascent

The ET-93 propulsion system performance was within design limits based on preflight predictions and postflight reconstruction. Comparison to historical performance showed performance within flight history experience for LWT, Super Light Weight Tank (SLWT), and Block II SSME. The STS-107 trajectory was within design limits through-

out ascent. There were no anomalous angles of attack or dynamic pressure indications (see Section 3.5). STS-107 reconstructed air loads were within design limits, and no unique observations were associated with STS-107/ET-93. It is unlikely that any significant bipod structural loads were associated with the 62 second wind shear event followed by a 0.6 Hz RSRM gimbal reaction associated with LO2 slosh (see Section 3.5 and sections below). No anomalous structural loads have been identified. Best-estimated trajectory loads and flex body loads assessment reconstructions show the ET interfaces to be well within design limits. Bipod interface vehicle loads are not considered "driving" environments for the bipod foam ramp. Adjacent structural stiffness precludes significant induced bipod ramp deflections from the interface strut loads. The majority of flexural loading on the bipod ramp results from cryogenic shrinkage of the LH2 tank prior to lift-off. STS-107 ascent thermal environments were within design limits based on analysis of flight data and ET system performance. A higher LH2 tank ullage preflight pressurization pressure (pre-press) is required for flights with Block-II SSME clusters. This helps reduce spikes in the high-pressure fuel turbopump turbine discharge temperatures during start. The LWT was certified for higher pre-press and approved for ET-92 and subsequent flights by Interface Revision Notice (IRN) IC-1432 on 8-28-98.

Data are inconclusive as to whether the STS-107 ascent environments contributed to the bipod foam loss on ET-93.

11.4.8.1 ET LO2 Slosh Baffle Changes

Eight ET LO2 slosh baffles were used until ET-14 in 1983. Vehicle stability analysis based on development flight instrumentation confirmed minimum LO2 sloshing disturbances and Space Shuttle Program LO2 damping requirements were subsequently reduced. Analysis and sub-scale test showed the baffle count could be reduced from eight to two and still maintain margin, but a reduction to four was selected as a trade off between cost benefit and weight reduction (see Figure 11-5).

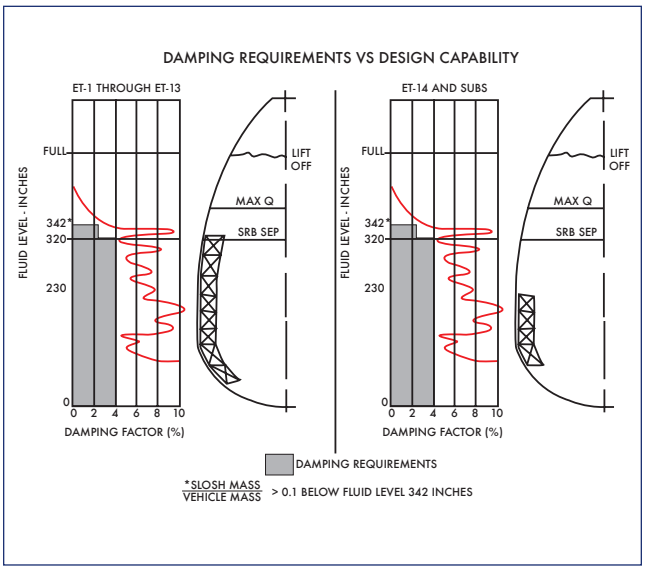

Figure 11-5. ET LO2 slosh baffle changes – ET-14.

One weight saving feature of the SLWT is the removal of one more slosh baffles section, as shown in Figure 11-6. This gives a predicted performance gain of 92 pounds. This feature was incorporated into the LWT at ET-87 in 1996 to reduce weight and diminish the number of first time configuration changes for the subsequent first flight of the SLWT. Dynamics analysis showed available damping remained within requirements and propulsion and stress analysis also remained within requirements. Data are inconclusive as to whether the ET LO2 slosh baffle configuration alone caused bipod foam loss on STS-107/ET-93.

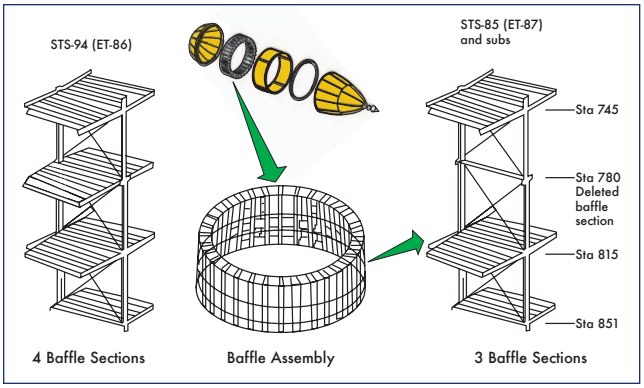

Figure 11-6. ET LO2 slosh baffle changes – ET-87.

11.4.9 Possible Contributors to Strain Energy at ET Separation

The Space Shuttle Program Loads Panel is continuing to work actions to identify potential contributors to strain energy that could have led to the off-nominal yaw rate at ET separation described in Section 3.5. For induced loads during ground operations, KSC is reviewing handling and stacking (orbiter and Ground Ops). For loads that occurred during flight, Boeing GNC is looking into the left side thermal event at 300 seconds MET and if the mechanical load overcomes the joint preload during ascent. The ET project is looking into loads induced through cryogenic and pressurization cycles and the effects on the ET, such as shrinkage of the diagonal strut and overall shrinkage of the ET affecting the forward and aft attachments. The data are inconclusive as to whether potential strain energy at ET separation can be associated with events that caused bipod foam loss on STS-107/ET-93.

11.5 STS-107/ET-93 TPS Bipod Debris

11.5.1 Bipod Foam Failure Modes and Contributors

Four basic possible bipod failure modes have been identified (shown in Figure 11-7) and each may occur alone or act in combination with each other. However, due to lack of bipod instrumentation, it is impossible to know exactly why part of the left bipod foam came off ET-93 during STS-107 ascent. Cracking is a break in the foam, which does not exhibit material loss and is typically perpendicular to the substrate. Debond or delamination is a separation of the material running along the substrate or layer lines. A divot is a piece of

material dislodged from the surface resulting in a cavity, which may or may not expose the substrate. Shear is the removal or separation of material within the cell structure and is not confined to the layer lines of the material, but is parallel to the substrate.

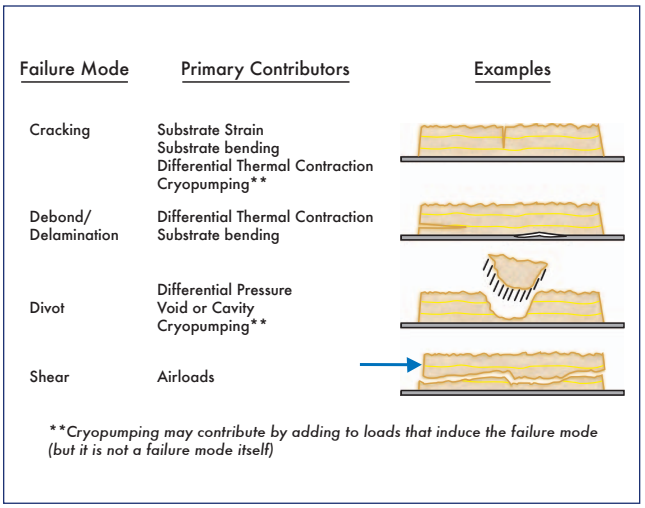

Figure 11-7. Bipod foam failure modes.

Cryopumping could contribute to bipod foam loss, shown schematically in Figure 11-8. The mechanism that drives cryopumping is the transformation of a gas to a liquid at cryogenic temperatures. Gases may condense within a void or porous material at low temperatures. Air in cavities or porous material liquefies when in contact with structure below -297°F for oxygen or -320°F for nitrogen. Pressure is reduced locally due to the condensation. If a leak path exists, more air will be "pumped," providing more gas to condense. When the structure warms, the consequence of cryopumping is that the liquefied air returns to the gaseous state with a local pressure increase. If the leak path is large, gas escapes with no detrimental effect. However, if the leak path is small, cracks may form in the TPS to relieve pressure, or a rapid increase in pressure may result in a divot. In order for this to occur, the inlet source must be blocked off to avoid venting out the inlet. It should be noted that testing has been unable to demonstrate cryopumping in this application.

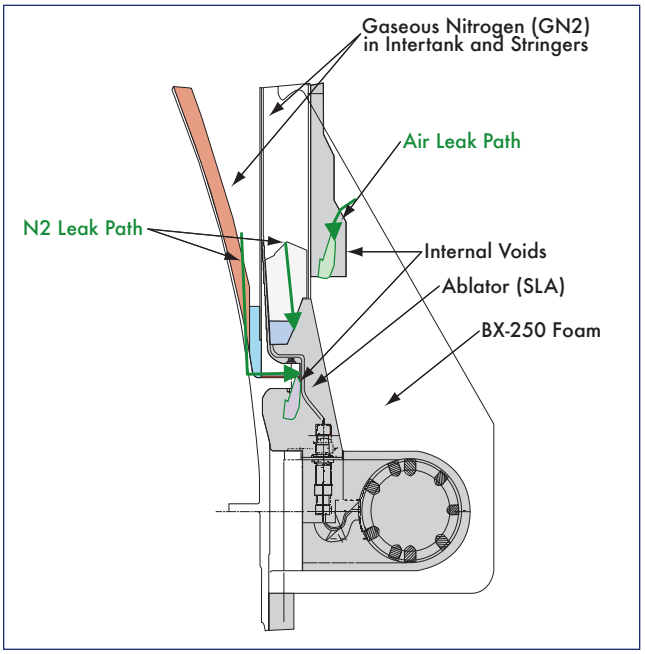

Figure 11-8. Schematic of bipod ramp - potential cryopumping.

11.5.2 Test Results for Debris Assessment

Bipod TPS static and dynamic coupon tests were performed (test ET-TR-003). The objectives of these tests were to evaluate the BX-250/SLA hand-pack (HP) bond line laminate mechanical properties and investigate whether liberated BX-250 material could "pull" or "tear" SLA HP material from the bipod region. Analysis shows the critical bipod Spray-On Foam Insulation (SOFI) ramp failure mode due to direct air load is shear failure between SOFI ramp and bipod fitting substrate.

Testing shows that the potential loss of BX-250 does not liberate hand packed SLA due to impulse loading for cryogenic applications; the BX-250 fails before the SLA. For shear, testing shows BX-250 fails before SLA at all test temperatures. For tension, testing shows BX-250 fails before SLA when SLA temperatures are less than or equal to -100 °F (see Figure 11-9).

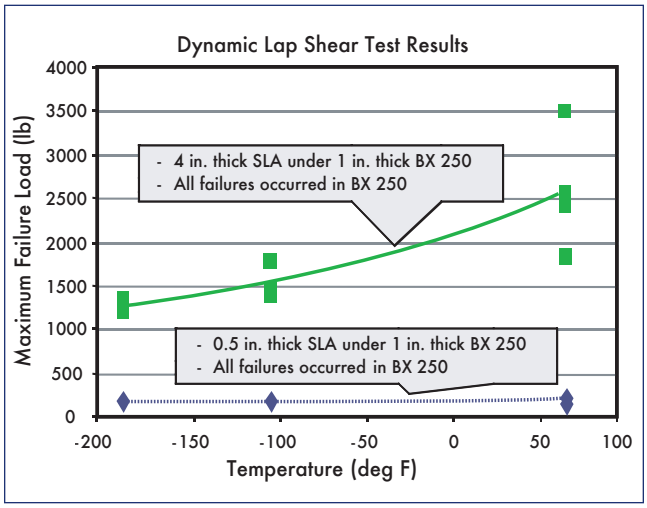

Figure 11-9. Critical test results in debris assessment.

11.5.3 Max Bipod SLA Temperatures (80 seconds MET)

The maximum SLA temperatures possible at 80 seconds were analyzed to determine maximum worst-case multi-event material loss. No cryopumping or cryo ingestion was assumed in order to calculate temperatures as high as possible. STS-107 ambient environments were used. Results showed the maximum SLA temperature possible at 80 seconds MET is less than or equal to -100 °F, as shown in Figure 11-10. Tension testing shows BX-250 fails before SLA at temperatures less than or equal to -100 °F.

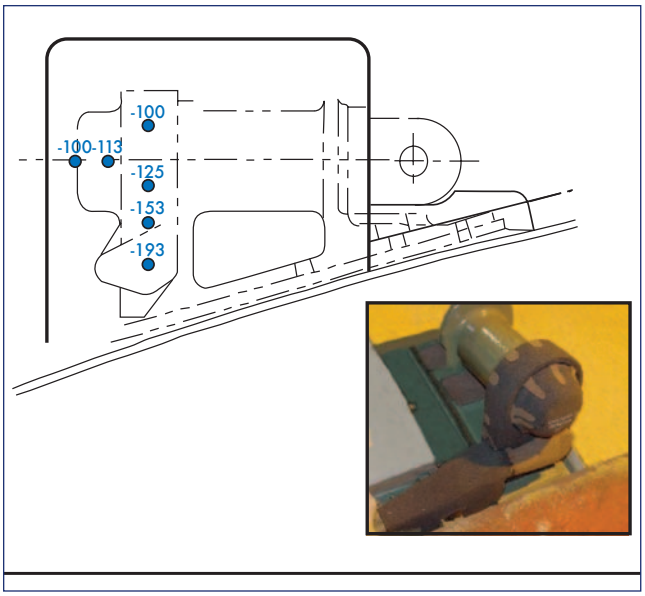

Figure 11-10. Max bipod SLA temperatures (80 seconds MET), °F.

11.5.4 Bipod Ramp As-Built Hardware Assessment

The dissection of six bipod ramps indicated similar patterns for geometry-induced defects in all ramps. Roll-overs were observed at complex substrate elements, and the majority of observations were associated with spraying over complex details at the substrate. Sporadic voids were also observed. One internal delamination and one weak plane at the knit line were observed. Critical locations, or areas at-risk for producing debris, were identified near the edge of the machined foam surface for both voids and roll-overs (see Figure 11-11). Vacuum pressure is the primary driver for divot formation; however, wind shear also contributes to flight loads. A combination of multiple large voids, geometry-induced defects, and critical locations is needed to produce significant foam loss. For example, a large interconnected void at close proximity to the surface plus a "weakened plane" (see Figure 11-12) may produce foam loss.

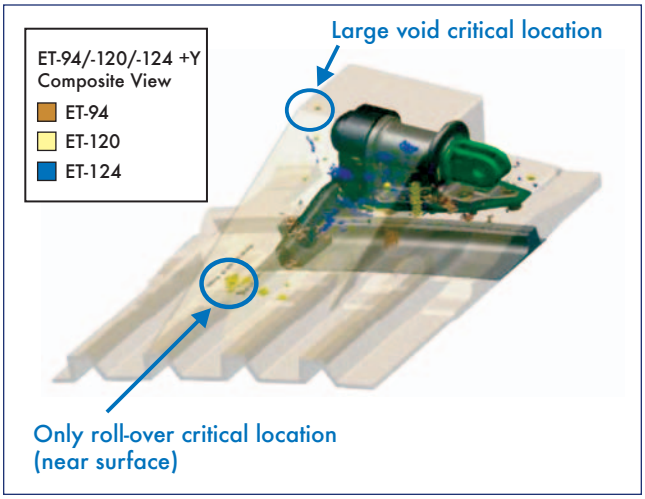

Figure 11-11. Defects found at critical locations.

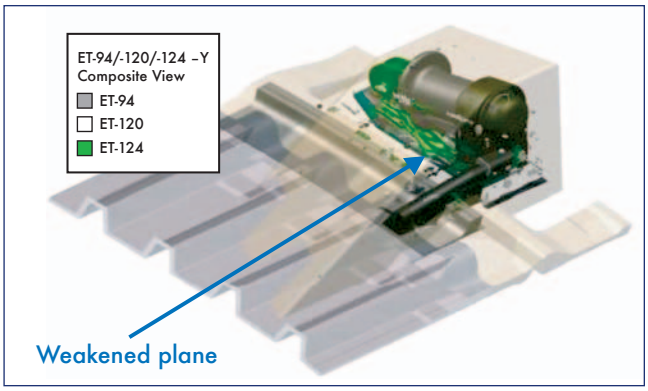

Figure 11-12. Weakened plane defect found.

11.5.5 Multi-Failure Mode TPS Bipod Debris

The ET Working Group conducted an analysis coupled with test data to estimate a multi-failure mode TPS bipod debris size and weight. The ET Working Group scenario includes seven simultaneous and interactive adverse events: A large rollover occurs at the inboard stringer interface immediately below the machined foam surface, side-to-side thermal crack/weak knit line, a large void near the topmost surface one inch below machined foam surface, warm SLA environment, and foam machined to minimum tolerances (not a failure). The specific results are shown in Figure 11-13.

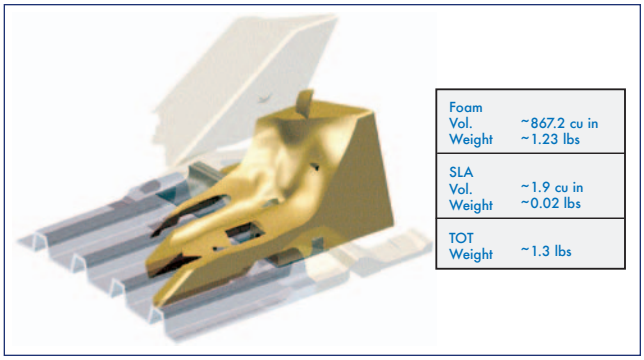

Figure 11-13. Multi-failure mode bipod TPS debris estimated by the ET Working Group. Note that this size and weight were not used in the RCC impact testing as part of the STS-107 investigation.

The determination of the STS-107/ET-93 bipod TPS debris is based on evaluation of fault tree findings, possible TPS failure modes and contributors, and results to date from TPS debris test programs including dissection, foam loss secondary effects assessment (SLA/BX-250), and bipod TPS debris size analysis. The TPS bipod debris size was determined by the ET Working Group to be approximately 870 cubic inches and 1.3 pounds.

The transport analysis presented in Section 3 suggests that the debris object may be heavier than average foam, but the ET Working Group analysis indicates there could not be ice or significant SLA in the debris and that the density of the foam is consistent. Also, the imagery analysis showed that

not all the debris struck the wing, but it broke up prior to impact, with all debris passing beneath the wing, some without impacting the wing. Recall that the transport analysis presented in Section 3 states the bipod TPS debris would be 1026 cubic inches and 1.4 pounds for a 820 ft/sec velocity or 1239 cubic inches and 1.7 pounds for a 775 ft/sec velocity. The RCC foam impact test conducted at Southwest Research Institute was performed at 775 ft/sec with a 1.67-pound foam article.

12.0 Summary

During the first stage of ascent, before SRB separation, the left wing of *Columbia* was struck by debris from the ET –Y bipod foam ramp. Analysis of the bipod foam ramp design, material, and processes suggests that the probable contributing mechanisms for foam liberation were cracks, delamination or debonding, divots, shear loads, or some combination of these. Analytical and test estimates of foam debris size, trajectory, and impact location indicate that the foam struck the left Wing Leading Edge (WLE) in the area between Reinforced Carbon-Carbon (RCC) panels 5 and 9. The impact energy tests conducted at Southwest Research Institute support the theory that the left wing RCC (lower panel 8 area, and/or an adjacent Tee seal) was damaged by the debris impact.

During ascent several new flight experience events occurred. These were all very near existing flight envelopes and well within the certified flight envelope for which the Shuttle was designed. The data indicate that all new flight experiences could be attributed to the winds aloft and SRB performance. The new flight experiences may have individually or collectively contributed to liberation of the bipod foam ramp, but data are inconclusive in this regard.

Launch radar analyses are inconclusive in determining size, shape, or identity of the debris measured after SRB separation. The radar data and analyses are inconclusive as to whether any of the debris impacted the orbiter.

There is data indicating that an object departed the orbiter on flight day 2 with a small relative separation velocity. Ballistics and Radar Cross Section (RCS) testing and analyses have excluded all tested objects except for a partial WLE Tee seal, a whole WLE Tee seal, or a partial WLE RCC panel. Data are inconclusive in determining the identity of the flight day 2 object, or whether the object was associated with the bipod foam debris impact.

Analysis of the RCC damage location and size is consistent with data from ascent. Analyses from orbiter telemetry, Modular Auxiliary Data System (MADS), aerodynamic and aero-thermal reconstruction and simulation, and debris forensics suggest that the RCC was damaged prior to Entry Interface (EI). The best estimate of the damage location is in the panel 8 lower area. Indications from modeling are that the damage size could have produced heating equivalent to a 6 to 10 inch hole diameter in the lower panel 8 area, or in one of the Tee seals adjacent to RCC panel 8.

The damage in the left wing RCC provided a pathway for hot gas to enter the left wing leading edge and support structure during entry. This resulted in significant damage to the left wing and the subsequent loss of vehicle control, leading to aerodynamic breakup.

Appendix A

Acronyms and Abbreviations

AA	Accelerometer Assembly
AC	Alternating Current
AFB	Air Force Base
AFRL	Air Force Research Labs
AFS	Air Force Station
AFSPC	Air Force Space Command
APU	Auxiliary Power Unit
BN	Ballistic Number
BSM	Booster Separation Motor
CAD	Computer-Aided Design
CAIB	Columbia Accident Investigation Board
CEI	Contract End Item
CF4	Tetraflouromethane
CFD	Computational Fluid Dynamics
CG	Center of Gravity
CSA	Canadian Space Agency
DAO	Data Assimilation Office
DAP	Digital Auto Pilot
dBsm	Decibels Relative to One Square Meter
DLR	German Aerospace Research Establishment
DOLILU	Day of Launch I-Load Update
DTA	Double Type A
EDO	Extended Duration Orbiter
EI	Entry Interface
EORF	Enhanced Orbiter Refrigerator/Freezer
ER	Eastern Range
ESA	European Space Agency
EST	Eastern Standard Time
ET	External Tank
FEP	Front End Processor
FOD	Foreign Object Debris
FRCS	Forward Reaction Control System
FREESTAR	Fast Reaction Enabling Science Technology and Research
FRSI	Felt Reusable Surface Insulation
GMT	Greenwich Mean Time
GNC	Guidance Navigation and Control
GRAM	Global Reference Atmosphere Model
GSE	Ground Support Equipment
Hi-Q	Maximum Dynamic Pressure
HMF	Hypergolic Maintenance Facility
HP	Hand Pack
HRSI	High-Temperature Reusable Surface Insulation
IEA	Integrated Electronics Assembly
IFA	In-Flight Anomaly
IMU	Inertial Measurement Unit
IPR	Interim Problem Report
IRN	Interface Revision Notice
ISS	International Space Station
JDMTA	Jonathan Dickinson Missile Tracking Annex
KSC	Kennedy Space Center
LAF	Lost and Found
LaRC	Langley Research Center
LCC	Launch Commit Criteria
LCD	Launch Countdown
LESS	Leading Edge Structural Subsystem
LH2	Liquid Hydrogen
LO2	Liquid Oxygen
LOS	Loss of Signal
LOX	Liquid Oxygen
LPS	Launch Processing System
LRU	Line Replaceable Unit
LWT	Light Weight Tank
MADS	Modular Auxiliary Data System
MAF	Michoud Assembly Facility
MCC	Mission Control Center
MEIDEX	Mediterranean Israeli Dust Experiment
MET	Mission Elapsed Time
MILA	Merritt Island Launch Area
MLP	Mobile Launch Platform
MMOD	Micrometeoroid or Orbital Debris
MOTR	Multiple-Object Tracking Radar
MPS	Main Propulsion System
MR	Management Review
MRB	Material Review Board
MSBLS	Microwave Scanning Beam Landing System
MSID	Measurement Stimulation Identification
NAIT	NASA Accident Investigation Team
NASA	National Aeronautics and Space Administration
NASDA	Japanese National Space Development
NDE	Non-Destructive Evaluation
NSI	NASA Standard Initiator
ODRC	Operational Data Retrieval Complex
OI	Operational Instrumentation
OMDP	Orbiter Maintenance Depot Processing
OMI	Operations and Maintenance Instruction
OMM	Orbiter Major Maintenance
OMS	Orbital Maneuvering System
PAFB	Patrick Air Force Base
PAL	Protuberance Air Load
PAPI	Precision Approach Position Indicator
PE	Performance Enhancement
PLB	Payload Bay
PMBT	Propellant Mean Bulk Temperature
PR	Problem Report
PRSD	Power Reactants Storage Device
QC	Quality Control
RCC	Reinforced Carbon-Carbon
RCS	Radar Cross Section
RDM	Research Double Module
RF	Radio Frequency
RGA	Rate Gyro Assembly
RSR	Range Separation Rate
RSRM	Re-usable Solid Rocket Motor
RSS	Range Safety System
RTV	Room Temperature Vulcanized
SAMS	Space Acceleration Measurement System
SIP	Strain Isolation Pad
SLA	Super Light Ablator
SLF	Shuttle Landing Facility
SLWT	Super Light Weight Tank
SMG	Space Meteorology Group
SOFI	Spray-On Foam Insulation
SRB	Solid Rocket Booster
SSME	Space Shuttle Main Engine
STA	Shuttle Training Aircraft
STS	Space Transportation System
TDRS	Tracking and Data Relay Satellite
TEOS	Tetraethyl Orthosilicate
TPS	Thermal Protection System
TVC	Thrust Vector Control
UHF	Ultra-High Frequency
VRCS	Vernier Reaction Control System
WLE	Wing Leading Edge

Appendix B

Working Scenario Team

Team Leaders

- **Columbia Accident Investigation Board**
  - CAIB Group I Lead: Major General John Barry
  - CAIB Group III Lead: Dr. James Hallock

- **NASA, Johnson Space Center**
  - NASA Lead, Flight Director Office: LeRoy E. Cain
  - NASA Deputy, Flight Director Office: J. Steve Stich

Primary Technical Support and POCs

- **Columbia Accident Investigation Board**
  - Lt. Col. Larry Butkis

- **Cimmaron**
  - Phil Glynn

- **Hernandez Engineering**
  - Ernest Ramirez

- **Johnson Space Center**
  - Flight Director Office: Phil Engelauf
  - Mission Operations Directorate: Jeffrey Kling, Michael Sarafin, Jon Reding, Dr. J.C. Melcher, Barbara Conte
  - Engineering Directorate: Gene Grush, Don Curry, Reynaldo Gomez, Steve Labbe, Jose Caram, Chris Madden, Julie Kramer, Steve Rickman
  - Space Shuttle Progam, Launch Integration Manager: N. Wayne Hale
  - Space Shuttle Systems Integration: Rod Wallace
  - International Space Station Vehicle Program: Tom Martin
  - Human Exploration Science: Greg Byrne

- **Kennedy Space Center**
  - Processing: Mike Leinbach, Charlie Abner, Terri Herst, Shawn Greenwell, Tim Wilson

- **Marshall Space Flight Center**
  - External Tank Working Group: Dr. Paul Munafo
  - External Tank Project: Neil Otte, Jerry Smelser
  - Reusable Solid Rocket Motor: Steve Cash
  - Solid Rocket Booster: Joe Lusk
  - Space Shuttle Main Engine: Mike Kynard

- **Michoud Assembly Facility**
  - Ron Wetmore
  - Eugene Sweet
  - Dan Callan

- **The Boeing Company**
  - Mark Hasselbeck
  - Mike Dunham

- **United Space Alliance**
  - Doug White
  - Pam Madera